

学位論文

Study on sign problem via
Lefschetz-thimble path integral
(レフシェッツスィンブル上の経路積分による)
符号問題の研究

平成27年12月博士（理学）申請
東京大学大学院理学系研究科
物理学専攻

谷崎 佑弥

Study on sign problem via Lefschetz-thimble path integral

Yuya Tanizaki

*Department of Physics, Graduate School of Science,
The University of Tokyo*

December 2015

PhD Thesis



Abstract

In this thesis, I study the sign problem appearing in the path-integral approach to strongly-coupled systems. This problem appears in many interesting systems, such as finite-density quantum chromodynamics (QCD), the repulsive Hubbard model away from the half filling, frustrated spin systems, and so on. In these systems, the Euclidean classical action S takes complex values, and the oscillatory nature of the Boltzmann weight e^{-S} causes the serious technical problems in *ab initio* numerical computations. In this study, I use the recently developing technique, called the path integral on Lefschetz thimbles, in order to understand the essence and difficulties of the sign problem in the path-integral formalism.

The basic idea of the Lefschetz-thimble method is to deform the integration contours in the complexified configuration space using Cauchy integration theorem. Under this deformation, the original oscillatory integral is decomposed into the sum of nicely convergent integrals, and the sign problem becomes moderate. Each integration cycle in this decomposition is called a Lefschetz thimble. In this thesis, I first give a concise review on this method, and demonstrate how it works by computing real-time Feynman kernels for free theories.

Next, I discuss the spontaneous breaking of chiral symmetry in 0-dimensional field theories without the sign problem. Chiral symmetry breaking is one of the characteristic features of low-energy QCD spectrum, and it is important to revisit this phenomenon using Lefschetz thimbles. I developed an efficient way to compute Lefschetz thimbles when a continuous symmetry is slightly broken due to the small explicit breaking term. This study also elucidates that the Lefschetz-thimble decomposition is suitable to analyze Lee–Yang zeros in the path-integral formulation, and the phase structure of the model is discussed for complex coupling constants.

If one tries to analyze finite-density QCD in the same way, the sign problem appears even at the level of the mean-field approximation. I show that the Lefschetz-thimble decomposition respects the anti-linearly extended charge conjugation so that the effective potential becomes manifestly real, and the saddle-point analysis based on this theorem solves the sign problem appearing in the mean-field approximation. The Polyakov-loop effective model of heavy-dense QCD is studied with this method as a lucid demonstration. Since all the quarks are heavy in this model, fermion dynamics is simplified and the mean-field treatment becomes accurate.

The sign problem in finite-density QCD with light flavors is known to become too severe as the quark chemical potential goes beyond the threshold of pion mass. In order to see what happens there, I consider the one-site Fermi Hubbard model, which is exactly solvable but has the severe sign problem in the path-integral expression. In this case, the above mean-field approximation is not applicable, and I elucidate its reason by studying topological structures of Lefschetz thimbles. I also show that interference of complex phases among multiple classical solutions play a pivotal role to understand the sign problem and the correct phase structures using path integrals. I discuss this interference is also important in the finite-density QCD with light flavors if the baryon chemical potential exceeds the pion mass.

In order to give a feedback of this finding to other approaches to the sign problem, I re-

late this newly developing technique, the Lefschetz-thimble path integral, with a conventional approach to the sign problem, the complex Langevin method. It is known that the complex Langevin method sometimes does not give correct answers, and I analytically show that the original complex Langevin method cannot give correct results if interference of complex phases among classical solutions becomes important. This gives a simple criterion for incorrectness of the complex Langevin method without doing its numerical simulation, and suggests that the complex Langevin method is not directly applicable to the finite-density QCD. To resolve this problem, I propose to modify the complex Langevin method with some technical working hypothesis, and it is numerically tested for the one-site Hubbard model. The original formulation of the complex Langevin method gives the wrong answer for this model. The modified complex Langevin method improves the result, but there exists systematic discrepancy, which requires further systematic studies on its properties.

Table of Contents

Title page	i
Abstract	iii
Table of Contents	v
Citations to published works	vii
Acknowledgments	ix
1 Introduction	1
1.1 Path integral quantization	1
1.2 QCD at finite chemical potential, and sign problem	2
1.3 Lefschetz-thimble approach to the path integral	6
1.4 Outline of this thesis	10
2 Path integral on Lefschetz thimbles	11
2.1 Picard–Lefschetz theory for oscillatory integrations	11
2.2 Path integral on Lefschetz thimbles	14
2.3 Simple examples in quantum mechanics	18
2.3.1 Free non-relativistic particles	18
2.3.2 Harmonic oscillator	21
2.4 Physical relevance of complex classical solutions	23
2.4.1 Complex classical solutions of the double-well potential	23
2.4.2 Quantum tunneling in the real-time path integral	26
2.5 Brief summary	28
3 Lefschetz-thimble approach to the spontaneous symmetry breaking	31
3.1 Spontaneous breaking of \mathbb{Z}_2 chiral symmetry	31
3.1.1 0-dimensional Gross–Neveu model	31
3.1.2 Structures of Lefschetz thimbles in massless case	32
3.1.3 Stokes phenomena and Lee–Yang zeros	35
3.1.4 Structures of Lefschetz thimbles in a massive case	38
3.2 Lefschetz thimbles with continuous symmetry	40
3.2.1 Exact continuous symmetry	40
3.2.2 Continuous symmetry with small explicit breaking	43
3.3 Spontaneous breaking of $U(1)_A$ chiral symmetry	48
3.3.1 0-dimensional Nambu–Jona-Lasinio model	48
3.3.2 Structures of Lefschetz thimbles in the massless case	49
3.3.3 Massive case	51
3.4 Brief summary	55

4	Lefschetz-thimble approach to the Silver Blaze problem	57
4.1	Sign problem in the mean-field approximation	57
4.1.1	Real-valuedness of the partition function and observables	57
4.1.2	Mean-field approximation and complex classical actions	59
4.2	One-site Hubbard model	62
4.2.1	Physical properties of the model	62
4.2.2	Path integral formulation and the sign problem	63
4.2.3	Lefschetz-thimble analysis at strong couplings	66
4.2.4	Importance of interference	71
4.3	Speculation on the Silver Blaze problem at finite-density QCD	75
4.4	Brief summary	77
5	Complex Langevin method revisited via Lefschetz-thimble integrals	79
5.1	Complex Langevin method and its failure	79
5.1.1	Brief review on basics of complex Langevin method	79
5.1.2	Semiclassical inconsistency	80
5.2	Modification of complex Langevin method	81
5.2.1	Proposal to modify complex Langevin method	82
5.2.2	Numerical test of the proposal	83
5.3	Brief summary	86
6	Summary and Outlook	89
A	Homology	91
A.1	General property	91
A.2	Smale–Witten theory	92
B	Path integral on Lefschetz thimbles and supersymmetry	95
B.1	Lefschetz thimble and SUSY quantum mechanics.	95
B.2	Hamilton dynamics	97
	References	99

Citations to published works

The materials given in Chapter 2 are based on the work below in collaboration with Takayuki Koike:

- **Yuya Tanizaki**, Takayuki Koike, “Real-time Feynman path integral with Picard–Lefschetz theory and its applications to quantum tunneling”, *Annals of Physics* 351 (2014) 250, [[arXiv:1406.2386\[math-ph\]](#)].

The results of Chapter 3 are based on the works below in collaboration with Takuya Kanazawa:

- **Yuya Tanizaki**, “Lefschetz-thimble techniques for path integral of zero-dimensional $O(n)$ sigma models”, *Phys. Rev. D* 91, 036002 (2015), [[arXiv:1412.1891\[hep-th\]](#)].
- Takuya Kanazawa, **Yuya Tanizaki**, “Structure of Lefschetz thimbles in simple fermionic systems”, *J. High Energy Phys.* 03 (2015) 044, [[arXiv:1412.2802\[hep-th\]](#)].

The first part of Chapter 4 is based on the work below in collaboration with Hiromichi Nishimura and Kouji Kashiwa:

- **Yuya Tanizaki**, Hiromichi Nishimura, Kouji Kashiwa, “Evading the sign problem in the mean-field approximation through Lefschetz-thimble path integral”, *Phys. Rev. D* 91, 101701(R) (2015), [[arXiv:1504.02979\[hep-th\]](#)].

The latter part of Chapter 4 and the results of Chapter 5 are based on the works below in collaboration with Yoshimasa Hidaka and Tomoya Hayata:

- **Yuya Tanizaki**, Yoshimasa Hidaka, Tomoya Hayata, “Lefschetz-thimble analysis of the sign problem in one-site fermion model”, to appear in New. J. Phys., [[arXiv:1509.07146\[hep-th\]](#)].
- Tomoya Hayata, Yoshimasa Hidaka, **Yuya Tanizaki**, “Complex saddle points and the sign problem in complex Langevin simulation”, under Review, [[arXiv:1511.02437\[hep-lat\]](#)].

The results of Appendix B are based on the work below in collaboration with Kenji Fukushima:

- Kenji Fukushima, **Yuya Tanizaki**, “Hamilton dynamics for the Lefschetz thimble integration akin to the complex Langevin method”, *Prog. Theor. Exp. Phys.* (2015) 111A01, [[arXiv:1507.07351\[hep-th\]](#)].

Acknowledgments

First of all, I would like to thank Tetsuo Hatsuda for supporting my Ph.D. course not only as a supervisor but also as an individual physicist since when I was a master course student. Furthermore, it was a luncheon conversation with him which brought my attention to this exciting research topic.

Let me acknowledge all the collaborators in this research. My Ph.D. thesis is composed of a lot of collaborating works. Without interesting communications with them, I could not produce so much works on broad areas with rich contents.

Takayuki Koike, one of my mathematician friends, helps me a lot in order to understand mathematical foundations of this research. His deep knowledge on the multi-variable complex analysis contributes a lot for our collaborating work.

I also thank Takuya Kanazawa, who brought my attention to the symmetry breaking phenomena in Lefschetz-thimble methods. His clear discussion deepens my understanding on the chiral symmetry breaking.

Kouji Kashiwa introduced me the sign problem appearing in the mean-field and perturbative calculations. One day, Hiromichi Nishimura gave a seminar on the importance of the charge conjugation in this problem at RIKEN, and we started discussion on its rigorous reformulation. This became my first study on the sign problem.

With Kenji Fukushima, I discussed technical aspects of Lefschetz thimbles using supersymmetry. Through this research, I learned a lot from him about the basics of complex Langevin method.

I thank Yoshimasa Hidaka and Tomoya Hayata for intriguing me to the one-site Hubbard model. Before starting computations, I did not expect the toy model contains so much fascinating information on the sign problem.

During my Ph.D. course, I could have a chance to visit Brookhaven National Laboratory for several times. In these visits, I could discuss the sign problem with Robert D. Pisarski, and it was a good chance for me to understand the sign problem and the Polyakov-loop effective models of quantum chromodynamics.

I also stayed in University of Illinois at Chicago for about a half year. I enjoyed that stay and appreciate hospitality of the member of high-energy theory and nuclear group, Mikhail Stephanov, Ho-Ung Yee, Wai-Yee Keung, David Mesterhazy, and Ahmed Ismail. During this stay, I had a chance to visit North Carolina State University, and private communications with Aleksey Cherman, and Mithat Ünsal were especially important to me for establishing my ideas on this research topic.

The author is financially supported by Grants-in-Aid for the fellowship of Japan Society for the Promotion of Science (JSPS) (No.25-6615). The set of these works was partially supported by the RIKEN interdisciplinary Theoretical Science (iTHES) project, by the Program for Leading Graduate Schools of Ministry of Education, Culture, Sports, Science, and Technology (MEXT), Japan, and by JSPS Strategic Young Researcher Overseas Visits Program for

Accelerating Brain Circulation.

Chapter 1

Introduction

Path integral is a useful tool to study strongly-correlated systems, however it sometimes suffer from the sign problem in its numerical computations. In this thesis, I study the sign problem by applying the Picard–Lefschetz theory to unveil its essence and difficulties. First, I would like to give a general introduction to study nonperturbative aspects of quantum statistical physics using path integrals in Sec. 1.1. In Sec. 1.2, we explain the sign problem appearing in the finite-density Quantum ChromoDynamics (QCD), and its relevance to neutron stars is mentioned. The basic idea of the Picard–Lefschetz theory is introduced in order to analyze the sign problem in Sec. 1.3 via the simple example of the Airy integral. We show the outline of this thesis in Sec. 1.4.

1.1 Path integral quantization

Path integral is invented as one of the ways to quantize the classical system [1, 2]. The biggest difference of quantum mechanics from classical mechanics is the existence of interference of transition amplitudes. In order to deal with it, the Feynman path integral tells us that the time development of quantum states can be interpreted as a summation of classical amplitudes $\exp(iS[x]/\hbar)$ over all possible spacetime classical paths $x(t)$. That is, we can compute the time development kernel $K(x_i, t_i; x_f, t_f)$ of a quantum particle in the potential $V(x)$ by performing the infinite-dimensional formal integration,

$$K(x_i, t_i; x_f, t_f) = \int \mathcal{D}x \exp \left[\frac{i}{\hbar} \int_{t_i}^{t_f} dt \left(\frac{1}{2} \left(\frac{dx}{dt} \right)^2 - V(x) \right) \right], \quad (1.1.1)$$

with the boundary condition $x(t_i) = x_i$ and $x(t_f) = x_f$. This reformulation of the Schrödinger equation is conceptually interesting, and it becomes easy to observe connection between classical and quantum mechanics.

By replacing the time t with the imaginary time $-i\tau$, one can study the thermal equilibrium property instead of the quantum dynamical processes [3]. This relates the d -dimensional quantum systems with $(d+1)$ -dimensional classical statistical systems, and we can study statistical physics using computational techniques of quantum physics and vice versa. In the path-integral representation, the partition function $Z(T)$ is given by

$$Z(T) = \int \mathcal{D}x \exp \left[-\frac{1}{\hbar} \int_0^\beta dt \left(\frac{1}{2} \left(\frac{dx}{d\tau} \right)^2 + V(x) \right) \right], \quad (1.1.2)$$

with the periodic boundary condition $x(0) = x(\beta)$, and $\beta = 1/T$ is the inverse temperature.

From the viewpoint of numerical computation, however, there is an outstanding difference between the real-time formalism (1.1.1) and the imaginary-time one (1.1.2). The integrand of (1.1.2) is positive definite, which means that we can regard it as a probability density. Instead of solving the quantum system exactly, we can create the ensemble of spacetime paths $x(\tau)$ according to the Boltzmann weight and solve the system in a stochastic way. This is called the Monte Carlo simulation of the path integral, and its computational cost scales algebraically with the system size in this method even when the system consists of many particles. Many thermodynamic quantities can be computed for various systems using the path-integral Monte Carlo method, such as finite-temperature quantum chromodynamics (QCD) in hadron physics [4], and liquid helium [5], ultracold atomic gases [6], Bose–Fermi mixtures [7] in condensed matter physics.

1.2 QCD at finite chemical potential, and sign problem

Quantum ChromoDynamics QCD is a part of the Standard Model in particle physics, and is a non-Abelian gauge theory with the color gauge group $SU(3)$. The gauge bosons are called gluons that belong to the adjoint color representation, while the spin- $\frac{1}{2}$ particles called quarks are in the fundamental color representation. QCD describes strong interaction among quarks and gluons, which are confined inside of hadrons. Therefore, this theory plays a pivotal role to understand properties of nuclei, compact stars, and also early Universe.

The QCD Lagrangian has quite a simple form,

$$\mathcal{L}_{\text{QCD}} = \mathcal{L}_{\text{YM}}(A) + \bar{q} [(\not{D}_A + m) - \mu_q \gamma_4] q, \quad (1.2.1)$$

$$\mathcal{L}_{\text{YM}} = \frac{1}{4g^2} \text{Tr}(F_{\mu\nu})^2, \quad (1.2.2)$$

where $F_{\mu\nu} = \partial_\mu A_\nu - \partial_\nu A_\mu + i[A_\mu, A_\nu]$ is the field strength of the $SU(3)$ gauge field, q is the quark Dirac field, and $\not{D} = \gamma_\nu(\partial_\nu + iA_\nu)$ is the Dirac operator (See, e.g., Refs. [8–11] as a textbook). Here, μ_q is the quark chemical potential. In order to study the equation of state of QCD, one has to compute the partition function

$$\begin{aligned} Z_{\text{QCD}}(T, \mu_q) &= \int \mathcal{D}A \mathcal{D}\bar{q} \mathcal{D}q \exp \left(- \int d^4x \mathcal{L}_{\text{QCD}} \right) \\ &= \int \mathcal{D}A \text{Det} [(\not{D}_A + m) - \mu_q \gamma_4] \exp \left(- \int d^4x \mathcal{L}_{\text{YM}} \right). \end{aligned} \quad (1.2.3)$$

In the second line, quark and antiquarks are integrated out, and we have to take the statistical average in terms of the gauge field A to find the thermodynamic properties.

Let us first describe the properties of QCD in the vacuum and its spectrum. One of the remarkable property of QCD as a four-dimensional gauge theory is its asymptotic freedom [12–14]: The gauge coupling constant g depends on the renormalization scale Q , and the one-loop renormalization group shows that

$$\alpha_s(Q) = \frac{g(Q)^2}{4\pi} = \frac{1}{4\pi\beta_0 \ln(Q^2/\Lambda_{\text{QCD}}^2)}, \quad (1.2.4)$$

with $\beta_0 = (11N_c - 2N_f)/48\pi^2$. In QCD, the number of color is $N_c = 3$, and the number of fermion flavor is $N_f = 6$, and thus $\beta_0 > 0$. Λ_{QCD} is the typical energy scale of strong interactions, and its appearance in quantization is called the dimensional transmutation. The world average value is $\Lambda_{\text{QCD}} = 213(8) \text{ MeV}$ when α_s is measured at the Z boson mass using the modified minimal subtraction ($\overline{\text{MS}}$) renormalization scheme based on the next-to-next-to-leading-order QCD predictions [15, 16]. This means that the QCD coupling constant becomes logarithmically weaker as the energy scale $Q^2 \rightarrow \infty$, and this property is called asymptotic freedom. Thanks to the asymptotic freedom of QCD, we can study the deep inelastic scattering experiments [17, 18] based on the first-principle computations, and the parton picture inside nucleons can be justified in high-energy nuclear collisions.

At low energies $Q \lesssim \Lambda_{\text{QCD}}$, physics of strong interaction is much more difficult. Free quarks and gluons have never been observed even though QCD Lagrangian contains them. Because of the nature of strong interaction, they cannot live longer than the timescale $\sim 1/\Lambda_{\text{QCD}}$. All the quarks and gluons are confined inside hadrons, and this is called the quark confinement [19]. Thanks to the lattice formulation of gauge theories [19] and its Monte Carlo numerical simulation [20–22], we have a solid theoretical foundation to study the nonperturbative aspects of low-energy QCD. Analytical study of nonperturbative gauge theories is still a big dream in theoretical and mathematical physics. Confinement of color degrees of freedom has a close relation with topological aspects of gauge theories [23–28]. Indeed, development of supersymmetric gauge theories elucidates that confining phases have rich topological structures [29, 30]. In order to extend this knowledge for non-supersymmetric cases, we must look more carefully at the microscopic dynamics of gauge fields, and there is much effort in that direction [31–44].

Let us briefly mention the phenomenological aspects of low-energy QCD spectrum. In the quark model, conventional hadrons are classified into mesons and baryons:

$$\text{hadron} \quad \begin{cases} \text{meson } (q\bar{q}') & \cdots \quad \pi, K, \eta, \text{ etc.} \\ \text{baryon } (qqq) & \cdots \quad N, \Sigma, \Xi, \text{ etc.} \end{cases} \quad (1.2.5)$$

Mesons are bound states of a quark q and an anti-quark \bar{q}' , and thus they have no baryon charge $Q_B = 0$. The lightest meson is the pion (π), whose mass m_π is about 140 MeV. Baryons are bound states of three quarks q , and thus they are fermions with the baryon number $Q_B = 1$. The lightest baryon is nucleon N , e.g. proton p or neutron n , whose mass m_N is about 940 MeV.

It is important to notice that there is a huge difference between $m_\pi/2$ and $m_N/3$. In the QCD Lagrangian, the light flavor of quarks, u , d , and s , have approximate chiral symmetry under $q \mapsto e^{i\theta\gamma_5}q$ because their masses are smaller than the strong scale Λ_{QCD} . At 2 GeV, the current quark masses of u , d , and s in the $\overline{\text{MS}}$ scheme are $m_u \simeq 2.15(15) \text{ MeV}$, $m_d \simeq 4.70(20) \text{ MeV}$, and $m_s \simeq 93.5(2.5) \text{ MeV}$, respectively [16]. This chiral symmetry $SU(n_f) \times SU(n_f)$ is spontaneously broken to $SU(n_f)$ in the QCD vacuum ($n_f = 2$ or 3),

$$\langle \bar{q}q \rangle = (-230 \text{ MeV})^3, \quad (1.2.6)$$

and pseudo-scalar mesons, such as pions, can be regarded as Nambu–Goldstone bosons [45, 46]. Because of the small explicit breaking of the chiral symmetry, those Nambu–Goldstone bosons become massive. The pion mass, $m_\pi \propto \sqrt{\Lambda_{\text{QCD}} m_{u,d}}$, is parametrically much smaller than Λ_{QCD} , which sets the natural mass scale of other hadrons.

QCD matters The possibility of existence of quark matters inside neutron stars has been discussed since the discovery of the asymptotic freedom [47]. Since the coupling constant becomes smaller at high energies or densities, quarks and gluons are expected to be liberated from

confinement. Based on such an idea, a prototype of the QCD phase diagram was proposed in Ref. [48]. The transition temperature there was given by the limiting temperature of the statistical model of hadrons, which comes from the exponential growth of hadron resonances [49]. For a modern version of the QCD phase diagram, see Ref. [50].

Finite-temperature QCD at $\mu_q = 0$ can be studied using Monte Carlo simulations of lattice QCD [4]. Around the physical quark masses with $(2+1)$ -flavor, lattice QCD suggests that there is no phase transition between hadron and quark-gluon plasma phases [51–53]. Thermodynamic functions show rapid crossover around the pseudo-critical temperature $T_{pc} \simeq 160$ MeV, and it is a big surprise to have a continuity of two seemingly-disparate systems. Only at sufficiently high temperatures $T \gg T_{pc}$, does the system become weakly coupled plasma. Near the pseudo-critical temperature, the system is most likely strongly coupled, and the non-perturbative treatment is inevitable. This system is also studied experimentally by colliding ultra-relativistic nuclei, and its phenomenology and model study are developing [54].

However, the situation becomes totally different for the finite-density QCD. We have no lattice QCD simulation of finite-density nuclear matters, and this is because of the big obstacle called the sign problem. Before its explanation, let us mention physical importance of finite-density QCD. One way to realize a high-density QCD matter is to mash up nuclei by external forces, like gravity, and the neutron star is a strongly promising candidate of a laboratory for its study. We must have rather stiff neutron star cores in order to explain recently observed two-solar-mass neutron stars [55]. The origin of large magnetic fields of magnetars is also still veiled. Forthcoming observation of gravitational waves from neutron star mergers is expected to provide many clues about high-density nuclear matters. Thus, its *ab initio* calculation becomes more and more important to understand dense nuclear matters.

Sign problem and Silver Blaze phenomenon At finite μ_q , the quark determinant becomes oscillatory complex functions of the gauge field A . In order to see this fact, let us study the properties of the Dirac spectrum. Let us set $D(A, \mu_q) = \not{D}_A - \gamma_4 \mu_q + m$, and consider

$$[\not{D}_A - \gamma_4 \mu_q] \psi_{n;A,\mu_q} = i\lambda_n(A, \mu_q) \psi_{n;A,\mu_q}. \quad (1.2.7)$$

Here, $i\lambda_n(A, \mu_q)$ is the n -th eigenvalue and $\psi_{n;A,\mu_q}$ is its eigenfunction. Let us multiply γ_5 from the left on the both sides of (1.2.7), then we obtain that

$$[\not{D}_A - \gamma_4 \mu_q] \gamma_5 \psi_{n;A,\mu_q} = -i\lambda_n(A, \mu_q) \gamma_5 \psi_{n;A,\mu_q}. \quad (1.2.8)$$

Therefore, $\det(D(A, \mu_q)) = \prod_n (\lambda_n(A, \mu_q)^2 + m^2)$. The quark determinant is positive definite if $\mu_q = 0$ because $\gamma_\nu D_\nu(A)$ is anti-Hermitian and $\lambda_n(A, 0) \in \mathbb{R}$. On the other hand, this does not hold for $\mu_q \neq 0$, and $\lambda_n(A, \mu_q)$ is complex in general. This means that the integrand of the QCD partition function does not accept the probabilistic interpretation, and importance sampling breaks down [56]. This is called the sign problem, and the same problem appears in many other condensed matter systems [57], such as non-Fermi liquids, the repulsive Hubbard model away from half filling, frustrated spin systems, etc.

One way to perform the Monte Carlo simulation is to consider the phase-quenched QCD, defined by

$$Z_{|\text{QCD}|}(T, \mu_q) = \int \mathcal{D}A |\text{Det}(D(A, \mu_q))| \exp \left(- \int d^4x \mathcal{L}_{YM} \right). \quad (1.2.9)$$

Since there is no oscillatory nature, we can generate the ensemble of the gauge field for this path integral and perform the Monte Carlo simulation. If the phase-quenched QCD is sufficiently

“similar” to the finite-density QCD, we can use this ensemble of the gauge fields to study finite-density nuclear matters and we have no problems in a practical sense.

This is not the case, however. In order to explain this lucidly, we consider the two-flavor QCD at $T = 0$. In this case, the phase-quenched QCD is the same with QCD with isospin chemical potential because $|\text{Det } D(A, \mu_q)|$ is realized by assigning the positive chemical potential $+\mu_q$ to the up quark and the negative one $-\mu_q$ to the down quark. Since \not{D}_A is anti-Hermitian, we find that

$$\begin{aligned} \overline{\det(D(A, \mu_q))} &= \det[-\not{D}_A - \gamma_4 \mu_q + m] \\ &= \prod_n (\lambda_n(A, -\mu_q)^2 + m^2) \\ &= \det(D(A, -\mu_q)). \end{aligned} \tag{1.2.10}$$

Therefore, $|\det(D(A, \mu_q))|^2 = \det(D(A, \mu_q))\det(D(A, -\mu_q))$ as we mentioned. At $T = 0$, the thermodynamic partition function picks up the minimum of the free energy. The lightest hadron is pion ($m_\pi \simeq 140$ MeV), and it belongs to the three dimensional representation of the isospin. Therefore, $Z_{|\text{QCD}|}(0, \mu_q)$ has a singularity at $\mu_q = m_\pi/2$, and the pion condensation appears, $\langle \pi^+ \rangle \neq 0$, in the phase-quenched QCD for $\mu_q > m_\pi/2$.

For QCD at finite baryon densities, nothing must happen at $\mu_q = m_\pi/2$ because pion has no baryon charges. In the hadron spectrum, the lightest baryon is a nucleon ($m_N \simeq 940$ MeV). Therefore, $Z_{\text{QCD}}(0, \mu_q)$ has the first-order phase transition at $\mu_q = (m_N - B)/3$, which is known as the nuclear liquid-gas phase transition. Here, B is the nuclear binding energy $\simeq 16$ MeV. For $\mu_q < (m_N - B)/3$, the QCD partition function must pick up the QCD vacuum state at $T = 0$, but this is highly nontrivial from the consideration on the phase-quenched QCD.

In order to perform the *ab initio* computation of the finite-density QCD, we have to understand why QCD at low temperatures experiences nothing for $\mu_q < (m_N - B)/3$. Only after comprehension of this “trivial physics” from the viewpoint of path integral, can we study the properties of finite-density nuclear matters by using lattice QCD. We must give much effort on nothing by saying it the “curious incident”, and, in Ref. [58], this fact is called with the funny, fashionable name “Silver Blaze problem” after the famous story [59] of Sherlock Holmes. There, “*the curious incident of the dog in the night-time*” is an essential clue for Sherlock Holmes to unveil the mystery. It was quite natural that the dog did nothing at ordinary times, however Holmes said “*I had grasped the significance of the silence of the dog, for one true inference invariably suggests others...*”.

In our case, the phenomenological evidence clearly tells us that the partition function has no singularities at low temperatures for $\mu_q \leq (m_N - B)/3$, but this becomes a curious incident from the viewpoint of the quark picture. The hadron spectrum contains the quasi-massless pions. Since the Dirac spectrum knows it, its real part starts from $m_\pi/2$. Naively thinking, quarks can be excited without any cost for $\mu_q > m_\pi/2$, and the thermodynamic state must experience the phase transition from the QCD vacuum. We must have much imagination and guess the reason why the quark chemical potential does nothing for $m_\pi/2 \lesssim \mu_q \lesssim (m_N - B)/3$. Interestingly, we can argue that all the phase transitions are hidden by the Silver Blaze problem: The orbifold equivalence in the large- N_c limit suggests that all the critical points in the QCD phase diagram must lie inside the pion condensation phase of the phase quenched QCD [60, 61].

1.3 Lefschetz-thimble approach to the path integral

Now I can concretely state the purpose of this thesis. We would like to understand how the partition function becomes constant on the chemical potential at $T = 0$ in the path-integral formulation. After unveiling its origin and analytical structure, I would like to propose a new way to solve the sign problem which can explain the Silver Blaze phenomenon.

For this purpose, I apply the Picard–Lefschetz theory to the path integral. The Picard–Lefschetz theory is a basic technique in the complex analysis with many variables. This theory is very useful in analyzing the asymptotic behavior of multiple oscillatory integrals [62, 63], because it gives a suitable extension of the steepest descent method for the one-dimensional integration. In the context of physics, its usefulness was found out in the study of analytic properties of the Chern–Simons and Liouville theory [64–66].

In the case of one-dimensional integrals, $\int d\phi \exp(-S(\phi)/\hbar)$, the steepest descent path can be determined by solving the stationary phase condition, $\text{Im}[S(\phi)] = \text{constant}$, in the complex plane $\phi \in \mathbb{C}$. The stationary phase condition is also important even for multiple oscillatory integrals, and it looks quite suitable for solving the sign problem. In Refs. [67–70], the Monte Carlo integration on a steepest descent cycle was proposed and numerically tested for scalar field theories.

Example: Airy integral Its formulation will be reviewed in the following chapter, and let us quickly remind the steepest descent method in the case of Airy integral. This is the simplest model to understand the philosophy of the Lefschetz-thimble method. When $x \in \mathbb{R}$, the Airy function is given by

$$\text{Ai}(x) = \int_{\mathbb{R}} \frac{d\phi}{2\pi} \exp(-S(\phi, x)), \quad (1.3.1)$$

$$S(\phi, x) = -i \left(\frac{\phi^3}{3} + x\phi \right). \quad (1.3.2)$$

If one tries to evaluate this integration literally, this is a hard numerical task because of its oscillatory nature. Such a hard task is not necessary thanks to Cauchy’s integration theorem. We can continuously change the integration contour in the complex plane \mathbb{C} without changing the result of integrals.

We show the usefulness of changing the integration contour in Fig. 1.1 for the Airy integral with $x = 1$. If we perform the integration on the real axis, we must perform the oscillatory integral, which integrand is shown with red dashed line in Fig. 1.1 (b). In order to apply the steepest descent method, we complexify the integration variable, $\phi \in \mathbb{C}$ and find the complex saddle points:

$$\partial_{\phi} S(\phi, 1) = -i(\phi^2 + 1) = 0, \implies \phi = \pm i. \quad (1.3.3)$$

Let us change the integration contour to the steepest descent path \mathcal{J} as shown in Fig. 1.1 (a), which passes the saddle point $\phi = +i$. In the case of one-variable integrals, the path of steepest descent can be found by solving

$$\text{Im}[S(\phi, 1)] = \text{Im}[S(i, 1)]. \quad (1.3.4)$$

The integrand shows the nice convergence after the deformation of the integration contour, and it is shown with the blue solid line in Fig. 1.1 (b). Furthermore, the condition (1.3.4) tells us

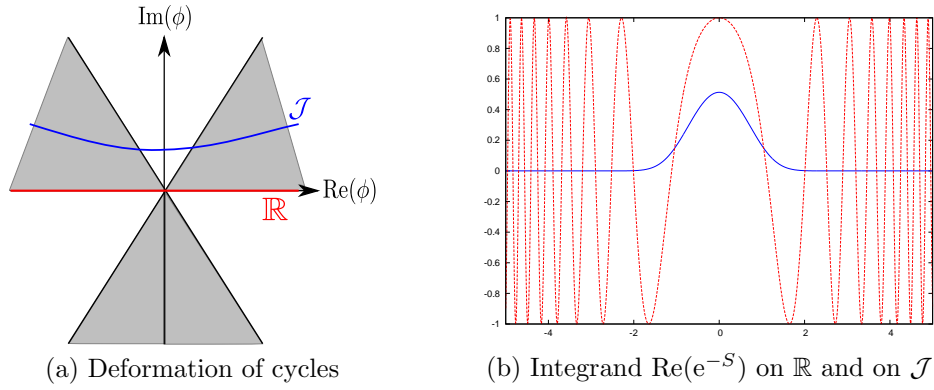


Figure 1.1: Effectiveness of the change of integration contours in the Airy integral ($x = 1$). (a) Gray region represents the nicely convergent direction $\text{Re}(S) \rightarrow \infty$, and the blue curve is the steepest descent path \mathcal{J} that connects two distinct convergent directions. (b) Dashed red and solid blue curves represents behaviors of the integrand $\text{Re}(e^{-S})$ on \mathbb{R} and \mathcal{J} , respectively.

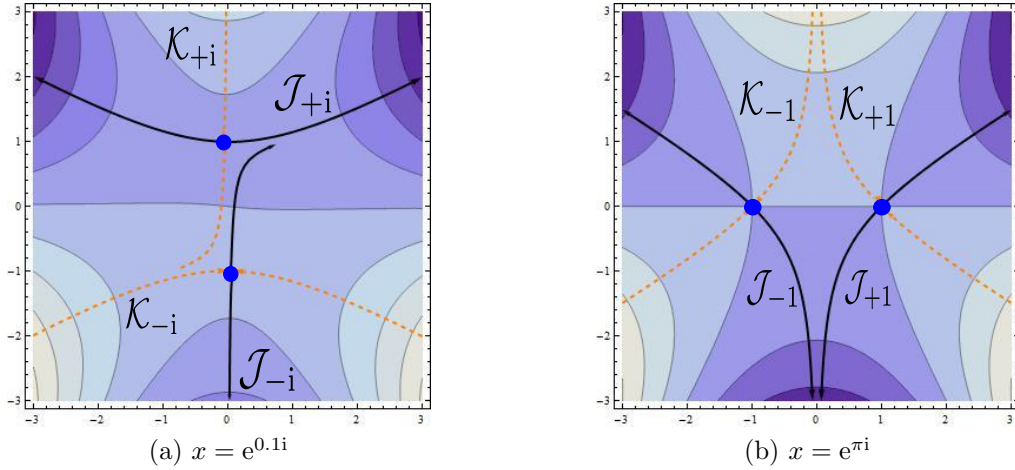


Figure 1.2: Steepest descent and ascent paths, $\mathcal{J}_{\pm i\sqrt{x}}$ (solid black lines) and $\mathcal{K}_{\pm i\sqrt{x}}$ (dashed orange lines), in the complex ϕ -plane. Blue blobs show complex saddle points, $\phi = e^{\pm i\pi/2}\sqrt{x}$.

that the oscillatory complex phase does not appear from the exponential part in the integrand of (1.3.1). As we already mentioned, this property is useful to study the sign problem, and Monte Carlo integrals on steepest descent paths were proposed in Refs. [67–73].

Let us consider a generic case when x takes complex values and perform analytic continuation of $\text{Ai}(x)$. Once the integration contour in (1.3.1) is deformed to the steepest descent path \mathcal{J} for $x > 0$, the integral expression is convergent for generic x . Let us rewrite that path \mathcal{J} in Fig. 1.1 using the steepest descent paths at x . We show steepest descent paths at $x = e^{0.1i}$ and $x = e^{\pi i}$ in Fig. 1.2. If the phase of x is sufficiently small, or, more precisely speaking, if $|\arg(x)| < 2\pi/3$, only the steepest descent path $\mathcal{J}_{+i\sqrt{x}}$ contributes as we can see in Fig. 1.2 (a). That is, for $|\arg(x)| < 2\pi/3$,

$$\text{Ai}(x) = \int_{\mathcal{J}_{+i\sqrt{x}}} \frac{d\phi}{2\pi} e^{-S(\phi, x)}. \quad (1.3.5)$$

However, when the phase of x is close to π , the topological structure of steepest descent paths

changes drastically, as is shown in Fig. Fig. 1.2 (b). For $|\arg(x) - \pi| < \pi/3$,

$$\text{Ai}(x) = \int_{\mathcal{J}_{+i\sqrt{x}}} \frac{d\phi}{2\pi} e^{-S(\phi,x)} + \int_{\mathcal{J}_{-i\sqrt{x}}} \frac{d\phi}{2\pi} e^{-S(\phi,x)}. \quad (1.3.6)$$

The jump between these two expression occurs at $\arg(x) = 2\pi/3$, which is called the Stokes jump. At $\arg(x) = 2\pi/3$, the complex phases of the classical actions at two saddle points become identical,

$$\text{Im} [S(+i\sqrt{x}, x)] = \text{Im} [S(-i\sqrt{x}, x)], \quad (1.3.7)$$

since $S(\pm i\sqrt{x}, x) = \pm \frac{2}{3}x^{3/2}$. Therefore, the stationary phase condition $\text{Im}(S(\phi)) = \text{constant}$ connects two saddle points $\phi = \pm i\sqrt{x}$. This is called the Stokes ray, at which the topological structure of $\mathcal{J}_{\pm i\sqrt{x}}$ changes. In order to apply the steepest descent method, tracing this change of the topological structure of \mathcal{J}_σ is essential for $\sigma \in \{\pm i\sqrt{x}\}$. Using the steepest ascent paths \mathcal{K}_σ shown with orange dashed lines in Fig. 1.2, this topological information can be encoded as intersection numbers. The integral on \mathcal{J}_σ must be taken into account if the intersection number $\langle \mathcal{K}_\sigma, \mathbb{R} \rangle$ between \mathcal{K}_σ and the original contour \mathbb{R} is nonzero, and

$$\text{Ai}(x) = \sum_{\sigma \in \{\pm i\sqrt{x}\}} \langle \mathcal{K}_\sigma, \mathbb{R} \rangle \int_{\mathcal{J}_\sigma} \frac{d\phi}{2\pi} e^{-S(\phi,x)}. \quad (1.3.8)$$

This single equation summarizes (1.3.5) and (1.3.6). Its extension to multiple oscillatory integrals will be considered in Sec. 2.1, and the steepest descent contours \mathcal{J}_σ are called Lefschetz thimbles.

Based on the steepest descent method with (1.3.5) and (1.3.6), let us study the asymptotic behavior of $\text{Ai}(x)$ with $|x| \rightarrow \infty$. According to (1.3.5), for $|\arg(x)| < 2\pi/3$,

$$\text{Ai}(x) \sim \frac{\exp\left(-\frac{2}{3}x^{3/2}\right)}{2\sqrt{\pi}x^{1/4}}. \quad (1.3.9)$$

Since the second term in (1.3.6) is exponentially smaller than the first term, this expression turns out to be valid not only for $|\arg(x)| < 2\pi/3$ but also for $|\arg(x)| < \pi$. On the other hand, for $|\arg(x) - \pi| < \pi/3$, we obtain

$$\text{Ai}(x) \sim \frac{\cos\left(\frac{2}{3}(-x)^{3/2} - \frac{\pi}{4}\right)}{\sqrt{\pi}(-x)^{1/4}}. \quad (1.3.10)$$

This expression is also valid for $|\arg(x) - \pi| < 2\pi/3$. Remarkably, there are two different asymptotic expressions of $\text{Ai}(x)$ for $\pi/3 < \arg(x) < \pi$, although $\text{Ai}(x)$ is a single-valued function on \mathbb{C} . This is one realization of the Stokes phenomenon. The boundary of applicability of each asymptotic approximation is called the anti-Stokes ray, at which the dominance of different Lefschetz thimbles is interchanged.

Stokes jumps, Borel summation For completeness of our analysis, let us briefly review the above analysis from the viewpoint of the differential equation. Let us recall that the Airy function is a solution of the Airy equation:

$$\left(\frac{d^2}{dx^2} - x\right) Z(x) = 0. \quad (1.3.11)$$

One can easily see that (1.3.1) satisfies the Airy equation (1.3.11) by using the integration by parts. By regarding $\text{Ai}(x)$ as a partition function $Z(x)$, the Airy equation is nothing but the Dyson–Schwinger equation,

$$0 = \int_{\mathbb{R}} \frac{d\phi}{2\pi} \frac{d}{d\phi} \exp i \left(\frac{\phi^3}{3} + x\phi \right) = i \int_{\mathbb{R}} \frac{d\phi}{2\pi} (\phi^2 + x) \exp i \left(\frac{\phi^3}{3} + x\phi \right). \quad (1.3.12)$$

Since ϕ^2 in the last expression can be replaced by $-d^2/dx^2$, we can obtain (1.3.11). This is a second-order ordinary differential equation and has two linearly independent solutions, commonly called $\text{Ai}(x)$ and $\text{Bi}(x)$. This corresponds to the fact that this model has two complex saddle points and thus two steepest descent contours. One can also easily see that using a new variable $\zeta = \frac{2}{3}x^{3/2}$ the Airy equation has a regular singularity at $\zeta = 0$ and an irregular singularity of rank 1 at $\zeta = \infty$. Because of these singularities, the perturbative expansion of these partition functions $\text{Ai}(x)$ and $\text{Bi}(x)$ at infinities can only have asymptotic expansions, i.e., the formal power series in terms of $1/\zeta$ are divergent. This fact leads an exotic but interesting fact, which is called the Stokes phenomenon.

Let us observe an example of the Stokes phenomenon. In the limit $x \rightarrow \infty$ with $\arg(x) < \pi$, the Airy function has a formal series expansion

$$\text{Ai}(x) \sim \frac{\exp(-\frac{2}{3}x^{3/2})}{2\sqrt{\pi}x^{1/4}} \sum_{k=0}^{\infty} (-1)^k \frac{\Gamma(k + \frac{5}{6}) \Gamma(k + \frac{1}{6})}{\Gamma(\frac{5}{6}) \Gamma(\frac{1}{6}) 2^k k!} \frac{1}{(\frac{2}{3}x^{3/2})^k}. \quad (1.3.13)$$

This series is asymptotic because the coefficients show factorial growth. In order to make sense out of this divergent series, we perform the Borel transformation;

$$B(\eta) = \sum_{k=0}^{\infty} (-1)^k \frac{\Gamma(k + \frac{5}{6}) \Gamma(k + \frac{1}{6})}{\Gamma(\frac{5}{6}) \Gamma(\frac{1}{6}) 2^k (k!)^2} \eta^k. \quad (1.3.14)$$

Here, the series coefficient is divided by $k!$ compared with that of the corresponding divergent series, and we can easily check that this series has the convergent radius $|\eta| < 2$. By regarding $B(\eta)$ as an analytic function by using the analytic continuation, it has a branch point at $\eta = -2$. In this easy case, one can perform this summation explicitly to find that

$$B(\eta) = {}_2F_1 \left(\frac{1}{6}, \frac{5}{6}; 1; -\frac{\eta}{2} \right). \quad (1.3.15)$$

In order to relate $B(\eta)$ with the Airy function, we perform the Laplace transformation and get

$$\text{Ai}(x) = \frac{\zeta^{5/6} e^{-\zeta}}{2^{5/6} 3^{1/6} \pi^{1/2}} \int_0^{\infty} d\eta e^{-\zeta \eta} B(\eta), \quad (1.3.16)$$

with $\zeta = \frac{2}{3}x^{3/2}$ and $\arg(\zeta) < \pi/2$. This is a well-known expression of $\text{Ai}(x)$ using the confluent hypergeometric function. In this way, we can reconstruct the original analytic function using its asymptotic series expression, and this process is called the Borel summation.

Using the Borel summation (1.3.16), let us observe how Stokes jump plays into the game. Let us add a phase $\zeta \mapsto \zeta e^{i\theta}$, then we also rotate the phase of the integration contour of η so that $\eta \in e^{-i\theta}[0, \infty)$. Therefore, for $-\pi < \theta < \pi$,

$$\text{Ai}(x e^{i2\theta/3}) = \frac{(\zeta e^{i\theta})^{5/6} e^{-\zeta e^{i\theta}}}{2^{5/6} 3^{1/6} \pi^{1/2}} \int_0^{e^{-i\theta}\infty} d\eta e^{-\zeta e^{i\theta} \eta} B(\eta). \quad (1.3.17)$$

As $\theta \rightarrow \pi$, the integration contour comes close to the negative real axis, while $B(\zeta)$ has a branch cut $(-\infty, -2]$. For $\theta > \pi$, the additional contribution comes from the contour integration around the branch cut, and this phase clearly corresponds to $\arg(x) = \frac{2\pi}{3}$. Therefore, the appearance of this additional contribution is the Stokes jumping, and $\theta = \pi$ is the Stokes ray. More interestingly, asymptotic expansions at two complex saddle points have some relations; for example, large order perturbations at a saddle point determines the small order behaviors of perturbations at another saddle point. This is an example of resurgence, proposed by Écalle [74]. For a readable review of resurgence, see Ref. [75] for example.

1.4 Outline of this thesis

In Chapter 2, we briefly review the Picard–Lefschetz theory and study its basic properties in the context of oscillatory integrations. Picard–Lefschetz theory is established only for finite-dimensional oscillatory integrals, and thus we confirm that the Picard–Lefschetz theory works well also for free quantum mechanical systems.

In order to understand how this technique describes the symmetry breaking phenomena, we discuss, in Chapter 3, the \mathbb{Z}_2 and $O(4)$ chiral symmetry breaking in simple models without the sign problem. By relating the Lefschetz-thimble analysis with the Lee–Yang zeros of partition functions, we can find how the phase transition is described in the Lefschetz-thimble path integral for these models.

In order to understand the origin and structures of the sign problem, we consider two examples with the sign problem in Chapter 4. The first one is the Polyakov-loop effective model of the finite-density quantum chromodynamics (QCD) with heavy quarks. In order to study it, we developed the mean-field approximation which is applicable even if the sign problem exists, and we can judge whether this works nicely by computing topologies of Lefschetz thimbles. This gives the mathematical foundation to study the Polyakov-loop models at finite quark densities. The second one is the one-site Fermi Hubbard model, which can be exactly solved and has the severe sign problem in the path-integral expression. In this case, the above mean-field approximation is not applicable, and we elucidate its reason by studying topological structures of Lefschetz thimbles. We show that interference of complex phases among complex classical solutions play a pivotal role to understand the sign problem and the correct phase structures using path integrals. We discuss this interference is also important in the finite-density QCD with light flavors if μ_q exceeds the half of the pion mass.

We relate the Lefschetz-thimble path integral with the complex Langevin method, in Chapter 5. Since the complex Langevin method has longer history for the study of the sign problem, this establishment enables us to translate the new findings in the Lefschetz-thimble approach to other methods, and vice versa. We show that the original complex Langevin method cannot give correct results if interference of complex phases among classical solutions is important. This gives the simplest criterion for incorrectness of the complex Langevin method without doing its numerical simulation. This also means that the complex Langevin method is not directly applicable to the baryon Silver Blaze phenomenon in finite-density QCD. To resolve this problem, we propose to modify the complex Langevin method by introducing a technical working assumption, and it is numerically tested with the one-site Hubbard model. The original complex Langevin method does not give the correct answer, while the modified one shows rapid transitions of number densities. Although the result is not yet perfect, this study shows the importance of relating the Lefschetz-thimble method to other approaches to the sign problem.

Chapter 2

Path integral on Lefschetz thimbles

In this chapter, we describe the application of the Picard–Lefschetz theory to the oscillatory multi-dimensional integrals, and its formal application to the functional integration. We study its generic properties, and compute it for solvable examples in quantum mechanics.

2.1 Picard–Lefschetz theory for oscillatory integrations

In this section, we first explain how to apply the Picard–Lefschetz theory to oscillatory integrals [62, 64, 65]. This gives a mathematically rigorous extension of the steepest descent analysis given in Sec. 1.3. In this formulation, the complex analogue of the Morse homology theory turns out to be useful, which basics is briefly summarized in Appendix A. The procedure for its formal application to the path integral is summarized in Sec. 2.2.

We consider the following integral,

$$Z_{\hbar} = \int_{\mathcal{Y}} d\theta \exp(-S(\theta)/\hbar), \quad (2.1.1)$$

where \hbar is a real parameter. Here, the integration region \mathcal{Y} is taken as a real affine variety with a natural volume form $d\theta$. One can think of $\mathcal{Y} = \mathbb{R}^n$ and $d\theta = d^n x$ as the simplest example, but one can also think of classical real Lie groups such as $\mathcal{Y} = O(n), U(n)$, etc. with the Haar measure. Let $S : \mathcal{Y} \rightarrow \mathbb{C}$ be a complex-valued polynomial on \mathcal{Y} , and $\text{Re}(S) \rightarrow \infty$ as $|\theta| \rightarrow \infty$ if \mathcal{Y} is non-compact. In the language of physics, \mathcal{Y} is the configuration space, $d\theta$ is the path-integral measure, and S is the (Euclidean) classical action of the system to be quantized. Since $S(\theta)$ is complex in general, this is an oscillatory integral, which often impedes the study of analytic properties of the partition function Z_{\hbar} . Picard–Lefschetz theory provides a beautiful framework, which converts such oscillatory integration into a sum of nicely convergent integrals. This \hbar in quantum physics appears with different symbols in different contexts; e.g., it can be replaced by $k_B T$ in statistical mechanics, $1/N$ in $N \times N$ matrix models, etc.

We assume the existence of complexification \mathcal{X} of \mathcal{Y} . This means that there is a complex manifold \mathcal{X} which contains \mathcal{Y} as its subspace, and that \mathcal{Y} is fixed under the complex conjugation $\bar{\cdot}$ of \mathcal{X} ; i.e. $\mathcal{Y} \hookrightarrow \mathcal{X}$ and $y = \bar{y}$ for any $y \in \mathcal{Y}$. For $\mathcal{Y} = \mathbb{R}^n, O(n), U(n)$, their complexifications are $\mathcal{X} = \mathbb{C}^n, O(n, \mathbb{C}), GL(n, \mathbb{C})$, respectively. By assumption, \mathcal{X} has a Kähler metric

$$ds^2 = \frac{1}{2} g_{i\bar{j}} \left(dz^i \otimes d\bar{z}^j + d\bar{z}^j \otimes dz^i \right), \quad (2.1.2)$$

and we denote its Kähler form as $\omega = \frac{i}{2} g_{i\bar{j}} dz^i \wedge d\bar{z}^j$. Here, (z^1, \dots, z^n) is a local holomorphic coordinate on \mathcal{X} .

One of the primary purposes of this section is to construct all the possible n -dimensional integration cycles \mathcal{J} in \mathcal{X} , on which $\text{Im}(S/\hbar)$ is constant so that the integrand is not oscillatory. After that, we represent (2.1.1) using those integrations. Let us denote $\mathcal{I} = -S/\hbar$ and regard it as a holomorphic function on \mathcal{X} (\hbar can now be complex in general). The Morse function h is defined by its real part:

$$h = \text{Re } \mathcal{I} = \frac{\mathcal{I} + \bar{\mathcal{I}}}{2}. \quad (2.1.3)$$

Since the integrand is given by $e^{h-i\text{Im}(S/\hbar)}$, this function h represents the importance of field configurations in the complexified space.

Let $p \in \mathcal{X}$ be a critical point of h ; i.e., $\partial_i h|_p = \bar{\partial}_i h|_p = 0$ using a local holomorphic coordinate (z^1, \dots, z^n) around p . Equivalently, $p \in \mathcal{X}$ is a critical point if and only if

$$\partial_i \mathcal{I}|_p = 0, \quad (2.1.4)$$

because $\bar{\partial}_i \mathcal{I} = 0$ follows automatically from the Cauchy–Riemann condition. This is nothing but the classical equation of motion. It is important to study the property of the Hessian matrix around the critical point. Using a complex version of the Morse lemma, we obtain that there exists a local coordinate around a non-degenerate critical point p such that

$$\mathcal{I}(z) = \mathcal{I}(0) + (z^1)^2 + \dots + (z^n)^2. \quad (2.1.5)$$

By taking its real part, we find that the Morse function behaves around the non-degenerate critical point as

$$h(z) = h(0) + (x^1)^2 + \dots + (x^n)^2 - (y^1)^2 - \dots - (y^n)^2, \quad (2.1.6)$$

with $z^j = x^j + iy^j$. Therefore, the Morse index of non-degenerate critical points of h is always $n = \dim_{\mathbb{C}} \mathcal{X}$.

In order to find the integration cycles \mathcal{J} , it turns out to be important to compute a relative homology of \mathcal{X} using the Morse function h . In order to explain it, we introduce the Morse's gradient flow equation by

$$\frac{dz^i}{dt} = -2g^{i\bar{j}} \frac{\partial h}{\partial z^{\bar{j}}} = -g^{i\bar{j}} \frac{\partial \bar{\mathcal{I}}}{\partial z^{\bar{j}}}, \quad \frac{d\bar{z}^{\bar{j}}}{dt} = -2g^{i\bar{j}} \frac{\partial h}{\partial z^i} = -g^{i\bar{j}} \frac{\partial \mathcal{I}}{\partial z^i}. \quad (2.1.7)$$

Along this flow equation, the Morse function h decreases monotonically:

$$\frac{dh}{dt} = -2g^{i\bar{j}} \partial_i h \bar{\partial}_{\bar{j}} h (= -|\nabla h|^2) \leq 0. \quad (2.1.8)$$

It is clear that the equality holds only at a critical point of h on \mathcal{X} . It is of great importance for our purpose to notice that $\text{Im}(S/\hbar)$ is constant on each flow line given by the gradient flow. Let us denote $H := \text{Im } \mathcal{I} = (\mathcal{I} - \bar{\mathcal{I}})/2i$, and then

$$\frac{dH}{dt} = \frac{dz^i}{dt} \partial_i H + \frac{d\bar{z}^{\bar{j}}}{dt} \bar{\partial}_{\bar{j}} H = -\frac{g^{i\bar{j}}}{2i} (\partial_i \mathcal{I} \bar{\partial}_{\bar{j}} \mathcal{I} + \partial_i \mathcal{I} (-\bar{\partial}_{\bar{j}} \mathcal{I})) = 0. \quad (2.1.9)$$

This phenomenon has a clear interpretation based on the classical mechanics [64], and it becomes useful when we extend this formalism to the case with continuous symmetries. Such an extension will be discussed in Sec. 3.2, and for a moment we continue to assume that all the

critical points are non-degenerate. In order to explain the classical-mechanical interpretation, we pay attention to the symplectic structure ω of \mathcal{X} , which defines the Poisson bracket $\{\cdot, \cdot\}_P$ by

$$\{f, g\}_P = -2ig^{k\bar{l}} (\partial_k f \bar{\partial}_{\bar{l}} g - \bar{\partial}_{\bar{l}} f \partial_k g). \quad (2.1.10)$$

In the language of classical mechanics, this says that x^i and y^i describe coordinates and canonical momenta, respectively. Now, the conservation of H becomes crystal-clear because the gradient flow equation is nothing but the Hamilton equation of motion:

$$\frac{dz^i}{dt} = \{H, z^i\}_P, \quad \frac{d\bar{z}^j}{dt} = \{H, \bar{z}^j\}_P. \quad (2.1.11)$$

The conservation of H is very important to define \mathcal{J} , because we would like to find integration cycles satisfying that property.

Let us denote the set of critical points by Σ . It labels critical points p_σ , i.e.,

$$\partial \mathcal{I}|_{p_\sigma} = 0, \quad (2.1.12)$$

for any $\sigma \in \Sigma$. In order for \mathcal{J} to be an integration cycle of the integration measure $e^{h-i\text{Im}(S)} d^n z$, it must be an n -dimensional object in \mathcal{X} and $h \rightarrow +\infty$ as $|z| \rightarrow \infty$ on \mathcal{J} . Therefore, we can identify all the possible integration cycles as an element of the relative homology $H_n(\mathcal{X}, \mathcal{X}_{-T}; \mathbb{Z})$ for $T \gg 1$, where

$$\mathcal{X}_{-T} := \{x \in X \mid h(x) \leq -T\}. \quad (2.1.13)$$

In other words, we identify all the points in \mathcal{X} if e^h is sufficiently close to zero, and compute the n -th homology of $\mathcal{X}/\mathcal{X}_{-T}$. The homology can be computed in the following way (see Appendix A for its detail). Assume that any two critical points are not connected via the gradient flow, then the Morse function h diverges to $-\infty$ as the flow time goes to ∞ . The Lefschetz thimble \mathcal{J}_σ associated to the critical point p_σ is defined as the moduli space for endpoints of solutions $c: \mathbb{R} \rightarrow \mathcal{X}$ of the downward flow

$$\frac{dc}{dt} = \{\text{Im } \mathcal{I}, c\}_P, \quad (2.1.14)$$

with the initial condition $c(-\infty) = p_\sigma$. That is,

$$\mathcal{J}_\sigma = \left\{ c(0) \in \mathcal{X} \mid \lim_{t \rightarrow -\infty} c(t) = p_\sigma \right\}. \quad (2.1.15)$$

Since all the critical points of h has the Morse index n , the Lefschetz thimbles \mathcal{J}_σ generates the n -th homology $H_n(\mathcal{X}, \mathcal{X}_{-T}; \mathbb{Z})$. By construction, the integrand becomes non-oscillatory and exponentially convergent on \mathcal{J}_σ .

Let us rewrite the original oscillatory integral (2.1.1) by using integrals on \mathcal{J}_σ . For that purpose, we regard the real cycle \mathcal{Y} as an element of $H_n(\mathcal{X}, \mathcal{X}_{-T}; \mathbb{Z})$ and express it in terms of Lefschetz thimbles as

$$\mathcal{Y} = \sum_{\sigma \in \Sigma} n_\sigma \mathcal{J}_\sigma, \quad (2.1.16)$$

where $n_\sigma \in \mathbb{Z}$. With this expression, the oscillatory integral becomes

$$Z_h = \sum_{\sigma \in \Sigma} n_\sigma \int_{\mathcal{J}_\sigma} d\theta \exp(-S/\hbar). \quad (2.1.17)$$

Since $\text{Im}(S/\hbar)$ is constant on each Lefschetz thimble \mathcal{J}_σ , each integration on the right hand side is expected not to suffer from the sign problem.

The coefficients n_σ is still unknown, and thus we must give the formula for them. Those coefficients can be obtained by introducing the intersection pairing. Consider the relative homology $H_n(\mathcal{X}, \mathcal{X}^T; \mathbb{Z})$, where

$$\mathcal{X}^T = \{x \in \mathcal{X} \mid h(x) \geq T\}. \quad (2.1.18)$$

As we have shown for $H_n(\mathcal{X}, \mathcal{X}_{-T}; \mathbb{Z})$ for $T \gg 1$, the n -th homology $H_n(\mathcal{X}, \mathcal{X}^T; \mathbb{Z})$ is generated by

$$\mathcal{K}_\sigma = \left\{ c(0) \in \mathcal{X} \mid \lim_{t \rightarrow +\infty} c(t) = p_\sigma \right\}. \quad (2.1.19)$$

By definition, $h(z) \leq h(p_\sigma)$ for $z \in \mathcal{J}_\sigma$ and $h(z) \geq h(p_\sigma)$ for $z \in \mathcal{K}_\sigma$, and the equality holds only at $z = p_\sigma$. Therefore, \mathcal{J}_σ and \mathcal{K}_σ intersects only at p_σ . Since we have assumed that any two distinct critical points are not connected via the gradient flow, \mathcal{J}_σ and \mathcal{K}_τ does not intersect with each other if $\sigma \neq \tau$. We find that the intersection pairing is naturally given as

$$\langle \mathcal{J}_\sigma, \mathcal{K}_\tau \rangle = \delta_{\sigma\tau} \quad (2.1.20)$$

under some appropriate orientations. Therefore, the coefficients n_σ can be calculated as

$$n_\sigma = \langle \mathcal{Y}, \mathcal{K}_\sigma \rangle. \quad (2.1.21)$$

That is, n_σ is given by the intersection number between the original integration cycle \mathcal{Y} and \mathcal{K}_σ , which gives an extension of the formula (1.3.8) for the example of the Airy integral. We now find that that the integration cycle can be decomposed into the sum of Lefschetz thimbles without any ambiguities.

2.2 Path integral on Lefschetz thimbles

We apply the Picard–Lefschetz theory to path integrals, which method is called the Lefschetz-thimble path integral. In this section, we first summarize the way to compute the Lefschetz-thimble path integral by formally using the argument in Sec. 2.1. This decomposes an infinite-dimensional oscillatory integral into the sum of well-defined, i.e. convergent, path integrals on Lefschetz thimbles. On each Lefschetz thimble, we show that the Schwinger–Dyson equation holds. This section is adapted from Ref. [76].

Application of the Picard–Lefschetz theory to path integrals Let us consider the path-integral quantization of a classical action $S[x(t)] = \int dt L(x, dx/dt)$ (For a Minkowski path integral, $-S$ should be regarded as iS in the usual convention). In the path-integral quantization, the transition amplitude $K(x_f, t_f; x_i, t_i)$ is computed by summing up the probability amplitude $\exp(-S[x]/\hbar)$ over the set of all the possible space-time paths $\mathcal{Y} = \{x : [t_i, t_f] \rightarrow \mathbb{R} \mid x(t_i) = x_i, x(t_f) = x_f\}$,

$$K(x_f, t_f; x_i, t_i) = \int_{\mathcal{Y}} \mathcal{D}x \exp\left(-\frac{S[x]}{\hbar}\right). \quad (2.2.1)$$

In general, the action $S[x]$ takes complex values for generic spacetime paths $x : [t_i, t_f] \rightarrow \mathbb{R}$, and (2.2.1) must be regarded as a limit of multiple oscillatory integrals.

The formal application of the Picard–Lefschetz theory to (2.2.1) can be summarized as follows [64–66]:

1. First, we must find all the solutions of the “complex” classical equation of motion, $\delta S[z] = 0$, in $\mathcal{X} = \{z : [t_i, t_f] \rightarrow \mathbb{C} \mid z(t_i) = x_i, z(t_f) = x_f\}$. We denote those solutions by z_σ ($\sigma \in \Sigma$ is the label).
2. For each z_σ , we compute the Lefschetz thimble \mathcal{J}_σ by solving the gradient flow equation

$$\frac{\partial z(t; u)}{\partial u} = \overline{\left(\frac{\delta S[z(t; u)]}{\delta z(t; u)} \right)}, \quad (2.2.2)$$

with the boundary conditions $z(t; -\infty) = z_\sigma(t)$, and $z(t_i, u) = x_i$ and $z(t_f, u) = x_f$. As we have shown in Sec. 2.1, $\text{Re } S \rightarrow +\infty$ and $\text{Im } S$ is a constant along flows. Therefore, the path integral on each Lefschetz thimble,

$$\mathcal{J}_\sigma := \left\{ z(\cdot; 0) : [t_i, t_f] \rightarrow \mathbb{C} \mid \lim_{u \rightarrow -\infty} z(t, u) = z_\sigma(t) \right\}, \quad (2.2.3)$$

shows good convergence.

3. The path integral (2.2.1) can be decomposed into the sum of the path integral on Lefschetz thimbles \mathcal{J}_σ ;

$$K(x_f, t_f; x_i, t_i) = \sum_{\sigma \in \Sigma} \langle \mathcal{K}_\sigma, \mathbb{R} \rangle \int_{\mathcal{J}_\sigma} \mathcal{D}z \exp \left(-\frac{S[z]}{\hbar} \right). \quad (2.2.4)$$

Here, $\langle \mathcal{K}_\sigma, \mathbb{R} \rangle$ is the intersection number of \mathcal{Y} and the dual thimbles,

$$\mathcal{K}_\sigma := \left\{ z(\cdot; 0) : [t_i, t_f] \rightarrow \mathbb{C} \mid z(t, +\infty) \rightarrow z_\sigma(t) \right\}. \quad (2.2.5)$$

Since we have only shown that this method is valid for finite-dimensional integrals in Sec. 2.1, the above procedure is somewhat formal and must be performed with appropriate regularization. We assume that some regularization is chosen, and that Lefschetz thimbles are well-defined as an integration cycle. If two distinct saddle points are connected via (2.2.2), the system is on the Stokes ray and the second assumption breaks down. However, this breakdown does not happen for generic cases because $\text{Im } S$ is a conserved quantity. In the following of this section, we use these assumptions implicitly.

Quantum equation of motions on Lefschetz thimbles Let us consider the consequence of the quantum equation of motion from the viewpoint of Lefschetz thimbles. The quantum equation of motions, or the Dyson–Schwinger equation, is given by

$$\int \mathcal{D}x \frac{\delta S[x]}{\delta x(t)} e^{-S[x]} = 0 \quad (2.2.6)$$

for any boundary conditions at $t = t_i$ and t_f . We first show that this equality (2.2.6) holds on each Lefschetz thimble, that is, for any $\sigma \in \Sigma$

$$\int_{\mathcal{J}_\sigma} \mathcal{D}z \frac{\delta S[z]}{\delta z(t)} e^{-S[z]} = 0. \quad (2.2.7)$$

Let us show a finite-dimensional analogue of (2.2.7) since the path integral is assumed to be regularized. $S(z)$ a holomorphic function of $z = (z^1, \dots, z^n)$, which has critical points z_σ . Then, we have to prove that

$$\int_{\mathcal{J}_\sigma} d^n z \frac{\partial S(z)}{\partial z^i} e^{-S(z)} = 0. \quad (2.2.8)$$

The following notations are useful to prove (2.2.8): let $\varepsilon = (\varepsilon^1, \dots, \varepsilon^n) \in \mathbb{C}^n$, then

$$S_\varepsilon(z) := S(z + \varepsilon), \quad Z_{\sigma, \varepsilon} := \int_{\mathcal{J}_\sigma} d^n z e^{-S_\varepsilon(z)}. \quad (2.2.9)$$

Since we can find that

$$\left. \frac{\partial Z_{\sigma, \varepsilon}}{\partial \varepsilon^i} \right|_{\varepsilon=0} = \int_{\mathcal{J}_\sigma} d^n z \frac{\partial S(z)}{\partial z^i} e^{-S(z)}, \quad (2.2.10)$$

it suffices to prove that $Z_{\sigma, \varepsilon}$ is independent of ε for sufficiently small ε .

All the saddle points $z_{\sigma, \varepsilon}$ of S_ε are clearly given by

$$z_{\sigma, \varepsilon} = z_\sigma - \varepsilon. \quad (2.2.11)$$

We can also readily find that the Lefschetz thimble $\mathcal{J}_{\sigma, \varepsilon}$ of S_ε is given by

$$\mathcal{J}_{\sigma, \varepsilon} = \mathcal{J}_\sigma - \varepsilon := \{z - \varepsilon | z \in \mathcal{J}_\sigma\} \quad (2.2.12)$$

as a subset of \mathbb{C}^n . When $\varepsilon = 0$, $\mathcal{J}_{\sigma, \varepsilon}$ does not intersect \mathcal{K}_τ if $\sigma \neq \tau$ and it intersects \mathcal{K}_σ transversally only at one point. This is an open condition, and thus valid for an open region of ε including $\varepsilon = 0$. For $|\varepsilon| \ll 1$,

$$\langle \mathcal{J}_{\sigma, \varepsilon}, \mathcal{K}_\tau \rangle = \delta_{\sigma\tau}, \quad (2.2.13)$$

which implies that $\mathcal{J}_{\sigma, \varepsilon} = \mathcal{J}_\sigma$ as integration cycles. This completes the proof of $Z_{\sigma, \varepsilon} = Z_{\sigma, 0}$, and we obtain (2.2.8).

Let us reverse the story. Assume that we have a generating functional $Z[j]$ satisfying the Dyson–Schwinger equation, or the quantum equation of motion,

$$(-S'[\partial/\partial j] + \hbar j)Z[j] = 0. \quad (2.2.14)$$

Using Lefschetz thimbles \mathcal{J}_σ , we can construct the general solution of this functional differential equation as

$$Z[j] = \sum_{\sigma} d_{\sigma} \int_{\mathcal{J}_{\sigma}} \mathcal{D}z e^{-S[z]/\hbar + j \cdot z}. \quad (2.2.15)$$

with some $d_{\sigma} \in \mathbb{C}$. These coefficients d_{σ} can be anything if one just requires the Dyson–Schwinger equation. In order to relate those generic solutions with the path-integral quantization, we must choose $d_{\sigma} = \langle \mathcal{K}_{\sigma}, \mathcal{Y} \rangle$.

Flow equations around complex classical solutions It would be useful to consider the structure of the perturbative fluctuations around a complex classical solution z_{σ} . Let us consider a classical and real-time action $\mathcal{I} = i \int dt \left[\frac{1}{2} \dot{z}^2 - V(z) \right]$ as an example; then the gradient flow (2.2.2) is given by

$$\frac{\partial z(t; u)}{\partial u} = -i \left(\frac{\partial^2 \bar{z}(t; u)}{\partial t^2} + V'(\bar{z}(t; u)) \right). \quad (2.2.16)$$

In order to restrict our consideration to the perturbative computations, we consider its linearization, $z = z_\sigma + \Delta z$, around the classical solution z_σ . It gives a parabolic partial differential equation,

$$\frac{\partial}{\partial u} \Delta z(t; u) = -i \left(\frac{\partial^2}{\partial t^2} + V''(\overline{z_\sigma}(t)) \right) \overline{\Delta z}(t; u). \quad (2.2.17)$$

In order to find analytic properties of this linearized equation, we try to construct its solutions by separating variables. Using an Ansatz $\Delta z(t; u) = e^{i\pi/4} \exp(\lambda u) f(t)$ ($\lambda > 0$), (2.2.17) reduces to an eigenvalue equation

$$- \left(\frac{\partial^2}{\partial t^2} + V''(\overline{z_\sigma}(t)) \right) \overline{f}(t) = \lambda f(t). \quad (2.2.18)$$

By separating the real and imaginary parts, $f(t) = f_1(t) + i f_2(t)$, (2.2.18) reads

$$\begin{pmatrix} -[\partial_t^2 + \text{Re } V''(\overline{z_\sigma}(t))] & -\text{Im } V''(\overline{z_\sigma}(t)) \\ -\text{Im } V''(\overline{z_\sigma}(t)) & [\partial_t^2 + \text{Re } V''(\overline{z_\sigma}(t))] \end{pmatrix} \begin{pmatrix} f_1 \\ f_2 \end{pmatrix} = \lambda \begin{pmatrix} f_1 \\ f_2 \end{pmatrix}. \quad (2.2.19)$$

On the space of smooth functions with the Dirichlet boundary condition, this differential operator L on the left hand side of (2.2.19) is self-adjoint. Its eigenvalues λ_j are real and eigenfunctions associated with different eigenvalues are orthogonal to each other. By assumption, $\lambda_j \neq 0$ for any j due to the non-degeneracy of critical points. Using this information, we can show that eigenvalues of L must be paired with opposite sign, $\pm \lambda_j$. To see this, the self-adjoint operator L is represented as $L = -[\partial_t^2 + \text{Re } V''(\overline{z_\sigma}(t))] \sigma_3 - \text{Im } V''(\overline{z_\sigma}(t)) \sigma_1$ using Pauli matrices σ_i . Introducing the “chirality” matrix $\varepsilon = i\sigma_2$, we can easily show that

$$\varepsilon^\dagger L \varepsilon = -L, \quad (2.2.20)$$

where $\varepsilon \varepsilon^\dagger = 1$.

It may be useful to remark here that the above property on the complexified fluctuation operator holds in general, although we are considering the Minkowski path integral as an example. It follows from the fact that the fluctuation operator is given by taking the continuum limit of the complex symmetric matrix.

The orthonormal property of L is not enough in order to perform the perturbative calculations around a complex saddle point. Let λ_a and λ_b be eigenvalues of L , and their eigenfunctions are denoted by $(f_{a,1}, f_{a,2})$ and $(f_{b,1}, f_{b,2})$, respectively. Assuming that $|\lambda_a| \neq |\lambda_b|$, we must show

$$\int dt \overline{f}_a f_b = 0, \quad (2.2.21)$$

where $f_a = f_{a,1} + i f_{a,2}$ and $f_b = f_{b,1} + i f_{b,2}$ for our purpose. Since the eigenfunctions are paired by multiplying ε^\dagger , $(f_{b,2}, -f_{b,1}) = \varepsilon^\dagger(f_{b,1}, f_{b,2})$ is an eigenfunction with the eigenvalue $-\lambda_b$. Orthogonality of L shows that

$$\int dt (f_{a,1} f_{b,1} + f_{a,2} f_{b,2}) = \int dt (f_{a,1} f_{b,2} - f_{a,2} f_{b,1}) = 0. \quad (2.2.22)$$

This is nothing but (2.2.21). The tangent space of \mathcal{J}_σ at z_σ is spanned by eigenfunctions with positive eigenvalues. In contrast, those with negative eigenvalues span the tangent space of \mathcal{K}_σ .

Now, we construct the tangent space $T_{z_\sigma} \mathcal{J}_\sigma$ of \mathcal{J}_σ at z_σ explicitly. Let $\{\lambda_n\}_{n=1}^\infty$ denote the positive eigenvalues of L , and $\{f_n\}_n$ the corresponding normalized eigenfunctions. Then, the tangent space $T_{z_\sigma} \mathcal{J}_\sigma$ is given by

$$T_{z_\sigma} \mathcal{J}_\sigma = \left\{ \sum_{n=1}^{\infty} a_n e^{i\pi/4} f_n(t) \mid a_n \in \mathbb{R} \right\}. \quad (2.2.23)$$

The behavior of $\mathcal{I}[z]$ on \mathcal{J}_σ up to $\mathcal{O}(\Delta z^2)$ is given by ($\Delta z(t) = \sum_n a_n e^{i\pi/4} f_n(t)$)

$$\begin{aligned} \mathcal{I}[z_\sigma + \Delta z] &= \mathcal{I}[z_\sigma] + \sum_{n,m} \frac{a_n a_m}{2} \int dt f_n(t) \left(\frac{\partial^2}{\partial t^2} + V''(z_\sigma(t)) \right) f_m(t) \\ &= \mathcal{I}[z_\sigma] - \sum_{n=1}^{\infty} \frac{\lambda_n}{2} a_n^2. \end{aligned} \quad (2.2.24)$$

This means that the real-time path integral on the Lefschetz thimble \mathcal{J}_σ is realized as a Wiener integration at least for small quantum fluctuations around z_σ .

Let me give one notice before closing this section. In quantum and many body physics, several low-lying eigenvalues λ_n may be sufficiently close to zero, e.g. $\lambda_n \sim \mathcal{O}(\hbar^{\alpha_n})$ with $\alpha_n > 0$. For these quasi-zero modes, the Gaussian approximation is not necessarily enough and we have to take into account the higher order corrections for those modes.

2.3 Simple examples in quantum mechanics

In this section, we compute real-time Feynman kernels using Lefschetz-thimble path integral for its demonstration. Three simple examples of quantum mechanics will be considered; free particles on a line and on a circle, and a harmonic oscillator. Since the our argument in previous sections is general and abstract, it would be useful to see the concrete way to compute Lefschetz thimbles of simple examples. It is also interesting to see that the real-time path integral for those systems turns out to be constructed as Lebesgue integrals on Lefschetz thimbles. This section is adapted from Ref. [76].

2.3.1 Free non-relativistic particles

Free particle on a line First, we consider path integral for a free particle on the real line \mathbb{R} . Let us solve the fundamental solution $K_{\text{free}}(x_f, t_f : x_i, t_i)$ of the Schrödinger equation,

$$i\hbar \frac{\partial}{\partial t} \psi(x, t) = -\frac{\hbar^2}{2} \frac{\partial^2}{\partial x^2} \psi(x, t), \quad (2.3.1)$$

by using the Lefschetz-thimble path integral.

The classical action of this system in (2.2.1) is given by,

$$\mathcal{I}[z] = i \int dt \frac{1}{2} \left(\frac{dz}{dt} \right)^2. \quad (2.3.2)$$

This can formally be regarded as a holomorphic functional on $\mathcal{X} = \{z : [t_i, t_f] \rightarrow \mathbb{C} \mid z(t_i) = x_i, z(t_f) = x_f\}$. The classical solution z_{cl} of this system is given by solving the Euler-Lagrange equation:

$$\frac{d^2 z_{\text{cl}}(t)}{dt^2} = 0. \quad (2.3.3)$$

Under the Dirichlet boundary condition $z(t_i) = x_i$ and $z(t_f) = x_f$, it is solved as

$$z_{\text{cl}}(t) = (x_f - x_i) \frac{t - t_i}{t_f - t_i} + x_i, \quad (2.3.4)$$

and the classical action is $\mathcal{I}[z_{\text{cl}}] = i(x_f - x_i)^2/2(t_f - t_i)$. This is a real-valued function, and then it belongs to the original integration cycle \mathcal{Y} of (2.2.1).

Let us compute Lefschetz thimbles, and, for that purpose, we have to write down the gradient flow. The Kähler metric of \mathcal{X} can be chosen as

$$ds^2 = \int dt \frac{1}{2} (\delta z(t) \otimes \delta \bar{z}(t) + \delta \bar{z}(t) \otimes \delta z(t)), \quad (2.3.5)$$

and then the cotangent space is spanned by $\delta z(t)$ and $\delta \bar{z}(t)$. The Kähler form of this metric is $\omega = \int dt \frac{1}{2} \delta z(t) \wedge \delta \bar{z}(t)$. Let us recall the definition of the Lefschetz thimble \mathcal{J} around $z_{\text{cl}}(t)$: It is defined as a set of gradient flows emanating from $z_{\text{cl}}(t)$:

$$\mathcal{J} = \left\{ z(t; 0) \in \mathcal{X} \left| z(t; -\infty) = z_{\text{cl}}(t), \frac{\partial z(t; u)}{\partial u} = -\overline{\left(\frac{\delta \mathcal{I}[z(t; u)]}{\delta z(t; u)} \right)} \right. \right\}. \quad (2.3.6)$$

This is a middle-dimensional cycle in \mathcal{X} and can be used as a domain of integration. Let us rewrite the path-integral expression of the Feynman kernel of the free particle K_{free} as

$$K_{\text{free}}(x_f, t_f; x_i, t_i) = \int_{\mathcal{J}} \mathcal{D}z \exp \frac{\mathcal{I}[z]}{\hbar}. \quad (2.3.7)$$

In the following, we will explicitly find that z_{cl} has the intersection number 1. In the real-time path integrals, it can generally be shown that the real-valued saddle point always has the unit intersection number [64, 65].

The Lefschetz thimble \mathcal{J} are computed as follows. Let us write $z(t; u) = z_{\text{cl}}(t) + \Delta z(t; u)$, where $\Delta z \rightarrow 0$ as $u \rightarrow -\infty$. The gradient flow equation in (2.3.6) becomes a partial differential equation of the parabolic type,

$$\frac{\partial}{\partial u} \Delta z(t; u) = -i \frac{\partial^2}{\partial t^2} \overline{\Delta z(t; u)}. \quad (2.3.8)$$

The boundary condition is $\Delta z(t; -\infty) = 0$, and the Dirichlet boundary condition $\Delta z(t_i; u) = \Delta z(t_f; u) = 0$ is also required. The basis of solutions $\Delta z(t; u)$ for (2.3.8) is given by

$$\Delta z_{\ell}(t; u) = e^{i\pi/4} \exp \left(\frac{\pi^2 \ell^2}{4(t_f - t_i)^2} u \right) \sin \left(\pi \ell \frac{t - t_i}{t_f - t_i} \right), \quad (2.3.9)$$

with $\ell \in \mathbb{Z}_{>0}$. As a result, any element of Lefschetz thimbles \mathcal{J} can be written as

$$z(t) = z_{\text{cl}}(t) + e^{i\pi/4} \sum_{\ell=1}^{\infty} a_{\ell} \sin \left(\pi \ell \frac{t - t_i}{t_f - t_i} \right), \quad (2.3.10)$$

where the coefficients a_{ℓ} are real values.

Since the Fourier transformation is unitary, the Jacobian associated with the change of integration variables does not appear. Indeed, the induced metric on the Lefschetz thimble \mathcal{J} from (2.3.5) is given by

$$ds^2|_{\mathcal{J}} = \sum_{\ell, \ell' \neq 0} da_{\ell} da_{\ell'} \int_{t_i}^{t_f} dt \sin\left(\pi \ell \frac{t - t_i}{t_f - t_i}\right) \sin\left(\pi \ell' \frac{t - t_i}{t_f - t_i}\right) = (t_f - t_i) \sum_{\ell \neq 0} (da_{\ell})^2. \quad (2.3.11)$$

The path-integral measure on the Lefschetz thimble \mathcal{J} is proportional to

$$\int_{\mathcal{J}} \mathcal{D}z = \mathcal{N} \int \prod_{\ell \neq 0} \sqrt{i} da_{\ell}, \quad (2.3.12)$$

with some normalization factor \mathcal{N} . Since $\mathcal{I}[z] - \mathcal{I}[z_{\text{cl}}]$ is a real-valued Gaussian functional of $\{a_{\ell}\}_{\ell}$, the real-time path integral becomes the Wiener integration on the Lefschetz thimble. It reads

$$\int_{\mathcal{J}} \mathcal{D}z \exp \mathcal{I}[z] = \mathcal{N} \prod_{\ell \neq 0} \left[\frac{\pi i}{\pi^2 \ell^2 / 2 (t_f - t_i)^2} \right]^{1/2} \exp \frac{\mathcal{I}[z_{\text{cl}}]}{\hbar}. \quad (2.3.13)$$

Since the computation of the normalization factor \mathcal{N} is standard, we do not give its details. The result is

$$\int_{\mathcal{J}} \mathcal{D}z \exp \mathcal{I}[z] = \sqrt{\frac{1}{2\pi i \hbar (t_f - t_i)}} \exp \frac{\mathcal{I}[z_{\text{cl}}]}{\hbar}. \quad (2.3.14)$$

It would be useful to point out the relationship of real- and imaginary-time path integrals from the viewpoint of Lefschetz thimbles. The imaginary-time formalism is also a mathematically rigorous approach to the path integral [77–79]. By formally replacing the real time t by the imaginary time $-i e^{i\varphi} t_{\varphi}$ with $0 \leq \varphi \leq \frac{\pi}{2}$, the classical action $\mathcal{I}[z]$ becomes positive definite at $\varphi = 0$. Therefore, the path integral at $\varphi = 0$ is well-defined as the Wiener integration. The complex time t_{φ} matches the real time t at $\varphi = \pi/2$, and we compute Lefschetz thimbles at each φ to show its connection to the real-time Lefschetz thimble. The path integral (2.2.1) becomes

$$K_{\text{free}}(x_f, -i e^{i\varphi} t_f; x_i, -i e^{i\varphi} t_i) = \int_{\mathcal{Y}} \mathcal{D}x \exp \left[-\frac{e^{-i\varphi}}{\hbar} \int dt_{\varphi} \frac{1}{2} \left(\frac{dx}{dt_{\varphi}} \right)^2 \right]. \quad (2.3.15)$$

It is now clear that this path integral with the imaginary time, $\varphi = 0$, is well-defined as a Wiener integral, and that the Lefschetz thimble at $\varphi = 0$ is nothing but the original integration cycle. In order to compute Lefschetz thimbles of (2.3.15) for general φ , we introduce

$$\mathcal{I}_{\varphi}[z(t_{\varphi})] = -\frac{e^{-i\varphi}}{\hbar} \int dt_{\varphi} \frac{1}{2} \left(\frac{dz}{dt_{\varphi}} \right)^2 \quad (2.3.16)$$

as a holomorphic functional of $z : [t_i, t_f] \rightarrow \mathbb{C}$ with $z(t_i) = x_i$ and $z(t_f) = x_f$. Since the classical solution is obtained by solving the same Euler–Lagrange equation (2.3.3), it is given by $z_{\text{cl}}(t_{\varphi})$ of (2.3.4). By repeating the same procedure in (2.3.8–2.3.10), the elements of the Lefschetz thimble \mathcal{J} around $z_{\text{cl}}(t_{\varphi})$ are obtained as

$$z(t_{\varphi}) = z_{\text{cl}}(t_{\varphi}) + e^{i\varphi/2} \sum_{\ell > 0} a_{\ell} \sin\left(\pi \ell \frac{t_{\varphi} - t_i}{t_f - t_i}\right). \quad (2.3.17)$$

At $\varphi = \pi/2$, as we remarked above, this is equal to the real-time Lefschetz thimble (2.3.10). Therefore, our results (2.3.7) and (2.3.14) have a clear relationship with the imaginary-time path integral of free theories by deforming Lefschetz thimbles smoothly as given in (2.3.17).

Free particle on a circle Using these results, the Lefschetz-thimble path integral can be computed also for quantum mechanics of a free particle on a circle S^1 . This is an interesting and simple example to learn about the path integral of quantum mechanics on a non-trivial topological space. We solve the Schrödinger equation (2.3.1) under the different boundary condition for $x \in S^1 = \mathbb{R}/2\pi\mathbb{Z}$. The wave functions obey

$$\psi(x + 2\pi, t) = e^{i\theta}\psi(x, t).$$

Here, θ is a real parameter.

The classical action in (2.2.1) of this system has a topological θ -term,

$$\mathcal{I}[z] = i \int dt \frac{1}{2} \left(\frac{dz}{dt} \right)^2 + i \frac{\hbar\theta}{2\pi} \int dz. \quad (2.3.18)$$

This is a holomorphic functional of $z : \mathbb{R} \rightarrow \mathbb{C}/2\pi\mathbb{Z}$ with the boundary condition $z(t_i) = x_i$ and $z(t_f) = x_f$. The topological term distinguishes the first homotopy class $\pi_1(\mathbb{R}/2\pi\mathbb{Z})$ of possible real-valued paths in the usual path integral. This is the same even after the complexification. The real-valued target space is embedded as $\mathbb{R}/2\pi\mathbb{Z} \subset \mathbb{C}/2\pi\mathbb{Z}$, and thus the topological term distinguishes $\pi_1(\mathbb{C}/2\pi\mathbb{Z}) (= \mathbb{Z})$ of complex paths.

Solving the same Euler–Lagrange equation (2.3.3) under the boundary condition $z(t_i) = x_i$ and $z(t_f) = x_f$ in $\mathbb{R}/2\pi\mathbb{Z} \subset \mathbb{C}/2\pi\mathbb{Z}$, the set of solutions $\{z_{\text{cl},w}(t)\}_{w \in \mathbb{Z}}$ are parametrized by the winding number $w \in \mathbb{Z}$;

$$z_{\text{cl},w}(t) = (x_f + 2\pi w - x_i) \frac{t - t_i}{t_f - t_i} + x_i. \quad (2.3.19)$$

Let \mathcal{J}_w be the Lefschetz thimble for $z_{\text{cl},w}(t)$, and its elements are calculable as (2.3.10). We can compute the path integral (2.2.1) of this system as we have done in (2.3.13), and the result is

$$K_{\text{free},\theta}(x_f, t_f; x_i, t_i) = \sum_{w \in \mathbb{Z}} \int_{\mathcal{J}_w} \mathcal{D}z \exp \frac{\mathcal{I}[z]}{\hbar} = \sqrt{\frac{1}{2\pi i \hbar (t_f - t_i)}} \sum_{w=-\infty}^{\infty} \exp \frac{\mathcal{I}[z_{\text{cl},w}]}{\hbar}. \quad (2.3.20)$$

Each classical solution has the intersection number 1, and thus all of them labeled by the topological number w must be summed up.

2.3.2 Harmonic oscillator

So far, path integrals of free particles are reconsidered by using the path integral on Lefschetz thimbles. Next, we compute quantum mechanics of a harmonic oscillator. The classical action is given by

$$\mathcal{I}[z] = i \int dt \left[\frac{1}{2} \left(\frac{dz}{dt} \right)^2 - \frac{1}{2} z^2 \right], \quad (2.3.21)$$

and we regard it as a holomorphic functional on \mathcal{X} . The Euler–Lagrange equation is

$$\frac{d^2 z(t)}{dt^2} = -z(t). \quad (2.3.22)$$

Thus, the classical solution is obtained as

$$z_{\text{cl}}(t) = \frac{x_f - x_i \cos(t_f - t_i)}{\sin(t_f - t_i)} \sin(t - t_i) + x_i \cos(t - t_i). \quad (2.3.23)$$

Let us assume that $t_f - t_i \neq n\pi$ for any $n \in \mathbb{Z}_{>0}$ in order to make (2.3.23) meaningful. Since this condition can be satisfied for generic initial and final times, t_i and t_f , the assumption is harmless in the following computations. The classical action is given as

$$\mathcal{I}[z_{\text{cl}}] = \frac{i}{2 \sin(t_f - t_i)} [(x_f^2 + x_i^2) \cos(t_f - t_i) - 2x_f x_i]. \quad (2.3.24)$$

In order to calculate the Lefschetz thimble, the gradient flow equation is considered,

$$\frac{\partial}{\partial u} \Delta z(t; u) = -i \left(\frac{\partial^2}{\partial t^2} + 1 \right) \overline{\Delta z(t; u)}. \quad (2.3.25)$$

Here, the complex path z is decomposed as $z(t; u) = z_{\text{cl}}(t) + \Delta z(t; u)$ with boundary conditions $\Delta z(t; -\infty) = 0$ and $\Delta z(t_i; u) = \Delta z(t_f, u) = 0$. The Lefschetz thimble is spanned by the following solutions Δz ,

$$\Delta z_n(t; u) = \begin{cases} e^{i\pi/4} \exp \left[\left(\left(\frac{\pi n}{t_f - t_i} \right)^2 - 1 \right) u \right] \sin \frac{n\pi}{t_f - t_i} (t - t_i), & (n\pi > (t_f - t_i)), \\ e^{-i\pi/4} \exp \left[\left(1 - \left(\frac{\pi n}{t_f - t_i} \right)^2 \right) u \right] \sin \frac{n\pi}{t_f - t_i} (t - t_i), & (n\pi < (t_f - t_i)). \end{cases} \quad (2.3.26)$$

Let ν denote the maximal non-negative integer smaller than $(t_f - t_i)/\pi$. Then, the Lefschetz thimble \mathcal{J} consists of complex paths,

$$z(t) = z_{\text{cl}}(t) + e^{-i\pi/4} \sum_{\ell=1}^{\nu} a_{\ell} \sin \frac{\pi \ell}{t_f - t_i} (t - t_i) + e^{i\pi/4} \sum_{\ell=\nu+1}^{\infty} a_{\ell} \sin \frac{\pi \ell}{t_f - t_i} (t - t_i), \quad (2.3.27)$$

with real-valued coefficients a_{ℓ} . Therefore, the path-integral measure on the Lefschetz thimble \mathcal{J} is given by

$$\int_{\mathcal{J}} \mathcal{D}z = \mathcal{N} \int \prod_{n=1}^{\nu} e^{-\frac{i\pi}{4}} da_n \prod_{m=\nu+1}^{\infty} e^{\frac{i\pi}{4}} da_m = e^{-i\pi\nu/2} \mathcal{N} \int \prod_{\ell=1}^{\infty} \sqrt{i} da_{\ell}. \quad (2.3.28)$$

Compared with that of the free particle case (2.3.12), the path-integral measure has an extra factor $\exp(-i\frac{\pi\nu}{2})$. This integer ν is called the Maslov–Morse index of the classical trajectory (see, e.g., Appendix 11 of Ref. [80]), and this represents the number of turning points during the time interval $[t_i, t_f]$.

We can readily compute the Feynman kernel $K_{\text{h.o.}}$ of the harmonic oscillator by using the Lefschetz thimble in the following way:

$$\begin{aligned} K_{\text{h.o.}}(x_f, t_f; x_i, t_i) &= \exp \left(\frac{\mathcal{I}[z_{\text{cl}}]}{\hbar} - i \frac{\pi\nu}{2} \right) \mathcal{N} \prod_{\ell} \int \sqrt{i} da_{\ell} \exp \left(- \left| \left(\frac{\pi \ell}{t_f - t_i} \right)^2 - 1 \right| a_{\ell}^2 \right) \\ &= \exp \left(\frac{\mathcal{I}[z_{\text{cl}}]}{\hbar} - i \frac{\pi\nu}{2} \right) \sqrt{\frac{1}{2\pi i \hbar (t_f - t_i)}} \prod_{\ell=1}^{\infty} \sqrt{\frac{1}{|1 - ((t_f - t_i)/\pi \ell)^2|}} \\ &= \sqrt{\frac{1}{2\pi i \hbar |\sin(t_f - t_i)|}} \exp \left(\frac{\mathcal{I}[z_{\text{cl}}]}{\hbar} - i \frac{\pi\nu}{2} \right). \end{aligned} \quad (2.3.29)$$

The normalization factor \mathcal{N} in this calculation is the same with that for the free particle. In the case of the harmonic oscillator, the Maslov–Morse index describes how the Lefschetz thimble intersects with the original space of paths.

2.4 Physical relevance of complex classical solutions

Since the original path integral is defined as the summation over real spacetime paths, it may not be clear what is the physical meaning of complex classical solutions. In this section, we demonstrate their possible usefulness by considering the tunneling or decaying process in the Minkowski path integral at the semi-classical level. This section is adapted from Ref. [76].

2.4.1 Complex classical solutions of the double-well potential

Tunneling is a characteristic process of quantum mechanics. Many dynamical phenomena are related to quantum tunneling; e.g., false vacua decays, bubble nucleation at first order phase transitions, domain wall fusions, etc. [81, 82]. Although quantum tunneling can be described very well by the WKB analysis of the Schrödinger equation, its understanding based on path integrals is not fully developed. This is mainly because any classical solutions cannot connect two classically stable regions when the potential barrier exceeds the energy. The purpose of this section is to open a new possibility to approach this problem by using the Lefschetz-thimble path integral, which shows the physical relevance of complex classical solutions.

Double-well potential As a model to discuss the tunneling, we consider the double-well quantum mechanics. In the real-time formalism, the classical action is

$$\mathcal{I}[z] = i \int dt \left[\frac{1}{2} \left(\frac{dz}{dt} \right)^2 - \frac{1}{2} (z^2 - 1)^2 \right]. \quad (2.4.1)$$

The Euler–Lagrange equation of (2.4.1) is

$$\frac{d^2 z}{dt^2} = -2z(z^2 - 1), \quad (2.4.2)$$

with the boundary condition $z(t_i) = x_i$ and $z(t_f) = x_f$. Instead of solving (2.4.2) directly, we use the conservation law of energy,

$$\left(\frac{dz}{dt} \right)^2 + (z^2 - 1)^2 = p^2, \quad (2.4.3)$$

where $p \in \mathbb{C}$ is a complex parameter. Using the Jacobian elliptic functions, the general solutions of (2.4.3) can be obtained as follows:

$$z(t) = \sqrt{\frac{p^2 - 1}{2p}} \operatorname{sd} \left(\sqrt{2p} t + c, \sqrt{\frac{1+p}{2p}} \right). \quad (2.4.4)$$

Here, c is an integration constant to satisfy the boundary condition $z(t_i) = x_i$, and $k = \sqrt{(1+p)/2p}$ is called an elliptic modulus. Our notation of elliptic functions is based on Chap. 22 of Ref. [83]. Later, we will find all the possible parameters p so as to satisfy $z(t_f) = x_f$.

Before calculating them, let us comment on properties of the double-well potential by observing qualitative behaviors of certain classical solutions. The potential term in (2.4.1) has two classical minima at $z = \pm 1$, and thus there are two different kinds of real solutions depending on their classical energies $p^2/2$. At high energies $p^2 > 1$, the energy exceeds the potential barrier at

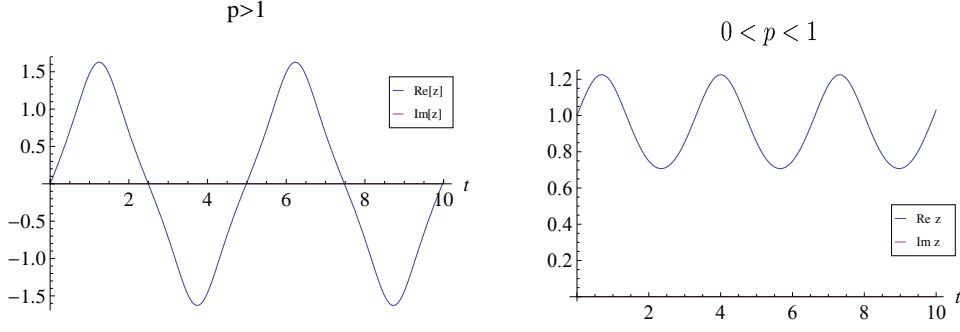


Figure 2.1: Typical behaviors of real classical solutions. The left and right panels show them for $p > 1$ and $p < 1$, respectively. (Figures are taken from Ref. [76].)

the origin $z = 0$, and thus the oscillation of the particle is given by the left panel of Fig. 2.1. In contrast, at low energies $p^2 < 1$, the potential traps the particle in one of the potential minima and its behavior is shown in the right panel of Fig. 2.1. At low energies, it is impossible to connect two potential minima if only the real-valued solutions are considered. There are also complex classical solutions, which properties will be discussed in the next subsection.

Classification of classical solutions By solving the boundary condition $z(t_i) = x_i$ and $z(t_f) = x_f$, we calculate the set of elliptic modulus k for classical solutions. Let us recall that the Jacobian elliptic function in (2.4.4) has the double half periodicities (see Sec. 22. 4 of Ref. [83]):

$$\text{sd}(z + 2K(k), k) = \text{sd}(z + 2iK(\sqrt{1 - k^2}), k) = -\text{sd}(z, k). \quad (2.4.5)$$

Here, $K(k)$ represents the complete elliptic integral given by $K(k) = \int_0^{\pi/2} d\theta / \sqrt{1 - k^2 \sin^2 \theta}$. The inverse elliptic function has ambiguities because of the above half-periodicities, and a label (n, m) must be introduced in order to remove them. The boundary condition is ($k' = \sqrt{1 - k^2}$)

$$x_f = \frac{kk'}{\sqrt{(2k^2 - 1)/2}} \text{sd} \left(\frac{t_f - t_i}{\sqrt{(2k^2 - 1)/2}} + \text{sd}^{-1} \left(\frac{\sqrt{(2k^2 - 1)/2}}{kk'} x_i, k \right), k \right), \quad (2.4.6)$$

and it can be solved as

$$2 \left(n K(k) + im K(\sqrt{1 - k^2}) \right) = \frac{t_f - t_i}{\sqrt{(2k^2 - 1)/2}} + \left\{ \text{sd}^{-1} \left(\frac{\sqrt{2k^2 - 1}}{\sqrt{2}kk'} x_i, k \right) - (-1)^{n+m} \text{sd}^{-1} \left(\frac{\sqrt{2k^2 - 1}}{\sqrt{2}kk'} x_f, k \right) \right\}. \quad (2.4.7)$$

It is possible to show that an appropriate subset of \mathbb{Z}^2 gives the set of classical solutions by using this relation (2.4.7)¹.

Intersection numbers n_σ and short-time asymptotic behaviors Since we have identified the set of complex classical solutions, we can calculate classical actions of those classical solutions. By taking the short-time limit $t_f - t_i \rightarrow +0$, the leading asymptotic behaviors of the classical action is easily calculable, and they provide useful information for intersection numbers n_σ .

¹The proof is given in Ref. [76].

Let us set $x_i = x_f = 0$ just for simplicity. Indeed, the leading short-time asymptotic behavior does not depend on x_i, x_f . For $(n, m) \in \mathbb{Z}$, we must solve the boundary condition (2.4.7) to find the elliptic modulus k :

$$\sqrt{\frac{2k^2 - 1}{2}} \left(nK(k) + imK(\sqrt{1 - k^2}) \right) = \frac{t_f - t_i}{2}. \quad (2.4.8)$$

In the limit $(t_f - t_i) \rightarrow +0$, the right-hand-side of (2.4.8) goes to zero. Therefore, the elliptic modulus k converges to $1/\sqrt{2}$ to satisfy this equality. We find from this observation that

$$k^2 = \frac{1}{2} + \left(\frac{t_f - t_i}{2(n + im)K(1/\sqrt{2})} \right)^2 + \mathcal{O}((t_f - t_i)^4). \quad (2.4.9)$$

If we adopt the standard choice of the branch cut, n must be a non-negative integer. The approximate expression for the classical solution is given by

$$z_{(n,m)}(t) \simeq \frac{(n + im)K(1/\sqrt{2})}{t_f - t_i} \text{sd} \left(2(n + im)K(1/\sqrt{2}) \frac{t - t_i}{t_f - t_i}, \frac{1}{\sqrt{2}} \right). \quad (2.4.10)$$

According to this formula of short-time behaviors, classical solutions are real-valued if and only if $nm = 0$. Other solutions take complex values. The total classical energy of this solution is given by

$$\frac{p_{(n,m)}^2}{2} = \frac{1}{2(2k^2 - 1)^2} \simeq 2 \left(\frac{(n + im)K(1/\sqrt{2})}{t_f - t_i} \right)^4. \quad (2.4.11)$$

Here, $p_{(n,m)}$ refers the parameter p of the label (n, m) , where $k = \sqrt{(1 + p)/(2p)}$. We can compute the leading term of the classical action \mathcal{I} in this limit only by evaluating the terms of $\mathcal{O}(1/(t_f - t_i)^4)$ in the Lagrangian. As a result, we find

$$\mathcal{I}[z_{(n,m)}] = i \int_{t_i}^{t_f} dt \left(\frac{p_{(n,m)}^2}{2} - (z_{(n,m)}^2 - 1)^2 \right) \simeq i \frac{2K(1/\sqrt{2})^4}{3} \frac{(n + im)^4}{(t_f - t_i)^3}. \quad (2.4.12)$$

The last expression can be obtained by using a formula in Sec. 23.14 of Ref. [83]. We can use these formulas also for the imaginary time by replacing t, t_i , and t_f by $-it, -it_i$, and $-it_f$.

By using this expression (2.4.12), we can derive a constraint on the intersection number $n_\sigma = \langle \mathcal{K}_\sigma, \mathcal{Y} \rangle$. The real-time classical action \mathcal{I} is purely imaginary for real-valued paths, and thus complex classical solutions with $\text{Re}(\mathcal{I}) > 0$ does not contribute to the Lefschetz-thimble decomposition of the path integral [64, 65]. Moreover, there are real-valued classical solutions when $nm = 0$, and we can conclude that their intersection numbers are unity, $n_\sigma = 1$. It means that there are infinitely many real-valued solutions, which contribute to the short-time asymptotic behavior of the path integral. In order to consider about complex classical solutions, we assume that $n > 0$ and $m \neq 0$. Using (2.4.12), we find the real part of \mathcal{I} as

$$\text{Re } \mathcal{I}[z_{(n,m)}] \simeq -\frac{8K(1/\sqrt{2})^4}{3(t_f - t_i)^3} nm(n^2 - m^2). \quad (2.4.13)$$

Since $\text{Re}(\mathcal{I})$ is positive for complex solutions with $nm(n^2 - m^2) < 0$, the intersection numbers n_σ of those classical solutions must be zero. On the other hand, complex solutions with $n > m > 0$

or $0 < n < -m$ may be able to contribute, although the intersection numbers for them are difficult to be determined. In order to find the intersection numbers for them, we must solve the gradient flow equations.

It is an open problem to compute undetermined coefficients n_σ . Moreover, the intersection number n_σ must be defined with an appropriate regularization, since we do not know the notion of the intersection between two infinite-dimensional manifolds. This problem always happens for interacting quantum field theories. Let N be the number of lattice sites when the lattice regularization is used, then the number of complex classical solutions is

$$(\deg V')^N = (\deg V - 1)^N, \quad (2.4.14)$$

where $\deg V$ denote the degree of the potential term V . Except for free field theories with $\deg V = 2$, the number of classical solutions grows exponentially with the lattice size N . Therefore, it is very difficult to solve the theory completely using the Lefschetz-thimble method. Nevertheless, this method sheds a new light on properties of the path integral. In this thesis, we will see that the structure of the sign problem is elucidated thanks to this technique.

2.4.2 Quantum tunneling in the real-time path integral

Let us try to describe the real-time tunneling phenomena by using the path integral on Lefschetz thimbles. Although our discussion in this part is incomplete because of limitation of our current knowledge on Lefschetz thimbles, this trial will make clear the physical relevance of complex classical solutions. Let us first review the consequence of quantum tunneling in the double-well potential. The ground and first excited states, ψ_0 and ψ_1 , are parity even and odd, respectively. In order to realize localized wave-functions in the semiclassical limit, we must consider the following superpositions, $\psi_\pm := (\psi_0 \pm \psi_1)/\sqrt{2}$. In the limit $\hbar \rightarrow 0$,

$$|\psi_\pm(x)|^2 \rightarrow \delta(x \mp 1). \quad (2.4.15)$$

These states ψ_\pm fail to be eigenstates of the Hamiltonian: A particle localized on a classical minimum transits to another classical minimum. This is the quantum tunneling, and its oscillation is characterized by the difference of two energies, $E_1 - E_0 \sim e^{-S_0/\hbar}$ ($S_0 > 0$).

In order to construct a classical solution describing the quantum tunneling, let us evaluate the long-time asymptotic behaviors of complex classical solutions. This would be important as a first step to develop our physical insight to describe the quantum tunneling using the real-time path integral.

For our purpose, it would be useful to start from instantons of the imaginary-time path integral, which play an important role to study the quantum tunneling. In Fig. 2.2 (a), instanton-like solutions in the imaginary-time formalism are shown for the case $x_i = -1$, $x_f = 1$ at the finite-time interval $t_f - t_i = -10i$. The two left figures, $(n, m) = (0, 0)$ and $(1, 0)$, show classical solutions with the one-instanton classical action $\mathcal{I}_0 = -4/3$ in the limit $t_f - t_i \rightarrow -i\infty$. The right figure, $(n, m) = (3, 0)$, shows a classical solution with $\mathcal{I} \simeq 3\mathcal{I}_0 (= -4)$, and thus it seems to be naturally interpreted as an instanton–anti-instanton–instanton process. Let us study an instanton by setting $(n, m) = (0, 0)$; then the boundary condition (2.4.7) becomes

$$-\frac{i}{2}T = \sqrt{\frac{2k^2 - 1}{2}} \operatorname{sd}^{-1} \left(\sqrt{\frac{2k^2 - 1}{2k^2(1 - k^2)}}, k \right) = -i\sqrt{\frac{1}{1 + p}} \operatorname{sn}^{-1} \left(\sqrt{\frac{1}{1 - p}}, \sqrt{\frac{1 - p}{1 + p}} \right). \quad (2.4.16)$$

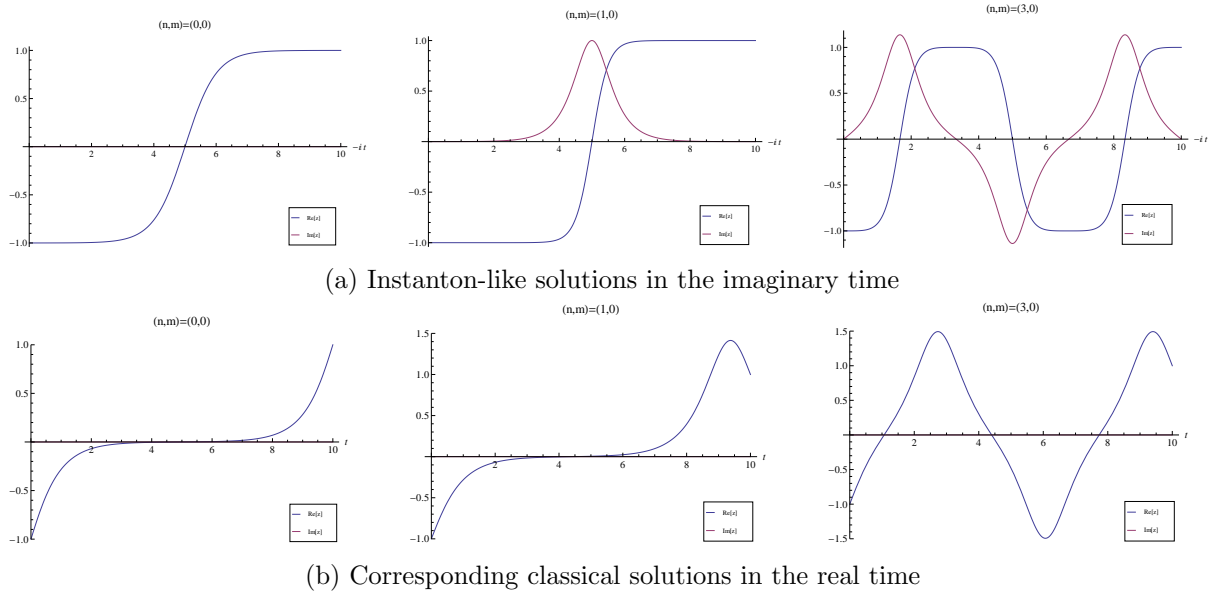


Figure 2.2: (a) Instanton-like solutions in the imaginary-time formalism. They correspond to $(n, m) = (0, 0)$, $(1, 0)$, and $(3, 0)$, respectively, for $x_i = -1$, $x_f = 1$, and $t_f - t_i = -10i$ in (2.4.7). (b) Corresponding solutions in the real-time formalism. Especially, the solution with $(n, m) = (0, 0)$ is very close to the unstable classical solution, and it seems to be natural to interpret them as sphalerons. (Figures are taken from Ref. [76].)

We rewrite the right hand side into a suitable form to study an asymptotic behavior in $p \rightarrow 0$ from the side $\text{Im } p > 0$ by using the formula given in Sec. 22. 17 of Ref. [83]. In the limit $T \rightarrow +\infty$, we can solve the asymptotic behavior of $p_{(0,0)} = 8i e^{-T}$, and obtain the well-known one-instanton solution ($t = -i\tau$):

$$z_{(0,0)}(\tau) = \sqrt{1 - p_{(0,0)}} \text{sn} \left(\sqrt{1 + p_{(0,0)}} \tau, \sqrt{\frac{1 - p_{(0,0)}}{1 + p_{(0,0)}}} \right) \simeq \tanh \tau. \quad (2.4.17)$$

By doing the same analysis for $(n, m) = (1, 0)$, we find that another instanton-like solution behaves as

$$\begin{aligned} z_{(1,0)}(\tau) &\simeq \sqrt{1 - p_{(1,0)}} \text{sn} \left(\sqrt{1 + p_{(1,0)}} \left(\tau + \frac{T}{2} - \frac{1}{2} \ln \frac{8}{p_{(1,0)}} - \frac{\pi}{4} i \right), \sqrt{\frac{1 - p_{(1,0)}}{1 + p_{(1,0)}}} \right) \\ &\simeq \tanh \left(\tau + \frac{\pi}{4} i \right), \end{aligned} \quad (2.4.18)$$

with $p_{(1,0)} \simeq -8e^{-T}$. This explains that both solutions has the same action, $\mathcal{I}_0 = -4/3$, in the limit $T \rightarrow \infty$.

In Fig. 2.2 (b), we show the corresponding classical solutions in the real-time formalism. These processes have sufficient energies, $p^2/2 \simeq 1/2$, to overcome the potential barrier classically. This always happen when the label (n, m) is fixed and the limit $t_f - t_i \rightarrow +\infty$ is considered: Since the label (n, m) designates the number of oscillation within the time interval $(t_f - t_i)$, the classical solution must stop almost at the top of the potential barrier. They might be related to unstable classical solutions, called sphalerons, in the long time limit $t_f - t_i \rightarrow \infty$, and then these processes are not suppressed in the semi-classical limit [84–86].

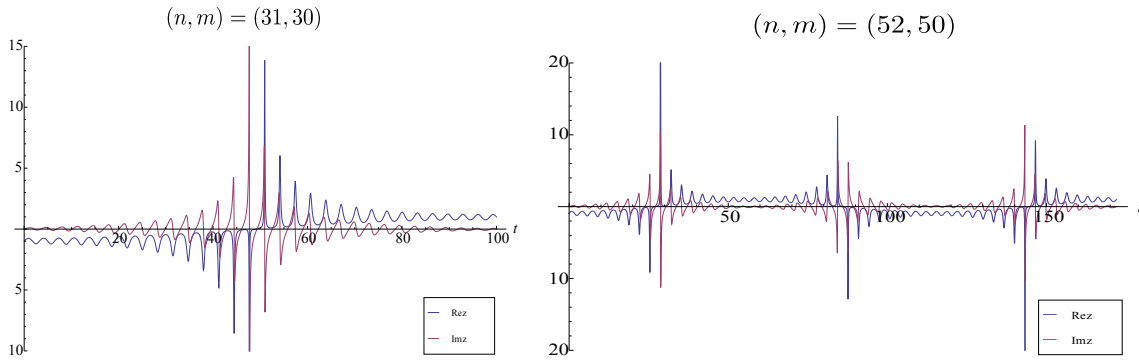


Figure 2.3: Highly-oscillatory complex solutions. In spite of their oscillatory nature, actions of these solutions can be comparable with multi-instanton actions. Indeed, we obtained $p_{(31,30)} = 0.427 + 0.155i$ and $\mathcal{I}_{(31,30)} = -1.072 + 0.007i$ for $(n, m) = (31, 30)$ with $(t_f - t_i) = 100$, and $p_{(52,50)} = 0.528 + 0.185i$ and $\mathcal{I}_{(52,50)} = -2.892 + 0.092i$ for $(n, m) = (52, 50)$ with $(t_f - t_i) = 172$, in these examples. (Figures are taken from Ref. [76].)

We expect that there exist complex classical solutions with $p \simeq 0$ because the quantum tunneling is a low-energy phenomenon [76, 87]. Indeed, if we perform the Wick rotation $\tau \mapsto it$ in (2.4.17) or (2.4.18), we can find classical solutions with $p^2 = 0$. Although they do not satisfy the boundary condition $x_i = -1$ and $x_f = 1$, it is intriguing to notice that those solutions oscillate with the period π . This observation may suggest that the quantum tunneling in our formulation is described by complex solutions with large labels (n, m) . Let us set the labels n, m of the order of $t_f - t_i$ (see Fig. 2.3). Such solutions can have finite classical actions with non-vanishing negative real parts, since they oscillate in the complexified configuration space (see Ref. [87] for detailed discussion on this property). Indeed, if n_σ of such solutions are nonzero, then their classical actions have negative real parts and those transition amplitudes are exponentially suppressed in the limit $\hbar \rightarrow 0$.

Therefore, it is very promising to conclude that infinitely many complex solutions including large (n, m) are significant in the real-time path-integral description of the quantum oscillation. This insight can be checked by computing intersection numbers n_σ of those complex solutions z_σ , and then we expect that those intersection numbers n_σ must be non-zero. Similar observation has been done also in the context of the particle production [88–90], and we will see its great importance to study the sign problem in Sec. 4.

2.5 Brief summary

In the present Chapter, we reviewed the foundation of the Picard–Lefschetz theory in order to apply it to the evaluation of oscillatory multiple integrals in Sec. 2.1 [62–66]. This naturally extends the idea of steepest descent methods (see Sec. 1.3 in the introduction). If the number of integration variables is one, we can easily designate the steepest descent path by using the stationary phase condition. When the number becomes larger, however, that condition is insufficient to pick up half-dimensional integration cycles. Mathematically, we can overcome this difficulty by using the Morse theory, and the steepest descent cycles can be found by solving the gradient flow in the complex phase space. Those steepest descent integration cycles are called Lefschetz thimbles, and they form a basis of a linear space.

In Sec. 2.2, we concretely describe the procedure to apply the Picard–Lefschetz theory to

the path integral in quantum mechanics following Refs. [64, 65]. After that, we confirm that the quantum equation of motion on each Lefschetz thimble. This explicitly shows that Lefschetz thimbles form a basis of complex vector space formed by the set of solutions of the Dyson–Schwinger equation. We also study the properties of the Gaussian fluctuation around complex classical solutions in a direct analytic way.

It is important and helpful to understand this method by applying it to the simplest examples of quantum mechanics. For that purpose, we compute the real-time Feynman kernels of free particles and the harmonic oscillator with this method in Sec. 2.3. The Lefschetz-thimble method reproduces the well-known results for these simple models, and we can confirm that this model works well. It is still interesting to see that we can compute Maslov–Morse index for the Feynman kernel of the harmonic oscillator without introducing explicit regulator explicitly.

In the following chapters, we will see the usefulness of the Lefschetz-thimble method to observe phase transitions and to understand the sign problem appearing in the statistical systems. In Sec. 2.4, we mention another possible direction for this method to be helpful. The real-time tunneling process can be studied using the WKB analysis, but its path-integral derivation is not fully understood. If we can understand it using path integral, then that computation is available not only in quantum mechanics but also in quantum field theory. As a prototype of this study, we consider the real-time tunneling of the double-well system based on the path integral on Lefschetz thimbles. We elucidate that the complex solutions play an important role there.

Chapter 3

Lefschetz-thimble approach to the spontaneous symmetry breaking

Chiral symmetry breaking is one of the characteristic nonperturbative phenomena of low-energy QCD. In this chapter, we study symmetry breaking phenomena for simple zero-dimensional toy models from the viewpoint of Lefschetz-thimble path integrals. In Sec. 3.1, the 0-dimensional Gross–Neveu model is considered for studying \mathbb{Z}_2 chiral symmetry breaking, and we directly relate the Lefschetz-thimble decomposition and the Lee–Yang zeros in the study of phase transitions. We develop a computational method to analyze the $O(n)$ -symmetric systems using Lefschetz thimbles in Sec. 3.2. This formalism is effectively used in Sec. 3.3 to study the $O(4)$ chiral symmetry breaking of the 0-dimensional Nambu–Jona-Lasinio model.

3.1 Spontaneous breaking of \mathbb{Z}_2 chiral symmetry

In this section, we discuss the spontaneous breaking of the discrete symmetry in the theory with chiral fermions based on the Lefschetz-thimble approach to the path integral. The discussion is adapted from Ref. [91].

3.1.1 0-dimensional Gross–Neveu model

We discuss a prototype of the spontaneous breaking of a discrete symmetry. For this purpose, we introduce the 0-dimensional analogue of the Gross–Neveu (GN) model [92]. This is the theory of 2-component Grassmann variables ψ_a and $\bar{\psi}_a$ with N colors ($a = 1, \dots, N$), and its partition function is defined by

$$Z_N(G, m) = \int d\bar{\psi} d\psi \exp \left(\sum_{a=1}^N \bar{\psi}_a (i\not{p} + m) \psi_a + \frac{G}{4N} \left(\sum_{a=1}^N \bar{\psi}_a \psi_a \right)^2 \right). \quad (3.1.1)$$

Here, $G > 0$ is a coupling constant that describes the four-fermion interaction, m is a bare fermion mass, and $\not{p} := \sum_{i=1}^2 p_i \sigma_i$ is a 2×2 matrix-valued constant that mimics the effect of nonzero-momentum modes in higher dimensions. In the massless case $m = 0$, the classical action in (3.1.1) is invariant under the \mathbb{Z}_2 chiral transformation defined by $\psi \mapsto \gamma_5 \psi$. Then, the theory has a discrete symmetry, and we will discuss its spontaneous breaking in the large- N limit.

In order to consider the path integral on Lefschetz thimbles for this system, we perform the Hubbard–Stratonovich transformation,

$$Z_N(G, m) = \sqrt{\frac{N}{\pi G}} \int d\bar{\psi} d\psi d\sigma \exp \left(\sum_{a=1}^N \bar{\psi}_a (i\not{p} + m + \sigma) \psi_a - \frac{N}{G} \sigma^2 \right) \quad (3.1.2)$$

$$= \sqrt{\frac{N}{\pi G}} \int_{\mathbb{R}} d\sigma [\det(i\not{p} + m + \sigma)]^N \exp \left(-\frac{N}{G} \sigma^2 \right). \quad (3.1.3)$$

Here, σ is an auxiliary bosonic field. The equation of motion tells us that σ is nothing but the fermion condensate,

$$\langle \sigma \rangle = \frac{G}{2N} \sum_a \langle \bar{\psi}_a \psi_a \rangle. \quad (3.1.4)$$

The partition function is given by

$$Z_N(G, m) = \sqrt{\frac{N}{\pi G}} \int_{\mathbb{R}} d\sigma e^{-NS(\sigma)}, \quad (3.1.5)$$

where the classical action is

$$S(\sigma) \equiv \frac{\sigma^2}{G} - \log[p^2 + (\sigma + m)^2] \quad (3.1.6)$$

with $p^2 \equiv p_1^2 + p_2^2 > 0$. Because of the fermion loop, the classical action has a logarithmic term. One of important purposes of this section is to demonstrate that the Lefschetz-thimble path integral is applicable also for such systems. According to the expression (3.1.5), we can see that the saddle-point analysis becomes accurate in the large- N limit. We separate the cases with $m = 0$ and $m > 0$ in the following, and the chiral limit $m = 0$ is discussed at first.

3.1.2 Structures of Lefschetz thimbles in massless case

Complex saddle points in the massless limit In order to understand the physical properties of the model, we assume that $G > 0$ for a moment and consider the case $m = 0$:

$$S(\sigma) = \frac{\sigma^2}{G} - \log(p^2 + \sigma^2). \quad (3.1.7)$$

The classical action in the chiral limit takes its minimum at $\sigma = 0$ for $0 < G \leq p^2$ and at $\sigma \neq 0$ for $G > p^2$. Because of this difference, the second-order phase transition associated with the chiral symmetry breaking occurs at $G = p^2$ in the limit $N \rightarrow \infty$.

In the following, we discuss this phase transition of the 0-dimensional GN model by using the path integral on Lefschetz thimbles. Because of the logarithmic singularity, the complexification of $\sigma \in \mathbb{R}$ is given by $z \in \mathbb{C} \setminus \{\pm ip\}$. The Morse function $\text{Re}(S(z))$ and the integrand $e^{-NS(z)}$ are well-defined as functions on $\mathbb{C} \setminus \{\pm ip\}$, and thus we can compute Lefschetz thimbles as one-dimensional manifolds in $\mathbb{C} \setminus \{\pm ip\}$. The complex saddle points are obtained as

$$0 = \frac{\partial S(z)}{\partial z} = \frac{2z}{G} - \frac{2z}{p^2 + z^2} \implies z = 0, \pm \sqrt{G - p^2}. \quad (3.1.8)$$

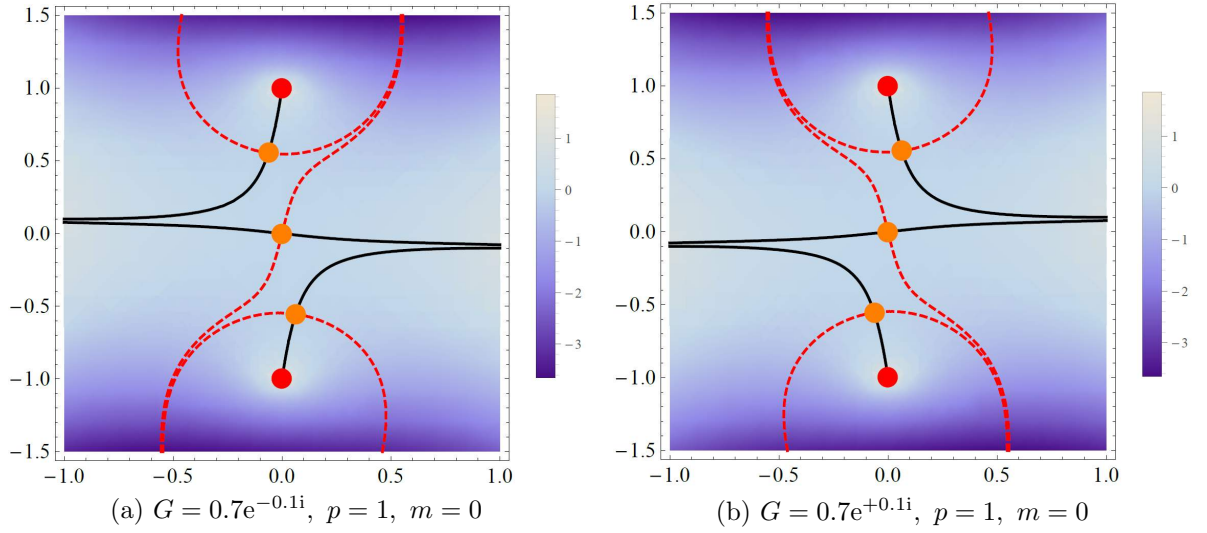


Figure 3.1: Lefschetz thimbles \mathcal{J} (black lines) and duals \mathcal{K} (dashed red lines) on the z -plane for the GN-like model in the chiral limit. The three orange blobs at $z = 0$ and $z_{\pm} = \pm i\sqrt{1-G}$ are the critical points of $S(z)$, while the two red blobs at $z = \pm i$ are the points where $S(z)$ diverges. The background color scale describes $\text{Re } S(z)$. (Figures are taken from Ref. [91].)

Let us set $z_{\pm} := \pm\sqrt{G-p^2}$. The three critical points coalesce at $G = p^2$. As a result, Lefschetz thimbles become ill-defined at $G = p^2$, and thus we hereafter put $G \neq p^2$.

When G is positive, all the classical actions at the saddle points $z = 0, z_{\pm}$ are real, and

$$S(0) - S(z_{\pm}) = -1 + \frac{p^2}{G} - \log \frac{p^2}{G} \geq 0. \quad (3.1.9)$$

The equality holds if and only if $G = p^2$. Therefore, if $z_{\pm} = \pm\sqrt{G-p^2}$ contribute, the symmetry is spontaneously broken in the limit $N \rightarrow \infty$. This can be judged by computing Lefschetz thimbles and their duals.

Before starting its computation, we must notice that $\text{Im } S(0) = \text{Im } S(z_{\pm}) = 0$ for real G and p . When this happens, the gradient flow may connect different complex saddle points, and the Lefschetz thimbles become ill-defined. This is a typical behavior when the theory is on the Stokes ray, as we have explained in Sec. 1.3 [64, 93]. In order to avoid this, we endow G with a phase factor $e^{i\theta}$ ($0 < |\theta| \ll 1$)¹. This solves the degeneracy of $\text{Im } S(z)$ among the critical points. We postpone more detailed analysis of Stokes jumps in the complex G -plane until Sec. 3.1.3.

Lefschetz thimbles in symmetric phase Let us consider the case where the chiral symmetry is unbroken, i.e., $G < p^2$. We compute Lefschetz thimbles and their duals for $p = 1$ and $G = 0.7e^{i\theta}$ with $\theta = \pm 0.1$, and the result is shown in Fig. 3.1. There are three Lefschetz thimbles $\mathcal{J}_0, \mathcal{J}_{z_+}$, and \mathcal{J}_{z_-} (solid black lines in Fig. 3.1) and three accompanying duals $\mathcal{K}_0, \mathcal{K}_{z_+}$, and \mathcal{K}_{z_-} (dashed red lines in Fig. 3.1). Lefschetz thimbles \mathcal{J}_{z_+} and \mathcal{J}_{z_-} terminate at branch points of the logarithmic term (red blobs), and this behavior is characteristic when fermions are included. Even though $S(z_{\pm}) \leq S(0)$, only the Lefschetz thimble \mathcal{J}_0 contributes since it has a nonzero intersection number. Thus, the symmetry is unbroken.

¹It is not appropriate to rotate the entire action as $S(z) \rightarrow e^{i\theta}S(z)$ because it allows the 2π -ambiguity in the imaginary part of $S(z)$ to induce an ambiguity in the *real part* of $e^{i\theta}S(z)$.

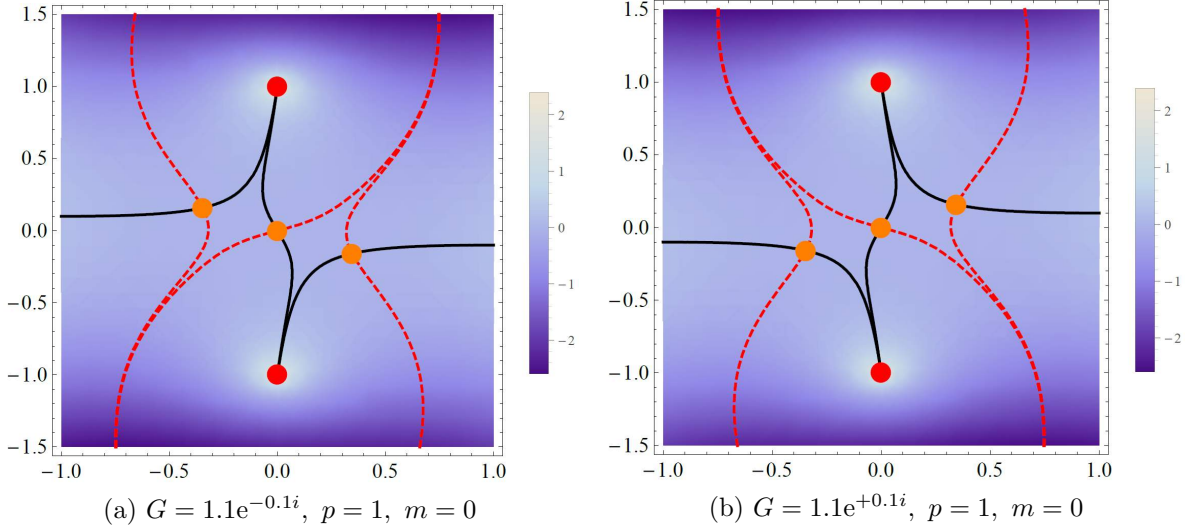


Figure 3.2: Same as Figure 3.1 but with $|G| = 1.1$. (Figures are taken from Ref. [91].)

Since $\theta = 0$ is a Stokes ray, $\mathcal{J}_{z_{\pm}}$ and \mathcal{K}_0 jump as θ crosses zero. This is a Stokes jumping, which is explained analytically in Sec. 1.3. When $|G| < p^2$, \mathcal{J}_0 does not jump at $\theta = 0$. The Stokes jump does not affect the computation of $Z_N(G, 0)$ itself at $\theta = 0$.

Lefschetz thimbles in symmetry-broken phase Next, let us set $|G| = 1.1$ and $p^2 = 1$ in order to study the symmetry broken phase. A small phase factor is attached to the four-fermion coupling G in order to circumvent the Stokes jump. Figure 3.2 shows the behavior of Lefschetz thimbles and their duals in this case. The structure of Lefschetz thimbles in Fig. 3.2 totally changes in comparison with Fig. 3.1. This difference plays an important role to describe the different phases, but the connection is not so straightforward, as we will see in Sec. 3.1.3.

In Fig. 3.2, all the dual thimbles \mathcal{K}_0 , \mathcal{K}_{z_+} , and \mathcal{K}_{z_-} (dashed red lines) intersect with \mathbb{R} . This is the biggest difference between Figs. 3.1 and 3.2, and it indicates that all three Lefschetz thimbles \mathcal{J}_0 , \mathcal{J}_{z_+} and \mathcal{J}_{z_-} contribute to $Z_N(G, 0)$. Indeed it is visually clear that the union of the three thimbles is homologically equivalent to \mathbb{R} . Since $S(z_{\pm}) \leq S(0)$ in the limit $\theta = 0$ according to (3.1.9), the behavior of $Z_N(G, 0)$ in the large- N limit is completely dominated by the nontrivial saddle points z_{\pm} . As a result of the spontaneous breaking of the \mathbb{Z}_2 chiral symmetry, fermions obtain a dynamical mass.

Let us analyze the Stokes jump in Figure 3.2 in more details. The orientation of $\mathcal{J}_{z_{\pm}}$ is fixed so that $\text{Re } z$ increases along the positive direction, and that of \mathcal{J}_0 is defined by the direction from $z = -ip$ to $z = +ip$ ($p > 0$). Then, the Lefschetz-thimble decompositions of the real integration cycle \mathbb{R} at $\theta = 0^{\mp}$ can be expressed as follows:

$$\mathbb{R} = \begin{cases} \mathcal{J}_{z_+} - \mathcal{J}_0 + \mathcal{J}_{z_-} & \text{for } \theta = 0^-, \\ \mathcal{J}_{z_+} + \mathcal{J}_0 + \mathcal{J}_{z_-} & \text{for } \theta = 0^+. \end{cases} \quad (3.1.10)$$

There are two remarks on (3.1.10).

- As we can see in Figs. 3.1 and 3.2, \mathcal{J}_0 does not jump across the Stokes ray. This fact can be intuitively understood: By definition of the gradient flow and (3.1.9), $\text{Re } S(z)|_{\mathcal{J}_0} \geq \text{Re } S(0) > \text{Re } S(z_{\pm})$. Any flows along \mathcal{J}_0 do not approach z_{\pm} .

- The integral coefficients of $\mathcal{J}_{z_{\pm}}$ in (3.1.10) do not jump across $\theta = 0$. This fact can be readily understood by applying the same argument to show that $\mathcal{K}_{z_{\pm}}$ do not jump across the Stokes ray. This is convincing also from the viewpoint of the asymptotic analysis. The asymptotic behavior of $Z_N(G, 0)$ for $G > p^2$ at $N \gg 1$ is given by the nontrivial saddle points $z = z_{\pm}$. Since $Z_N(G, 0)$ is a continuous function on G , the contributions from $\mathcal{J}_{z_{\pm}}$ cannot jump discontinuously in the large- N limit.

Both arguments have been presented in Sec. 3 of Ref. [64] in the context of bosonic integrals. Here, their usefulness is highlighted in a fermionic model.

3.1.3 Stokes phenomena and Lee–Yang zeros

Stokes lines So far, we have considered the phase transition of the 0-dimensional GN model, and the Stokes jumps for $G > 0$ are studied. Through those explicit calculations, the Lefschetz thimbles turn out to be well-defined if a small complex phase $e^{i\theta}$ ($0 < |\theta| \ll 1$) is attached to the four-fermion coupling G . Let us now study the Stokes phenomenon for a generic four-fermion coupling $G \in \mathbb{C}$.²

Before starting our analysis, let us remark a technical comment. In the original path-integral expression (3.1.5), the integral is convergent only when $\text{Re}(G) > 0$. Only after its computation, can we perform the analytic continuation to study $Z_N(G, 0)$ as an entirely analytic function in terms of G . Here, the Lefschetz-thimble decomposition again plays an essential role. Lefschetz thimbles connect nicely convergent regions to provide an integration cycle, and thus the path integral on Lefschetz thimbles always converges even if the coupling G is complexified. Thus, we can study analytic properties of $Z_N(G, 0)$ while keeping its path-integral expression by using Lefschetz thimbles.

Let us at first study the Stokes jumping in the complex G -plane. A Stokes jump can occur if multiple saddle points have the same imaginary part of the classical action. This condition reads

$$0 = \text{Im}[S(0) - S(z_{\pm})] = \text{Im}\left[-1 + \frac{p^2}{G} - \log \frac{p^2}{G}\right]. \quad (3.1.11)$$

Recall that $p^2 > 0$ by assumption. This condition can be solved by $G \in \mathbb{R}_{>0}$ or by $G \in \{p^2 r e^{i\phi} \mid r = \frac{\sin \phi}{\phi} \text{ and } -\pi < \phi \leq \pi\}$. We show the union of these curves by blue lines in Fig. 3.3, on which the Stokes jump happens. In the shaded area of Fig. 3.3, \mathcal{J}_0 is the unique Lefschetz thimble that contributes to $Z_N(G, 0)$ as in Fig. 3.1. Outside the shaded area, all the Lefschetz thimbles \mathcal{J}_0 and $\mathcal{J}_{z_{\pm}}$ contribute to $Z_N(G, 0)$ as in Fig. 3.2.

It must be pointed out that the Stokes jump at the boundary of the shaded area does not describe the phase transition directly. In the large- N limit, we find

$$Z_N(G, 0) \sim \begin{cases} \#e^{-NS(0)} & \text{inside the curve,} \\ \#e^{-NS(0)} + \#e^{-NS(z_+)} + \#e^{-NS(z_-)} & \text{outside the curve,} \end{cases} \quad (3.1.12)$$

with some coefficients symbolically represented by $\#$. In both cases, $Z_N(G, 0)$ is entirely dominated by the same term $e^{-NS(0)}$ since $\text{Re} S(0) < \text{Re} S(z_{\pm})$ on the boundary. Because of the continuity of $Z_N(G, 0)$, subdominant contributions can emerge across the Stokes ray but the dominant one cannot change discontinuously [93, 96].

²A complex four-fermion coupling appears in studies of the θ vacuum in QCD [94, 95].

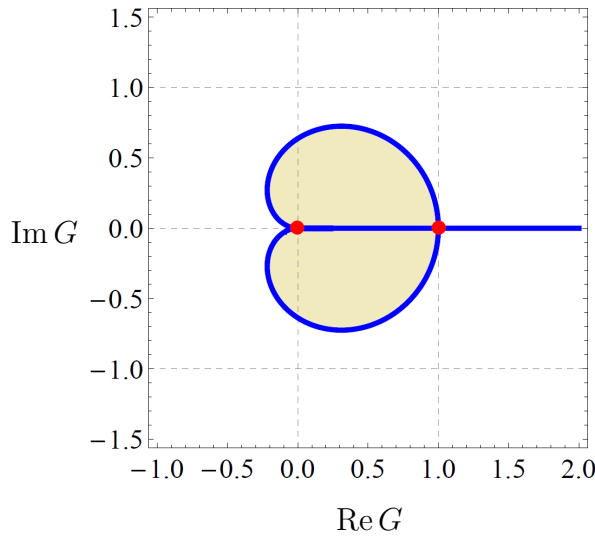


Figure 3.3: Stokes lines for the GN-like model with $p = 1$ and $m = 0$ (blue lines). The global topology of Lefschetz thimbles and their duals changes across the Stokes lines. In the shaded area, only \mathcal{J}_0 contributes to $Z_N(G, 0)$. Outside the shaded area, all the three thimbles contribute. (The Figure is taken from Ref. [91].)

Anti-Stokes lines and Lee-Yang zeros Let us now study the phase transition of the chiral symmetry breaking in the complex- G plane by applying the path integral on Lefschetz thimbles. In order to find the nonzero chiral condensate in the large- N limit, the following two conditions must be satisfied simultaneously:

1. $\mathcal{J}_{z_{\pm}}$ contribute to $Z_N(G, 0)$, and
2. $\text{Re } S(z_{\pm}) < \text{Re } S(0)$.

We have already seen that $\mathcal{J}_{z_{\pm}}$ contribute outside the shaded region in Fig. 3.3. The second condition says that $\mathcal{J}_{z_{\pm}}$ must give the dominant contributions in the large- N limit in order to break the chiral symmetry spontaneously. This is characterized by an *anti-Stokes line*, at which saddle points exchange their dominance. In the present model, the anti-Stokes line is specified by

$$0 \stackrel{!}{=} \text{Re} [S(0) - S(z_{\pm})] = \text{Re} \left[-1 + \frac{p^2}{G} - \log \frac{p^2}{G} \right]. \quad (3.1.13)$$

The anti-Stokes line is shown with the green curve in Fig. 3.4 for $p = 1$, together with the Stokes rays from Fig. 3.3.³ For this simple model, we can neglect the effect of fluctuations around saddle points z_{σ} , but in general we must compare the real part of “free energies” instead of those of classical actions. Outside the green anti-Stokes curve, chiral symmetry is spontaneously broken in the limit $N \rightarrow \infty$. The phase transition along the anti-Stokes curve is generally of first order because several saddle points exchange their dominance. The only exception is the point $G = p^2$, at which the phase transition is of second order. This happens since the Stokes and anti-Stokes curves intersect there, and the physical phase transition occurs at $G = p^2$.

³The anti-Stokes line actually extends into the interior of the Stokes curve, but this part is not shown in Fig. 3.4 because \mathcal{J}_{z_+} and \mathcal{J}_{z_-} do not contribute to $Z_N(G, 0)$ there.

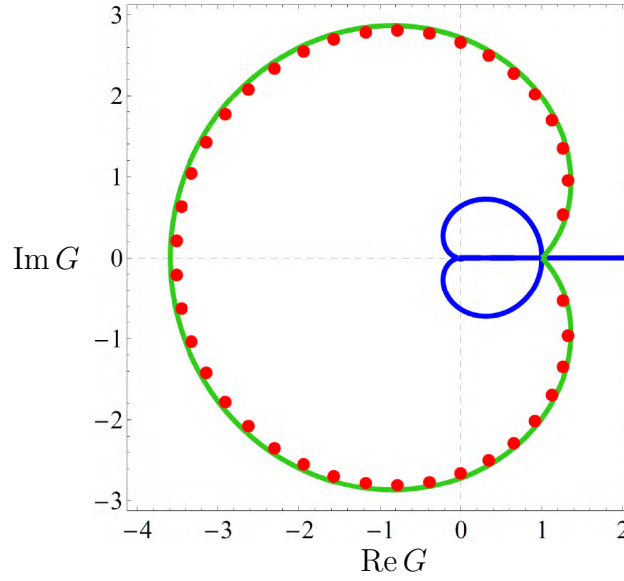


Figure 3.4: Anti-Stokes line for the GN-like model with $p = 1$ and $m = 0$ (green curve), overlaid with Lee-Yang zeros for $N = 40$ (red bullets) and the Stokes line in Figure 3.3 (blue curve). (The figure is taken from Ref. [91].)

Next, we would like to explore a connection between the anti-Stokes line and zeros of the partition function. According to the seminal work by Lee and Yang [97, 98], zeros of a finite-volume partition function in a complex parameter space, called *Lee-Yang zeros*, provides rich information on the phase transition in the thermodynamic limit. We here give only a brief review on this topic (See [99] for a review and [100–107]). Assume that we put a field theory on a compact torus so that the partition function $Z(\mu)$ is analytic in terms of a parameter μ , such as the chemical potential. If the physical parameter is real, the partition function is positive definite, and thus it has no zeros for $\mu \in \mathbb{R}$. However, if we allow the chemical potential μ being complex after computing the partition function, it can have zeros in $\mathbb{C} \setminus \mathbb{R}$, and let us denote them by $\{\mu_\alpha\}$, i.e.,

$$Z(\mu) \sim \prod_{\alpha} (\mu - \mu_{\alpha}). \quad (3.1.14)$$

Therefore, the partition function satisfies the following second-order differential equation:

$$\partial_{\mu} \bar{\partial}_{\mu} \ln Z(\mu) = \sum_{\alpha} \pi \delta^2(\mu - \mu_{\alpha}). \quad (3.1.15)$$

This is nothing but the Poisson equation in the complex μ -plane, and we can exploit our knowledge on electrostatics. In this interpretation, the number density $n = \frac{\partial}{\partial \beta \mu_R} \ln Z$ is nothing but the electric field in the real direction. In the decompactification limit, $V \rightarrow \infty$, the set of zeros $\{\mu_{\alpha}\}$ typically forms lines in the complex μ -plane. If the line of electric charges cuts the real μ -axis smoothly at $\mu_c \in \mathbb{R}$, the electric field $\partial_{\mu} Z$ has a discontinuous singularity at that point and thus the system experiences the first-order phase transition there. If the line ends or has a singularity, such as a kink, at some $\mu_c \in \mathbb{R}$, $\partial_{\mu} Z(\mu)$ is continuous but singular at $\mu = \mu_c$. This is nothing but the higher-order phase transition.

In order to see the connection between the anti-Stokes curve and Lee-Yang zeros, we can compare them directly. We can evaluate the partition function (3.1.1) or (3.1.5) explicitly to

find that

$$Z_N(G, 0) = p^{2N} \sum_{k=0}^N \binom{N}{k} \binom{2k}{k} k! \left(\frac{G}{4Np^2} \right)^k. \quad (3.1.16)$$

We show the numerical result of Lee–Yang zeros at $N = 40$ and $p = 1$ in Fig. 3.4. All Lee–Yang zeros are located in the vicinity of the anti-Stokes curve (green curve). As N become larger, we can observe that Lee–Yang zeros align on the anti-Stokes curve more and more densely. In the large- N limit, they form the anti-Stokes curve. Since the anti-Stokes curve in Fig. 3.4 has a kink at $G = p^2$, this phase transition is of higher order. By using (3.1.13), we can show that the anti-Stokes curve pinches the real axis at angle $\pm\pi/4$. According to a general theory of Lee–Yang zeros [99], this behavior characterizes the second-order phase transition with the mean-field critical exponent. This is exactly what happens in this model at $G = p^2$.

3.1.4 Structures of Lefschetz thimbles in a massive case

At the nonzero fermion mass $m \neq 0$, it breaks the \mathbb{Z}_2 chiral symmetry explicitly and the “chiral condensate” $\langle\sigma\rangle$ becomes nonzero even for small $G > 0$. Although a phase transition is absent at $m \neq 0$, it is still interesting to see the behavior of Lefschetz thimbles because of a crossover. Let us assume $m > 0$ in the following.

We complexify σ to $z \in \mathbb{C}$ in order to use the path integral on Lefschetz thimbles. The saddle points of $S(z)$ are obtained as solutions of

$$0 = \frac{\partial S(z)}{\partial z} = \frac{2z}{G} - \frac{2(z+m)}{p^2 + (z+m)^2}. \quad (3.1.17)$$

There are three solutions: One of them is always real, and other two solutions are both real or form a complex conjugate pair.

Figure 3.5 (left panel) is the phase diagram of the 0-dimensional Gross–Neveu model. The typical shape of $S(\sigma)$ is also shown in each region. Across the blue dashed line in Fig. 3.5 (left panel), the number of real saddle points changes. This line does not describe a phase transition, but a metastable state appears/disappears across this line. We schematically show in Fig. 3.5 (right panel) how complex saddle points move when the line of metastability is crossed from below by making the fermion mass m larger.

We can now elucidate the behavior of Lefschetz thimbles. Let us take two points **A** and **B** in Fig. 3.5 (left panel) that represent white and blue regions, respectively. In Fig. 3.6 (a), we draw the Lefschetz thimbles with $p = 1$ at the point **A**. It is interesting to see that no gradient flows connect distinct saddle points at $m \neq 0$ and $G < p^2$. We do not need to introduce a complex factor to G in this case, and the chiral condensate vanishes in the limit $m = 0$. Just as we saw in Fig. 3.1, we find that only one Lefschetz thimble (the real axis, \mathbb{R}) contributes to the partition function $Z_N(G, m)$. In the large- N limit, the saddle point associated with this Lefschetz thimble gives the expectation value of the chiral condensate $\langle\sigma\rangle \neq 0$.

Figure 3.6 (b) displays the Lefschetz thimbles at the point **B** in Fig. 3.5 (left panel) at $G = 1.5e^{-0.1i}$, $p = 1$, and $m = 0.05$. When $G > p^2$, the three saddle points lie on the real axis with $\text{Im } S = 0$. Therefore, $G \in \mathbb{R}$ is right on the Stokes ray and we must attach a complex phase to G .⁴ The overall structure of the thimbles is the same as in Fig. 3.2 at $m = 0$. Among the

⁴More generally, a Stokes phenomenon occurs *everywhere* in the shaded region of Fig. 3.5 (left panel), since all critical points are real there.

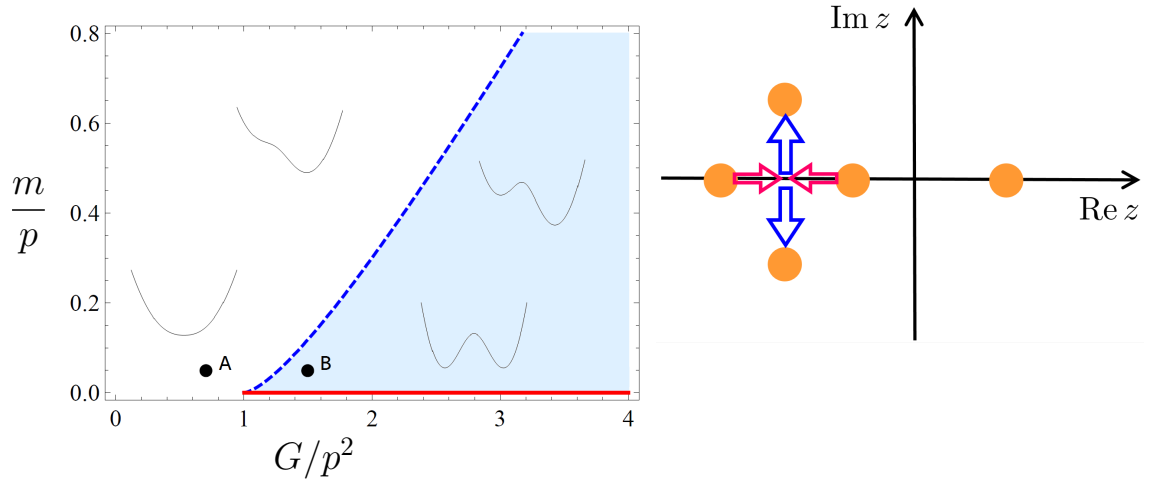


Figure 3.5: **Left:** Phase diagram of the GN model. The solid red line represents a first-order phase transition line. The dashed blue line is a limit of metastability (not a phase transition). Concerning the points **A** and **B**, see Figs. 3.6 (a) and (b). **Right:** The behavior of saddle points of $S(z)$ when m is increased at fixed $G > p^2$. As we move out of the blue region in the left panel upward, two of the three saddles on the real axis merge and then migrate into the complex plane. (Figures are taken from Ref. [91].)

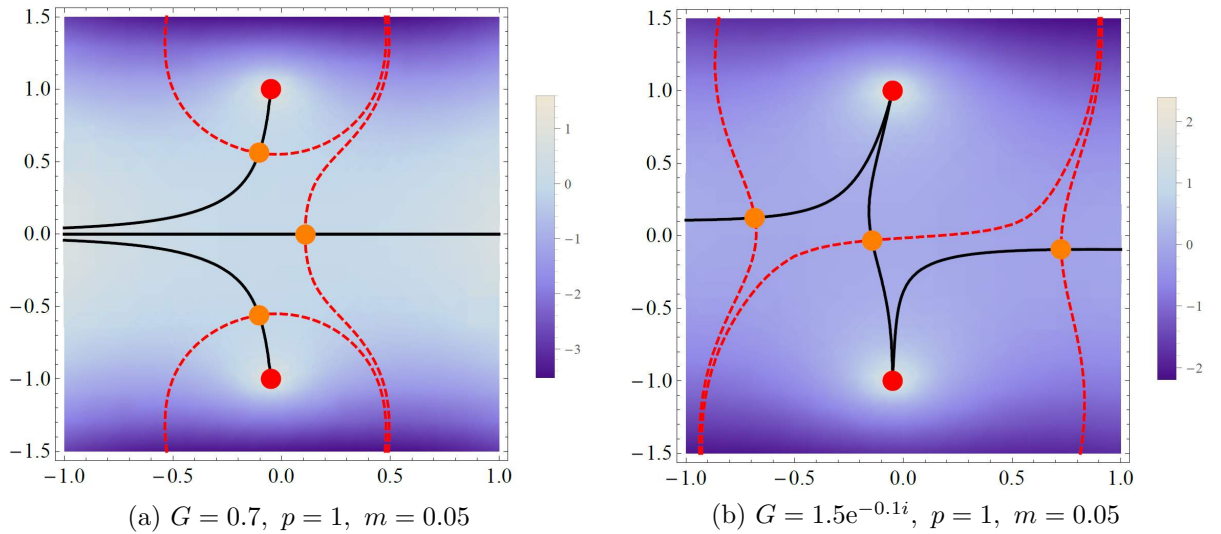


Figure 3.6: Same as Fig. 3.1 but with $G = 0.7$ and $m = 0.05$ (a), and at $G = 1.5e^{-0.1i}$ and $m = 0.05$ (b). (Figures are taken from Ref. [91].)

three saddle points, the right-most one has the smallest $\text{Re } S$ and hence governs the partition function and condensate at $N \gg 1$.

Between $G = 0.7$ and $G = 1.5$, the number of contributing Lefschetz thimbles changes from one to three. This change happens when the four-fermion coupling G traverses the blue dashed boundary in Fig. 3.5 (left panel). This is not a phase transition since the symmetry is always broken. From the viewpoint of asymptotic analysis, this is because the dominant saddle point always lies on $\mathbb{R}_{>0}$ and moves smoothly in terms of G . Although the Stokes line crosses the real axis in the complex G plane, the anti-Stokes line does not if $m \neq 0$.

3.2 Lefschetz thimbles with continuous symmetry

In order to study the phase transition associated with continuous symmetry breaking, we must develop a formalism to compute the Lefschetz thimble if continuous symmetry exists. If there exists a continuous symmetry, the classical solutions of the equation of motion are degenerate in general, which forbids us naive application of the Picard–Lefschetz theory described in Sec. 2.1. In Sec. 3.2.1, we give a brief review about the way to compute Lefschetz thimbles with continuous symmetry following Refs. [64, 65]. Applying this knowledge, a general way to compute Lefschetz thimbles with small explicit breaking terms is developed in Sec. 3.2.2. This extension is necessary to study the phase transition associated with the spontaneous continuous symmetry breaking, and we study its application to the Nambu–Jona-Lasinio-like model in Sec. 3.3. This section is adapted from Ref. [108].

3.2.1 Exact continuous symmetry

In this subsection, we review applications of Picard–Lefschetz theory to oscillatory integrations with unbroken continuous symmetries [64, 65]. For simplicity, we concretely consider a zero-dimensional $O(n)$ sigma model.

Let $\sigma = (\sigma_a)_a \in \mathbb{R}^n$, and then consider the Lie group action $O(n) \curvearrowright \mathbb{R}^n$ given by the defining representation. Using real anti-symmetric matrices ε , its infinitesimal transformation reads

$$\delta_\varepsilon \sigma_a = \varepsilon_{ab} \sigma_b \quad (3.2.1)$$

with $\varepsilon_{ab} = -\varepsilon_{ba} \in \mathbb{R}$. We consider a classical action function $S_0 : \mathbb{R}^n \rightarrow \mathbb{R}$, which is invariant under $O(n)$, and study the property of integration,

$$Z_0(\hbar) = \int_{\mathbb{R}^n} d^n \sigma \exp(-S_0[\sigma]/\hbar), \quad (3.2.2)$$

where $d^n \sigma = d\sigma_1 \wedge \cdots \wedge d\sigma_n$ is the Lebesgue measure.

Before trying Lefschetz-thimble methods to evaluate (3.2.2), let us consider the result of $O(n)$ symmetry directly. The $O(n)$ symmetry of the integrand and integration measure tells us that we can integrate radial and angular directions separately, $\mathbb{R}^n \setminus \{0\} \simeq \mathbb{R}_{>0} \times S^{n-1}$. By integrating out the angular directions S^{n-1} , we just need to evaluate the following integration

$$Z_0(\hbar) = \frac{2\pi^{n/2}}{\Gamma(n/2)} \int_0^\infty d\sigma \sigma^{n-1} \exp(-S_0(\sigma)/\hbar), \quad (3.2.3)$$

with $S_0(\sigma) = S_0[\sigma \hat{e}]$ (\hat{e} is an arbitrary unit vector), instead of the original one (3.2.2). This result can be interpreted from the viewpoint of the reduction of integration cycles: The quotient space $(\mathbb{R}^n \setminus \{0\})/O(n)$ is identified with the positive real axis $\mathbb{R}_{>0} (= (0, \infty))$. In the rest of this section, let us review a general way to derive (3.2.3) without taking quotients of the original integration cycle at first [64]. This consideration also provides a basic setup for taking into account the effect of explicit breaking terms.

We take the complexification \mathbb{C}^n of \mathbb{R}^n , and introduce the complex coordinate $\xi_a = \sigma_a + i\eta_a$.

The complexified space \mathbb{C}^n canonically admits the symplectic structure⁵,

$$\omega = -\frac{i}{2} d\xi_a \wedge d\bar{\xi}_a = d\eta_a \wedge d\sigma_a. \quad (3.2.4)$$

We exploit the fact that a gradient flow for the Lefschetz thimble can be viewed as a Hamiltonian flow of classical mechanics [64] (see also Sec. 2.1). Namely, we regard $\{\sigma_a\}_a$ as canonical coordinates and $\{\eta_a\}_a$ as conjugate momenta, and consider the Poisson bracket

$$\{f, g\} = \frac{\partial f}{\partial \sigma_a} \frac{\partial g}{\partial \eta_a} - \frac{\partial f}{\partial \eta_a} \frac{\partial g}{\partial \sigma_a}. \quad (3.2.5)$$

Let us consider the Hamilton mechanics with the Hamiltonian

$$H_0 = \text{Im } S_0[\xi], \quad (3.2.6)$$

then its equation of motion with respect to “time” t , $\frac{d\xi_a}{dt} = \{H_0, \xi_a\}$, is nothing but Morse’s downward flow equation,

$$\frac{d\xi_a}{dt} = \overline{\left(\frac{\partial}{\partial \xi_a} S_0[\xi] \right)}. \quad (3.2.7)$$

Along the flow, the Hamiltonian $H_0 = \text{Im } S_0[\xi]$ as well as other constants of motion are conserved, which plays a pivotal role in the following discussions.

The group action (3.2.1) must also be extended. The real orthogonal group $O(n)$ is complexified to the complex orthogonal group $O(n, \mathbb{C}) = \{A \in GL(n, \mathbb{C}) | AA^T = \text{id}_n\}$. The complexified group action $O(n, \mathbb{C}) \curvearrowright \mathbb{C}^n$ is given by

$$\delta_{\tilde{\varepsilon}} \xi_a = \tilde{\varepsilon}_{ab} \xi_b, \quad (3.2.8)$$

with $\tilde{\varepsilon}_{ab} = -\tilde{\varepsilon}_{ba} \in \mathbb{C}$. This extension makes clear that the $O(n)$ symmetry of the original action $S[\sigma]$ is extended to the $O(n, \mathbb{C})$ symmetry of $S[\xi]$. Under this $O(n, \mathbb{C})$ transformation, the symplectic structure (3.2.4) transforms as

$$\delta_{\tilde{\varepsilon}} \omega = \text{Im}(\tilde{\varepsilon}_{ab}) d\xi_a \wedge d\bar{\xi}_b, \quad (3.2.9)$$

and thus it is invariant if and only if the infinitesimal parameter $\tilde{\varepsilon}_{ab}$ is real. Therefore, the symmetry of this Hamilton system is $O(n)$, although the Hamiltonian H_0 is invariant under $O(n, \mathbb{C})$. Noether charges of the $O(n)$ symmetry are

$$J_{ab}(\xi, \bar{\xi}) = -\eta_a \sigma_b + \eta_b \sigma_a = \frac{i}{2} (\xi_a \bar{\xi}_b - \xi_b \bar{\xi}_a), \quad (3.2.10)$$

and a collection of these Noether charges is called the momentum map, denoted by $\mu_{O(n)}$ (See Appendix 5 of Ref. [80] for example). It is important to notice that $\mu_{O(n)} = 0$ on the original integration cycle \mathbb{R}^n . Since Lefschetz thimbles contributing to the original integration must be connected with \mathbb{R}^n via a flow [64], such Lefschetz thimbles must be connected to the region $\mu_{O(n)} = 0$ through $O(n, \mathbb{C})$ transformations.

⁵As we have already seen in Sec. 2.1, the complexified space must be chosen to admit a Kähler metric, which is a closed, non-degenerate two-form and compatible with the complex structure. The important point is that the Kähler metric uniquely provides the symplectic form ω in (3.2.4), which defines the Poisson bracket.

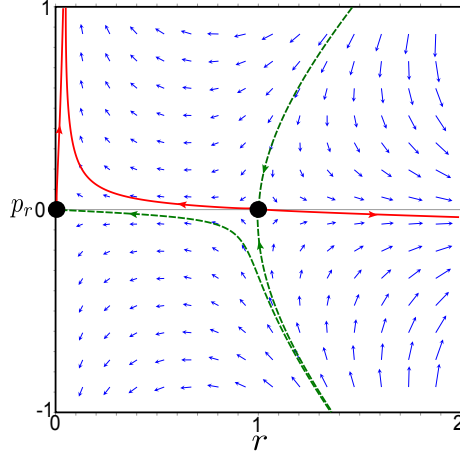


Figure 3.7: Downward flows of the reduced Hamilton system ($p_\theta = 0$) in the rp_r plane with $\alpha = 0.1$. Two points with $(r, p_r) = (0, 0)$ and $(1, 0)$ are critical points of this system. Red solid lines represent Lefschetz thimbles \mathcal{J} , i.e., downward flows emanating from critical points. Green dashed lines are their homological duals \mathcal{K} , which are characterized by downward flows getting sucked into critical points. Blue arrows show Hamiltonian vector fields. (The figure is taken from Ref. [108].)

Let us consider the simplest toy model:

$$S_0[\boldsymbol{\xi}] = \frac{e^{i\alpha}}{4}(\boldsymbol{\xi}^2 - 1)^2, \quad (3.2.11)$$

with $\boldsymbol{\xi}^2 = \xi_1^2 + \dots + \xi_n^2$. Here, α should be formally regarded as an infinitesimally small positive constant, $\alpha = 0^+$, which makes Lefschetz thimbles well-defined as integration cycles. Critical points of $S_0[\boldsymbol{\xi}]$ consist of two sets: One of them is the origin $O = \{\boldsymbol{\xi} = 0\}$, and the other one is a complex quadric,

$$Q^{n-1} = \{\boldsymbol{\xi} \in \mathbb{C}^n \mid \boldsymbol{\xi}^2 = 1\}. \quad (3.2.12)$$

Complexified critical orbits can be nicely parametrized with slow variables. For each symmetry, there exists two degenerate directions around a critical point: One of them is given by the symmetry transformation, and another one by the corresponding Noether charge. This provides the easiest way to find the set of zero modes, or slow variables, of the flow equation (3.2.7). Mathematically, this implies the fact that Q^{n-1} can be identified with the cotangent bundle T^*S^{n-1} of the hypersphere $S^{n-1} = \{\boldsymbol{\sigma} \in \mathbb{R}^n \mid \boldsymbol{\sigma}^2 = 1\}$. We will see this explicitly in Sec. 3.2.2 for $n = 2$.

Since the critical point $\boldsymbol{\xi} = 0$ is nondegenerate, we can compute its Lefschetz thimble in a usual way. Thus, we only explain how to construct the Lefschetz thimble of $\boldsymbol{\xi}^2 = 1$ in the following. Let us introduce the polar coordinate to emphasize the rotational symmetry by using the (point) canonical transformation: $r = |\boldsymbol{\sigma}|$ is a radial coordinate, $p_r = (\boldsymbol{\sigma} \cdot \boldsymbol{\eta})/|\boldsymbol{\sigma}|$ is its conjugate momentum, and $p_\theta^2 = \sum_{a < b} J_{ab}^2$ represents the total angular momentum. The $O(n, \mathbb{C})$ -invariant variable $\boldsymbol{\xi}^2$ can be written using r , p_r , and p_θ as

$$\begin{aligned} \boldsymbol{\xi}^2 &= (\boldsymbol{\sigma} + i\boldsymbol{\eta})^2 = (\boldsymbol{\sigma}^2 - \boldsymbol{\eta}^2) + 2i\boldsymbol{\sigma} \cdot \boldsymbol{\eta} \\ &= r^2 - \left(p_r^2 + \frac{p_\theta^2}{r^2}\right) + 2irp_r. \end{aligned} \quad (3.2.13)$$

The Hamiltonian H_0 of this $O(n)$ -invariant system becomes

$$H_0 = \frac{\sin \alpha}{4} \left\{ \left((r^2 - 1) - \left(p_r^2 + \frac{p_\theta^2}{r^2} \right) \right)^2 - 4r^2 p_r^2 \right\} + \cos \alpha r p_r \left((r^2 - 1) - \left(p_r^2 + \frac{p_\theta^2}{r^2} \right) \right). \quad (3.2.14)$$

Because of the conservation law of $\mu_{O(n)}$, dynamics of the rp_r direction is completely determined once p_θ^2 is fixed. The result for the case $p_\theta^2 = 0$ is shown in Fig. 3.7, and this is nothing but the downward flow for the integral (3.2.3) by regarding $r + ip_r$ as a complexified variable of σ : $H_0|_{p_\theta=0} = \text{Im}(S_0(r + ip_r))$ with $S_0(\sigma)$ in (3.2.3). The red and green dashed lines in Fig. 3.7 show downward flows emanating from and getting sucked into a critical point at $r + ip_r = 1$, respectively, which are given by

$$H_0(r, p_r)|_{p_\theta=0} = H_0(r = 1, p_r = 0)|_{p_\theta=0}. \quad (3.2.15)$$

Once the radial motion is totally determined in this way, the angular motion is automatically determined, and thus we can embed Fig. 3.7 into \mathbb{C}^n . In order to obtain an n -dimensional convergent integration cycle $\mathcal{J}_{r=1}^{\text{sym.}}$ and its dual $\mathcal{K}_{r=1}^{\text{sym.}}$, we must pick up other $(n-1)$ directions from the $2(n-1)$ -dimensional critical orbit $Q^{n-1}(= T^*S^{n-1})$.

The convenient procedure to construct the Lefschetz thimble, which is proposed in [64], is to rotate a red solid line of Fig. 3.7 by using $O(n)$ symmetry. As a result, the Lefschetz thimble $\mathcal{J}_{r=1}^{\text{sym.}}$ for $r = 1$ can be determined as the direct product of $S^{n-1} = \{\sigma^2 = 1\}$ and the red solid line at $r = 1$ of Fig. 3.7: $\mathcal{J}_{r=1}^{\text{sym.}} \simeq \mathbb{R} \times S^{n-1}$ as manifolds. Its dual $\mathcal{K}_{r=1}^{\text{sym.}}$ is given by rotating the green dashed line at $r = 1$ in Fig. 3.7 using the imaginary direction of $O(n, \mathbb{C})$. This procedure ensures that \mathcal{J} and \mathcal{K} intersect only at a single point. The reader may suspect that this construction contains some ambiguities because we pick up $(n-1)$ directions for $\mathcal{J}_{r=1}^{\text{sym.}}$ by hand, but we can argue that this is the unique choice up to continuous deformations [64]. In Sec. 3.2.2, we will see that this special choice of directions in T^*S^{n-1} is consistent with the downward flows with symmetry-breaking perturbations.

3.2.2 Continuous symmetry with small explicit breaking

In this section, we add a small symmetry-breaking term $\varepsilon \Delta S$, which lifts degeneracies of critical points and allows us to use the familiar formulation of Picard–Lefschetz theory. Global behaviors of downward flows are scrutinized, and use of approximate symmetries plays an essential role for computation of Lefschetz thimbles. This study can become important in studying spontaneous symmetry breaking using Lefschetz thimbles.

$O(2)$ sigma model We again consider the $O(2)$ linear sigma model with the action (3.2.11), and add a symmetry-breaking term,

$$\varepsilon \Delta S[\sigma] = \varepsilon e^{i\alpha} \sigma_1, \quad (3.2.16)$$

with $0 < \varepsilon \ll 1$. We formally set $\alpha = 0^+$ to simplify our argument. We study properties of the path integral

$$Z_\varepsilon(\hbar) = \int_{\mathbb{R}^2} d\sigma_1 d\sigma_2 \exp[-(S_0[\sigma] + \varepsilon \Delta S[\sigma])/\hbar], \quad (3.2.17)$$

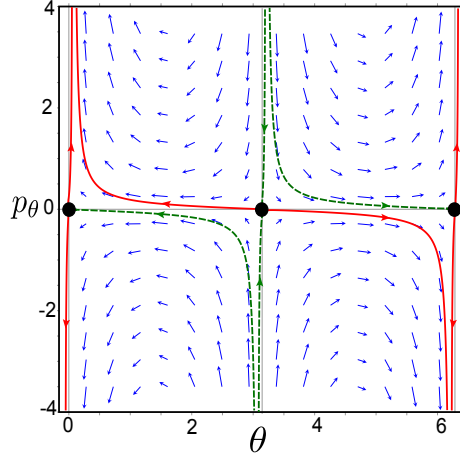


Figure 3.8: Flows projected on the critical orbit T^*S^1 induced by the perturbation $\varepsilon\Delta H$ at $\alpha = 0.1$. Black circles at $\theta = 0, \pi$ correspond to critical points in the perturbed system. Red solid and green dashed curves are downward flows projected onto T^*S^1 , which emanate from and get sucked into critical points, respectively. Blue arrows show Hamiltonian vector fields. (The figure is taken from Ref. [108].)

using Lefschetz-thimble techniques. We also discuss the relation to the previous formulation in the limit $\varepsilon \rightarrow +0$ at the end of this section.

Since there is an approximate $O(2)$ symmetry, the canonical transformation to the polar coordinate is again useful:

$$\begin{aligned} r &= \sqrt{\sigma_1^2 + \sigma_2^2}, & \theta &= \tan^{-1} \frac{\sigma_2}{\sigma_1}, \\ p_r &= \frac{\sigma_1\eta_1 + \sigma_2\eta_2}{\sqrt{\sigma_1^2 + \sigma_2^2}}, & p_\theta &= \eta_2\sigma_1 - \eta_1\sigma_2. \end{aligned} \quad (3.2.18)$$

Here, p_θ is nothing but the Noether charge J_{12} in (3.2.10), and $\omega = dp_r \wedge dr + dp_\theta \wedge d\theta$. Since $\xi^2 = r^2 + 2irp_r - (p_r^2 + p_\theta^2/r^2)$, the critical condition $\xi^2 = 1$ can be solved as $p_r = 0$ and $r^2 - (p_\theta/r)^2 = 1$. Now, the $O(2, \mathbb{C})$ critical orbit (3.2.12) is explicitly represented as

$$\left\{ \xi = \begin{pmatrix} r \cos \theta - i(p_\theta/r) \sin \theta \\ r \sin \theta + i(p_\theta/r) \cos \theta \end{pmatrix} \middle| r = \sqrt{(1 + \sqrt{1 + 4p_\theta^2})/2}, p_\theta \in \mathbb{R}, \theta \in [0, 2\pi) \right\}. \quad (3.2.19)$$

As we mentioned, this has a nice parametrization via slow variables θ and p_θ , which implies that $Q^1 \simeq T^*S^1$.

The Hamiltonian of this system is $H = H_0 + \varepsilon\Delta H = \text{Im}(S_0[\xi] + \varepsilon\Delta S[\xi])$. The unperturbed Hamiltonian is given in (3.2.14), and the perturbation is given by

$$\Delta H = \sin \alpha \, r \cos \theta + \cos \alpha \left(p_r \cos \theta - \frac{p_\theta}{r} \sin \theta \right). \quad (3.2.20)$$

This solves degeneracies of critical orbits, and validates Morse theory. However, naive computation of flows can easily fail, because of the remnant of symmetry. After giving a proposal for circumventing this technical difficulty, we show its origin by scrutinizing properties of downward flows through concrete computations.

Before starting explicit computations, we mention an efficient way to compute Lefschetz thimbles and comment on behaviors of downward flows. We advocate that the downward

flow on the nearly critical orbit T^*S^1 should be calculated at first: The perturbation ΔH breaks the $O(2, \mathbb{C})$ symmetry of $S[\xi]$, and it induces slow downward flows. The slow downward flow can be projected onto T^*S^1 , which is shown in Fig. 3.8. In order to get Fig. 3.8, the Hamilton mechanics in terms of θ and p_θ is solved under the critical condition $p_r = 0$ and $r = \sqrt{(1 + \sqrt{1 + 4p_\theta^2})}/2$. This step turns out to be important because Lefschetz thimbles in this system are two-dimensional cycles with one nearly flat direction: To create such integration cycles, downward flows must first travel slowly along red solid curves on T^*S^1 in Fig. 3.8 [up to $\mathcal{O}(\varepsilon)$]. After that, flows branch into radial directions, as will be confirmed below.

The critical condition $\partial S / \partial \xi_a = 0$ gives

$$(\xi_1^2 + \xi_2^2 - 1) \begin{pmatrix} \xi_1 \\ \xi_2 \end{pmatrix} + \begin{pmatrix} \varepsilon \\ 0 \end{pmatrix} = \begin{pmatrix} 0 \\ 0 \end{pmatrix}. \quad (3.2.21)$$

Critical points of this system consist only of three points: $(\xi_1, \xi_2) = (\varepsilon, 0)$, $(\pm 1 - \varepsilon/2, 0)$ up to $\mathcal{O}(\varepsilon)$, and two of them $(\pm 1 - \varepsilon/2, 0)$ correspond to black blobs in Fig. 3.8 ($\alpha = 0.1$ in this figure). In the polar coordinate (3.2.18), these solutions are $(r, \theta) = (\varepsilon, 0)$, $(1 - \varepsilon/2, 0)$, and $(1 + \varepsilon/2, \pi)$ with $p_r = p_\theta = 0$. Among these critical points, $\text{Re}(S_0 + \varepsilon \Delta S)$ takes the smallest value at $(r, \theta) = (1 + \varepsilon/2, \pi)$, and the largest value at $(r, \theta) = (\varepsilon, 0)$. Because of the symmetry-breaking term, the value at $(r, \theta) = (1 - \varepsilon/2, 0)$ is lifted up from the smallest one roughly by $2\varepsilon \cos \alpha (= 2\varepsilon)$.

The Hamiltonian H takes 0, $\sin \alpha$, and $-\sin \alpha$ at $(r, \theta) = (\varepsilon, 0)$, $(1 - \varepsilon/2, 0)$, and $(1 + \varepsilon/2, \pi)$, respectively, up to $\mathcal{O}(\varepsilon^0)$, and thus flows cannot connect distinct critical points. At $\alpha = 0^+$, however, these differences are infinitesimally small: The Lefschetz thimble $\mathcal{J}_{(1+\varepsilon/2, \pi)}$ around $(r, \theta) = (1 + \varepsilon/2, \pi)$ can pass infinitesimally close to other critical points.

The set of Hamilton equations (exactly at $\alpha = 0$) is

$$\frac{dr}{dt} = r \left(r^2 - \frac{p_\theta^2}{r^2} - 1 \right) - 3rp_r^2 + \varepsilon \cos \theta, \quad (3.2.22a)$$

$$\frac{dp_r}{dt} = (1 - 3r^2)p_r + p_r^3 - \frac{p_r p_\theta^2}{r^2} - \varepsilon \frac{p_\theta}{r^2} \sin \theta, \quad (3.2.22b)$$

$$\frac{d\theta}{dt} = -\frac{2p_r p_\theta}{r} - \varepsilon \frac{\sin \theta}{r}, \quad (3.2.22c)$$

$$\frac{dp_\theta}{dt} = \varepsilon \left(p_r \sin \theta + \frac{p_\theta}{r} \cos \theta \right). \quad (3.2.22d)$$

One can find a set of special solutions of this Hamiltonian system such that $p_r \equiv 0$ and $p_\theta \equiv 0$, which indeed automatically solves (3.2.22b) and (3.2.22d). Moreover, Figs. 3.7 and 3.8 imply that these are nothing but the conditions for a part of $\mathcal{J}_{(1+\varepsilon/2, \pi)}$. Solutions of (3.2.22) are shown in Fig. 3.9 (a) in the original coordinate system $(\sigma_1, \sigma_2) = r(\cos \theta, \sin \theta)$. Let us consider flows starting from $(r, \theta) = (1 + \varepsilon/2, \pi)$. Near the critical point, one solution flows along the radial direction in the same way as in the symmetric case, but there is another solution along the θ direction. Indeed, setting $r \simeq 1$ in (3.2.22c) gives

$$\theta(t) = \pm 2 \tan^{-1}(\exp(-\varepsilon t)). \quad (3.2.23)$$

According to (3.2.23), there is a downward flow rotating along a nearly flat direction with a time scale $1/\varepsilon$. For consistency with (3.2.22a), the radial direction should be fine-tuned so that $r(t) \simeq 1 - (\varepsilon/2) \tanh(\varepsilon t)$. After traveling along the critical orbit T^*S^1 in this way, flows branch

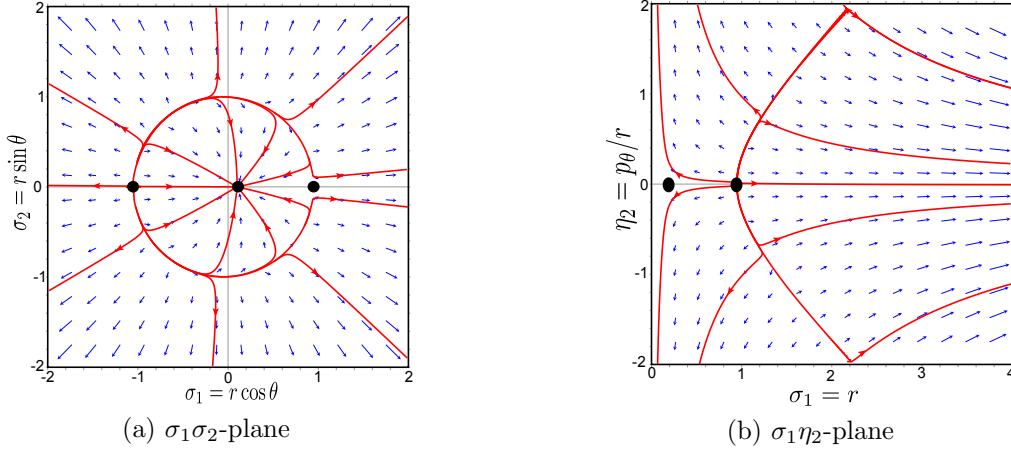


Figure 3.9: (a) Behaviors of downward flows (3.2.22) in the $\sigma_1\sigma_2$ -plane when $p_r = p_\theta = 0$ and $\alpha = 0$. Black blobs are critical points of the symmetry-broken system. Red arrowed curves are typical solutions starting from the global minimum $(r, \theta) = (1 + \varepsilon/2, \pi)$ with $0 < \varepsilon \ll 1$ ($\varepsilon = 0.1$ in this figure). Before branching into the r direction, every flow from the global minimum moves slowly along the critical orbit $r = 1$. (b) Behaviors of solutions to the differential equation (3.2.22) in the $\sigma_1\eta_2$ -plane with $\theta = p_r = 0$ when $\alpha = 0$. Red arrowed curves show typical solutions starting from $(r, \theta) = (1 - \varepsilon/2, 0)$ with $\varepsilon = 0.1$. (Figures are taken from Ref. [108].)

into radial directions, as shown in Fig. 3.9 (a): Drawing flow lines starting from a critical point is thus a difficult task, because we must designate the way of branching after traveling the nearly critical orbit just by tuning the initial condition. Since we already know the approximate flow on the critical orbit in Fig. 3.8; however, we can start and revert a flow from a point of branch in drawing Fig. 3.9 (a). This procedure does not require fine-tuning of initial conditions. All we have to confirm is that the reverted flow is drawn into the critical point.

Next, let us calculate the Lefschetz thimble $\mathcal{J}_{(1-\varepsilon/2,0)}$ for $(r, \theta) = (1 - \varepsilon/2, 0)$. For that purpose, we consider another set of special solutions of (3.2.22) by putting $\theta = 0$ and $p_r = 0$, which gives the red solid line around $\theta = 0$ in Fig. 3.8 (but at $\alpha = 0$). This condition solves (3.2.22b) and (3.2.22c) automatically. Behaviors of the downward flow in this plane are shown in Fig. 3.9, and, as we expected, downward flows go along the hyperbola $\sigma_1^2 - \eta_2^2 = 1$ at first, which is characterized by p_θ : Put $r(p_\theta) = \sqrt{\frac{1+\sqrt{1+4p_\theta^2}}{2}}$, and then (3.2.22d) gives

$$2r(p_\theta(t)) - \tanh^{-1}(1/r(p_\theta(t))) = \varepsilon t. \quad (3.2.24)$$

After this slow motion, they branch into the r direction in order to span a two-dimensional cycle $\mathcal{J}_{(1-\varepsilon/2,0)}$. In drawing red flow lines in Fig. 3.9 (b), we start and revert the flow from a point of branch instead of a point near the critical point. It would be really hard to control global behaviors of the flow if we compute the flow starting from a point near the critical point.

Now that we have identified local behaviors of Lefschetz thimbles around critical points and properties of approximate downward flows on the nearly critical orbit, we can comment on global behaviors of Lefschetz thimbles. This enables us to comment also on the relation of Lefschetz thimbles in symmetric and non-symmetric cases. The Lefschetz thimble $\mathcal{J}_{(1+\varepsilon/2,\pi)}$ around the global minimum goes away to infinities in the η_2 direction at $\theta = 0, 2\pi$ because there is another Lefschetz thimble $\mathcal{J}_{(1-\varepsilon/2,0)}$ at $\theta = 0$. See Fig. 3.10 for its schematic description. In order to recover the symmetric Lefschetz thimble $\mathcal{J}_{r=1}^{\text{sym.}}$ in the limit $\varepsilon \rightarrow +0$, we must sum $\mathcal{J}_{(1+\varepsilon/2,\pi)}$ and $\mathcal{J}_{(1-\varepsilon/2,0)}$ for the cancellation of the η_2 direction.

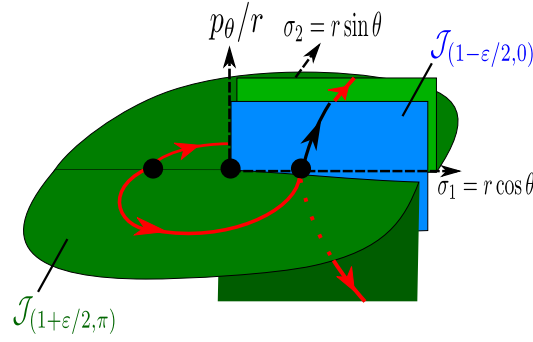


Figure 3.10: Schematic figure for a global structure of Lefschetz thimbles $\mathcal{J}_{(1+\epsilon/2, \pi)}$ and $\mathcal{J}_{(1-\epsilon/2, 0)}$ at $\alpha = 0^+$, which are shown with green and blue surfaces, respectively. In this limit, flows into p_r direction of these thimbles are quite small unless $r \simeq 0$, and we totally neglect that direction. Three black blobs represent critical points of this system, and arrowed lines show slow motion with time scale $1/\epsilon$ along the critical orbit T^*S^1 . (Figures are taken from Ref. [108].)

What is the fate of each Lefschetz thimble $\mathcal{J}_{(1+\epsilon/2, \pi)}$, $\mathcal{J}_{(1-\epsilon/2, 0)}$ in the limit $\epsilon \rightarrow +0$? Let us observe the behavior of integration on $\mathcal{J}_{(1-\epsilon/2, 0)}$ in the limit $\epsilon \rightarrow +0$:

$$\begin{aligned} & \int_{\mathcal{J}_{(1-\epsilon/2, 0)}} d^2z \exp[-(S_0 + \epsilon \Delta S)/\hbar] \\ & \sim -i \int_0^\infty \lambda d\lambda \exp\left(-\frac{(\lambda^2 - 1)^2}{4\hbar}\right) \int_{-\infty}^\infty d\phi \exp\left(-\frac{\epsilon\lambda}{\hbar} \cosh \phi\right). \end{aligned} \quad (3.2.25)$$

Here, we have set $\sigma_1 = \lambda \cosh \phi$ and $\eta_2 = \lambda \sinh \phi$. The integration of λ is convergent, but the integration of ϕ is logarithmically divergent in the limit $\epsilon/\hbar \rightarrow +0$:

$$\int d\phi \exp\left(-\frac{\epsilon\lambda}{\hbar} \cosh \phi\right) \sim 2 \ln \frac{\hbar}{\epsilon}. \quad (3.2.26)$$

This divergent integration is nothing but the integration along the critical orbit $r^2 - (p_\theta/r)^2 = 1$. Exactly the same divergence with the opposite sign appears in the integration over $\mathcal{J}_{(1+\epsilon/2, \pi)}$, and we must sum them up to construct a convergent integration cycle in the limit $\epsilon \rightarrow 0$. As already mentioned, this is identical with $\mathcal{J}_{r=1}^{\text{sym.}}$ in the homological sense:

$$\mathcal{J}_{r=1}^{\text{sym.}} = \mathcal{J}_{(1+\epsilon/2, \pi)} + \mathcal{J}_{(1-\epsilon/2, 0)}. \quad (3.2.27)$$

This might be surprising because the number of possible integration cycles changes under continuous change of parameters. Physically, this means that the number of solutions of the Dyson–Schwinger equation in the symmetric system is smaller than that of symmetry-broken systems.

We need to pick up half dimensions of the critical orbit T^*S^{n-1} in order to construct the middle-dimensional integration cycle $\mathcal{J}_{r=1}^{\text{sym.}}$. In the previous section, we picked them up in a specific way by rotating the Lefschetz thimble of the reduced system using the original symmetry $O(n)$. However, we did not explain why we cannot use imaginary directions of $O(n, \mathbb{C})$. The above analysis clearly shows the reason we have to give up imaginary directions of the complexified symmetry group: Otherwise, integration does not converge.

We have stuck to the case $\alpha = 0^+$ in order to draw Figs. 3.9, but our proposal is expected to be useful for generic α . Since there is no Stokes jump in $0 < \alpha < \pi$, Lefschetz thimbles at

generic α are continuous deformations of Fig. 3.10 (in \mathbb{C}^2). In order to span such cycles, flows should still go along T^*S^1 up to $\mathcal{O}(\varepsilon)$ as shown in Fig. 3.8, and branch. The dynamics after the branch can be solved in a similar way to get Fig. 3.7: $\varepsilon\Delta H$ is expected to be negligible since critical conditions are broken at $\mathcal{O}(\varepsilon^0)$.

Generalization to $O(n)$ sigma models Let us consider the case with general n . Then, the original action has $O(n)$ symmetry, and the perturbation ΔH breaks it into $O(n-1)$ symmetry:

$$O(n-1) = \left(\frac{1}{0} \middle| \frac{0}{O(n-1)} \right) \subset O(n). \quad (3.2.28)$$

In order to study the effect of ΔH , we need nothing new. All the computations are reduced into the ones in the case of $O(2)$ symmetry as follows.

Since the $O(n-1)$ symmetry is not broken at all, let us integrate it out. The $O(n-1)$ -invariant variables are

$$\sigma_1, \sigma'_2 = \sqrt{\sigma_2^2 + \cdots + \sigma_n^2}. \quad (3.2.29)$$

The original $O(n)$ invariance ensures that the unperturbed action can only depend on $\sigma_1^2 + \sigma_2'^2$. Therefore, even after $O(n-1)$ symmetry is reduced, there still exists a continuous $O(2)$ symmetry. Thus, all of the previous argument for the system with explicit symmetry breaking holds. After computing downward flows in the reduced system, we can construct Lefschetz thimbles by rotating them under $O(n-1)$.

3.3 Spontaneous breaking of $U(1)_A$ chiral symmetry

In this section, we discuss the spontaneous breaking of the continuous symmetry in the theory with chiral fermions based on the Lefschetz-thimble approach. The computational technique developed in Sec. 3.2 is applied in our analysis for that purpose. The discussion is adapted from Ref. [91].

3.3.1 0-dimensional Nambu–Jona-Lasinio model

Let us consider two zero-dimensional toy models which have continuous chiral symmetries. They are zero-dimensional analogues of the Nambu–Jona-Lasinio (NJL) model [45, 46]. The first model is defined by

$$Z_{U(1)} = \int d\bar{\psi} d\psi \exp \left(\sum_{a=1}^N \bar{\psi}_a (i\not{p} + m) \psi_a + \frac{G}{4N} \left\{ \left(\sum_{a=1}^N \bar{\psi}_a \psi_a \right)^2 + \left(\sum_{a=1}^N \bar{\psi}_a i\gamma_5 \psi_a \right)^2 \right\} \right). \quad (3.3.1)$$

We use the same symbols and variables as in (3.1.1). In the chiral limit $m = 0$, the classical action is invariant under the $U(1)_A$ chiral rotation $\psi \rightarrow e^{i\theta\gamma_5}\psi$ and $\bar{\psi} \rightarrow \bar{\psi}e^{i\theta\gamma_5}$. By introducing auxiliary fields σ and π via the Hubbard–Stratonovich transformation, we get

$$\begin{aligned} Z_{U(1)} &= \frac{N}{\pi G} \int_{\mathbb{R}^2} d\sigma d\pi [\det(i\not{p} + m + \sigma + i\gamma_5\pi)]^N \exp \left(-\frac{N}{G}(\sigma^2 + \pi^2) \right) \\ &= \frac{N}{\pi G} \int_{\mathbb{R}^2} d\sigma d\pi e^{-NS(\sigma, \pi)}, \end{aligned} \quad (3.3.2)$$

with

$$S(\sigma, \pi) \equiv -\log [p^2 + (\sigma + m)^2 + \pi^2] + \frac{\sigma^2 + \pi^2}{G}. \quad (3.3.3)$$

The $U(1)_A \cong O(2)$ transformation rotates (σ, π) as a two-dimensional vector, and it is a symmetry when $m = 0$. If we set $\pi = 0$ by using an $O(2)$ rotation, then the present model reduces to the GN-like model in Sec. 3.1 up to an $O(2)$ -invariant measure. This perspective will become important in analyzing the structure of Lefschetz thimbles later.

The second model we consider is defined by the partition function

$$Z_{SU(2)} = \int d\bar{\psi} d\psi \exp \left(\sum_{a=1}^N \bar{\psi}_a (i\not{p} + m) \psi_a + \frac{G}{4N} \left\{ \left(\sum_{a=1}^N \bar{\psi}_a \psi_a \right)^2 + \sum_{A=1}^3 \left(\sum_{a=1}^N \bar{\psi}_a i\gamma_5 \tau^A \psi_a \right)^2 \right\} \right), \quad (3.3.4)$$

where ψ and $\bar{\psi}$ are two-component Grassmann variables with $SU(2)$ flavors and N colors, $\{\tau^A\}$ are the Pauli matrices for $SU(2)$ flavors, and the summation over flavor indices is implicitly assumed. In the chiral limit $m = 0$, this model has an exact $SU(2)_R \times SU(2)_L$ symmetry, and it is explicitly broken to its diagonal component, $SU(2)_{L+R}$, by nonzero m . Again using the Hubbard–Stratonovich transformation,

$$Z_{SU(2)} = \left(\frac{N}{\pi G} \right)^2 \int_{\mathbb{R}^4} d\sigma d\pi_A [\det(i\not{p} + m + \sigma + i\gamma_5 \pi_A \tau^A)]^N \exp \left(-\frac{N}{G} (\sigma^2 + \pi_A^2) \right) \quad (3.3.5)$$

$$= \left(\frac{N}{\pi G} \right)^2 \int_{\mathbb{R}^4} d\sigma d\pi_A \{p^2 + (m + \sigma)^2 + \pi_A^2\}^{2N} \exp \left(-\frac{N}{G} (\sigma^2 + \pi_A^2) \right). \quad (3.3.6)$$

Under the chiral symmetry $SU(2)_L \times SU(2)_R \cong O(4)$, $(\sigma, \pi_1, \pi_2, \pi_3)$ rotates as a four-dimensional vector. One can rotate any such vectors to $(\sigma, 0, 0, \pi_3)$ by using an unbroken $SU(2)_{L+R} \cong SO(3)$ rotation. The resulting integral over σ and π_3 is essentially equivalent to the former model s(3.3.2) and does not entail a new feature. For this reason we focus on the first model in the following.

3.3.2 Structures of Lefschetz thimbles in the massless case

Let us consider the chiral limit $m = 0$ at first. In this case, there exists an exact continuous symmetry. Therefore, in order to apply the Lefschetz-thimble method for $Z_{U(1)}$, we have to decompose the original integration cycle \mathbb{R}^2 according to Sec. 3.2.1. Upon a complexification of variables, the action becomes

$$S(z, w) = -\log(p^2 + z^2 + w^2) + \frac{z^2 + w^2}{G}, \quad (3.3.7)$$

whose domain is $\{(z, w) \in \mathbb{C}^2 \mid z^2 + w^2 \neq -p^2\}$. The set of singular points of logarithm, $\{(z, w) \in \mathbb{C}^2 \mid z^2 + w^2 = -p^2\}$, forms a two-dimensional surface in \mathbb{C}^2 . It is equal to the $O(2, \mathbb{C})$ -orbit of the singular points $(z, w) = (\pm ip, 0)$ of the massless GN-like model.

The flow equation reads⁶

$$\frac{d\bar{z}}{d\tau} = \frac{2z}{p^2 + z^2 + w^2} - \frac{2z}{G} \quad \text{and} \quad \frac{d\bar{w}}{d\tau} = \frac{2w}{p^2 + z^2 + w^2} - \frac{2w}{G}. \quad (3.3.8)$$

⁶In this section, the definition of the fictitious time τ has an extra minus sign.

It is important to point out that the symmetry of this flow equation is $O(2)$ instead of $O(2, \mathbb{C})$, although the classical action is invariant under $O(2, \mathbb{C})$ (see Sec. 3.2.1).

The set of saddle points is obtained by solving (3.3.8) with

$$\frac{d\bar{z}}{d\tau} = \frac{d\bar{w}}{d\tau} = 0. \quad (3.3.9)$$

Let us put $G \neq p^2$ in order to circumvent accidental degeneracy of complex saddle points. The set of saddle points in \mathbb{C} consists of two connected components:

$$C_0 := \{(0, 0)\} \quad \text{and} \quad C_1 := \{(z, w) \in \mathbb{C}^2 \mid z^2 + w^2 = G - p^2\}. \quad (3.3.10)$$

C_1 is equal to the $O(2, \mathbb{C})$ critical orbit of the saddle points $(\pm\sqrt{G-p^2}, 0)$ in the 0-dimensional massless GN model. It crosses the real plane \mathbb{R}^2 if $G-p^2 > 0$ but has no intersection otherwise.

We now construct Lefschetz thimbles \mathcal{J}_σ and their duals \mathcal{K}_σ ($\sigma = 0, 1$) for saddle points C_0 and C_1 . Since $C_0 = \{(0, 0)\}$ is a non-degenerate saddle point, we can compute \mathcal{J}_0 and \mathcal{K}_0 in the standard manner; $\text{Re } S(z, w)$ increases in two directions and decreases in the other two directions around C_0 . Since the gradient flow preserves the $O(2)$ symmetry, we can obtain \mathcal{J}_0 by rotating a Lefschetz thimble in the GN-like model with the $O(2)$ action:

$$\mathcal{J}_0 = \left\{ \begin{pmatrix} z \\ w \end{pmatrix} = \begin{pmatrix} \cos \theta & -\sin \theta \\ \sin \theta & \cos \theta \end{pmatrix} \begin{pmatrix} z' \\ 0 \end{pmatrix} \mid -\pi < \theta \leq \pi \text{ and } z' \in \mathcal{J}_0|_{\text{GN}} \right\}. \quad (3.3.11)$$

The dual thimble \mathcal{K}_0 can be computed in the same way.

Since C_1 is the set of degenerate saddle points, we need a special treatment to construct \mathcal{J}_1 . The general method given in Ref. [64] is already explained in Sec. 3.2.1, but we try to compute it in a more concrete manner. Let us pick up a point $(\sqrt{G-p^2}, 0) \in C_1$. Two directions along C_1 give two null eigenvectors of the Hessian matrix of S , and other two directions are non-degenerate. For non-degenerate directions, we can construct the flow lines, and the flow line emanating from $(\sqrt{G-p^2}, 0)$ can be identified as a Lefschetz thimble \mathcal{J}_{z_+} of the 0-dimensional GN model. Recalling that the flow respects the $O(2)$ symmetry, \mathcal{J}_1 can simply be obtained as an $O(2)$ revolution of \mathcal{J}_{z_+} in Sec. 3.1. We thus conclude that

$$\mathcal{J}_1 = \left\{ \begin{pmatrix} z \\ w \end{pmatrix} = \begin{pmatrix} \cos \theta & -\sin \theta \\ \sin \theta & \cos \theta \end{pmatrix} \begin{pmatrix} z'' \\ 0 \end{pmatrix} \mid -\pi < \theta \leq \pi \text{ and } z'' \in \mathcal{J}_{z_+}|_{\text{GN}} \right\}. \quad (3.3.12)$$

Since the Noether charge μ is conserved along a flow, μ vanishes everywhere on \mathcal{J}_1 .

By our construction, it is clear that behaviors of the Lefschetz thimbles, (3.3.11) and (3.3.12), in terms of $G \in \mathbb{C}$ can be learned from Sec. 3.1 without additional calculation:

- \mathcal{J}_0 and \mathcal{J}_1 jump on the Stokes lines (blue lines) in Fig. 3.3.
- For G inside the shaded area of Fig. 3.3, only \mathcal{J}_0 contributes to $Z_{U(1)}$.
- For G outside the shaded area of Fig. 3.3, both \mathcal{J}_0 and \mathcal{J}_1 contribute to $Z_{U(1)}$.
- For G inside the anti-Stokes line (green line) in Fig. 3.4, \mathcal{J}_0 dominates \mathcal{J}_1 at large N . Their dominance is exchanged as G moves out across the anti-Stokes line.

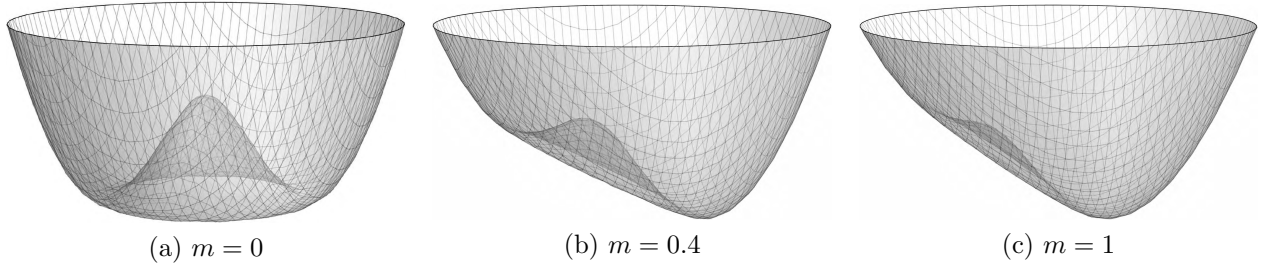


Figure 3.11: Snapshots of the action $S(\sigma, \pi)$ in (3.3.3) for varying m at $G = 3$ and $p = 1$. The number of saddle points jumps from 3 to 1 at $m \simeq 0.724$. (Figures are taken from Ref. [91].)

- Spontaneous breaking of the $O(2)$ chiral symmetry is a first-order phase transition for generic complex couplings G . For physical $G \in \mathbb{R}_{>0}$, this is the second-order phase transition at $G = p^2$.

As a conclusion, the Lefschetz thimbles for the 0-dimensional massless NJL model (3.3.2) can be obtained by $O(2)$ revolutions of the Lefschetz thimbles for the 0-dimensional massless GN model (3.1.5). Therefore, we can immediately derive many properties of the chiral symmetry breaking for the NJL-like model thanks to the knowledge of the GN-like model.

3.3.3 Massive case

With nonzero fermion mass $m \neq 0$, the $O(2)$ chiral symmetry is explicitly broken. The behaviors of the NJL-like model becomes qualitatively similar to those of the massive GN-like model. Because of the absence of the continuous symmetry, there are only three saddle points $\{(z, w) = (z_\sigma, 0) \mid \sigma = 0, \pm\}$, where $\{z_\sigma\}_{\sigma=0,\pm}$ are the three solutions to (3.1.17), and a critical manifold (3.3.10) has different meaning. Associated with three non-degenerate saddle points, there are three Lefschetz thimbles \mathcal{J}_σ and their dual thimbles \mathcal{K}_σ .

We have already discussed the dependence of $\{z_\sigma\}_\sigma$ on G and m in Sec. 3.1.4 (see, e.g., Fig. 3.5). For sufficiently large fermion mass m , there is only one saddle point in the real space $(\sigma, \pi) \in \mathbb{R}^2$, and only one Lefschetz thimble contributes to $Z_{U(1)}$ (see Fig. 3.11 (c)). At small m or large G , all the three Lefschetz thimbles contribute (see Figs. 3.11 (a) and (b)). In the latter case, the Stokes phenomenon occurs among the three thimbles, but it is hard to visualize as it occurs in \mathbb{C}^2 .

Let us try to calculate Lefschetz thimbles for sufficiently small m . This helps us to visualize the Stokes jump in the NJL-like model. So far, we have emphasized similarities of the NJL-like model to the GN-like model. However, the flow equation of the NJL-like model has a unique character: There are quasi-fixed points of the flow equation because of the approximate $O(2, \mathbb{C})$ symmetry of S (see Sec. 3.2.2). That is, the flow along the critical orbit C_1 in the massless case is extremely slow compared with that of other directions.

For simplicity, we put $p = 0$ in the following (This simplification in the GN-like model is discussed in Ref. [91]). Here we summarize main features of the NJL-like model at $p = 0$.

- $m = 0$: The Lefschetz thimble \mathcal{J}_0 in (3.3.11) disappears at $p = 0$ as $\mathcal{J}_0|_{\text{GN}}$ no longer exists. This is because the singularity of logarithm exists at the origin at $p = 0$. Therefore, \mathcal{J}_1 is the unique Lefschetz thimble. From (3.3.12), we find $\mathcal{J}_1 = \mathbb{R}^2 \setminus \{(0, 0)\}$.
- $m > 0$: There are only two saddle points at $(z, w) = \left(\frac{-m \pm \sqrt{m^2 + 4G}}{2}, 0 \right) =: (z_\pm, 0)$,

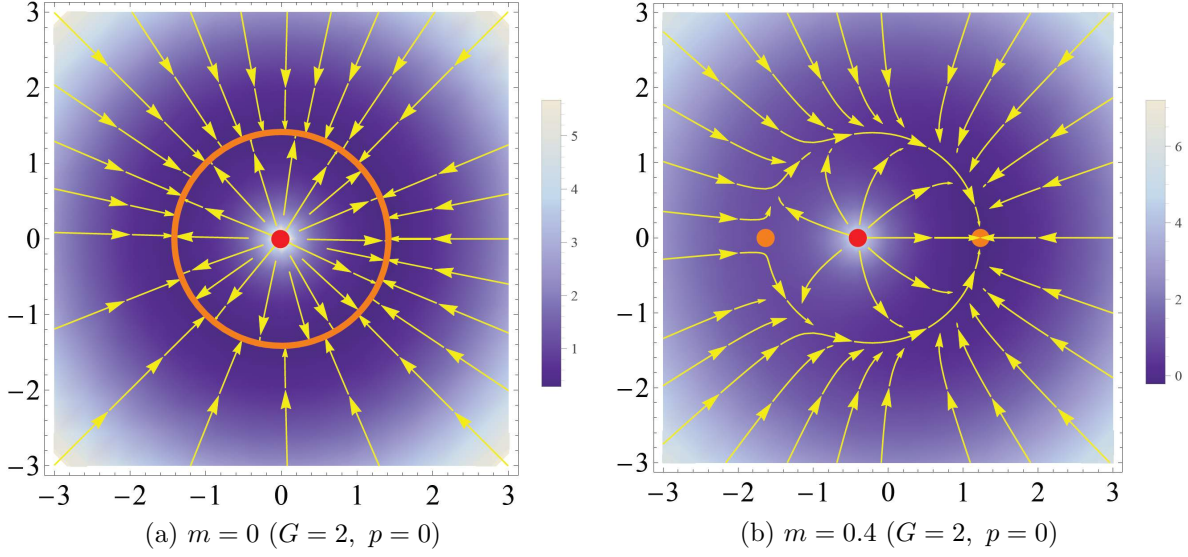


Figure 3.12: The downward flow (3.3.13) of the NJL-like model in a plane with $\text{Im } z = \text{Im } w \equiv 0$. The background color scale represents $\text{Re } S(z, w)$. The red blob at $(-m, 0)$ is a singularity of the flow. The orange circle in the left panel and the orange blobs in the right panel are saddle points. (Figures are taken from Ref. [91].)

and C_1 is no longer the set of saddle points. The associated Lefschetz thimbles are denoted by \mathcal{J}_+ and \mathcal{J}_- . Both \mathcal{J}_+ and \mathcal{J}_- contribute to (3.3.2), and \mathcal{J}_+ gives a dominant contribution at $N \gg 1$ as $\text{Re}(S(z_+, 0)) < \text{Re}(S(z_-, 0))$.

Thus, the Lefschetz thimble \mathcal{J}_1 is split as $\mathcal{J}_+ \cup \mathcal{J}_-$ by an arbitrarily small $m \neq 0$. In order to visualize the Stokes jump, we compute Lefschetz thimbles \mathcal{J}_\pm on the Stokes ray $G > 0$, and the quasi-stationary flows are important there. The flow equations at $p = 0$ read⁷

$$\frac{d\bar{z}}{d\tau} = \frac{2(z+m)}{(z+m)^2 + w^2} - \frac{2z}{G}, \quad (3.3.13a)$$

$$\frac{d\bar{w}}{d\tau} = \frac{2w}{(z+m)^2 + w^2} - \frac{2w}{G}. \quad (3.3.13b)$$

It is easy to check that the condition $\text{Im } z = \text{Im } w = 0$ is conserved along the flow. That is, if we start a flow from a point $(z, w) \in \mathbb{R}^2$, then the flow stays in \mathbb{R}^2 . In Fig. 3.12, we show a sketch of the flow for $(z, w) \in \mathbb{R}^2$ at $m = 0$ (left panel) and $m > 0$ (right panel). At $m = 0$, there is a ring of fixed points $z^2 + w^2 = G$ (orange line) that is $C_1 \cap \mathbb{R}^2$ and attracts all flows on the plane $\mathcal{J}_1 = \mathbb{R}^2 \setminus \{(0, 0)\}$.

For $m > 0$, there are only two saddle points shown with orange blobs in Fig. 3.12 (b). This figure corresponds to the left panel of Fig. 3.9. Now there is a slow but non-vanishing flow along the orbit $z^2 + w^2 \simeq G$. It is clear from the figure that $(z_+, 0)$ attracts all the flows on this plane, except for the real axis to the left of $(-m, 0)$ on which the flow is attracted to $(z_-, 0)$. Since \mathcal{J}_+ is defined as the union of all flows that sink in $(z_+, 0)$, we find that the set

$$\mathfrak{J}_A := \mathbb{R}^2 \setminus \{(x, 0) \mid x \leq -m\} \subset \mathbb{C}^2 \quad (3.3.14)$$

is contained in \mathcal{J}_+ .

⁷In this section, the definition of the fictitious time τ has an extra minus sign.

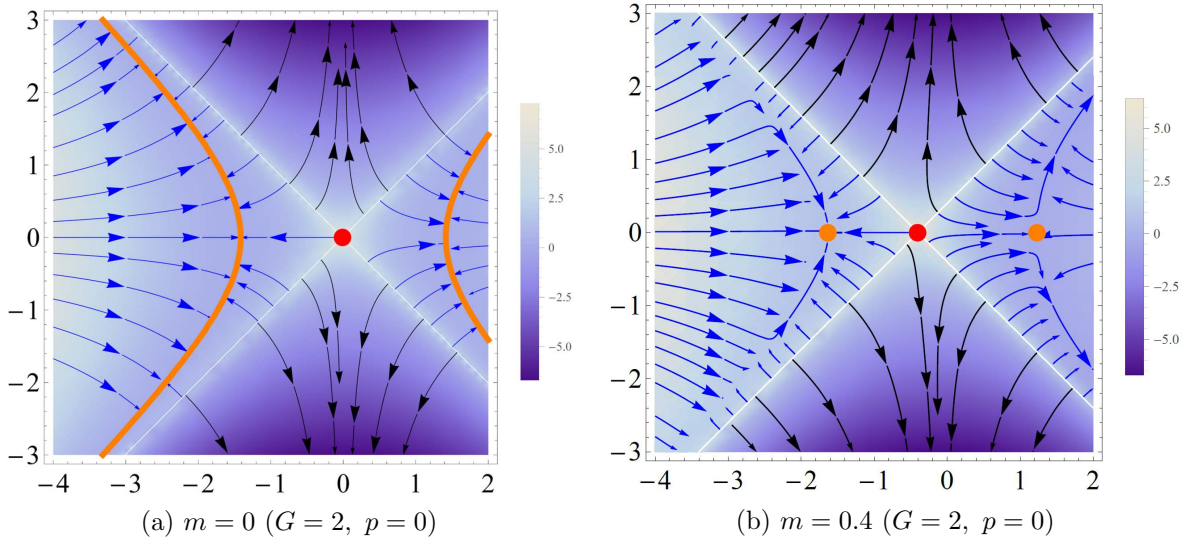


Figure 3.13: Same as Fig. 3.12 but with $\text{Im } z = \text{Re } w \equiv 0$. The X-shaped white lines are points of logarithmic singularity of the action. (Figures are taken from Ref. [91].)

Let us go back to (3.3.13), then the condition $\text{Im } z = \text{Re } w = 0$ is also conserved along the flow. Figure 3.13 shows the flow pattern in the $(\text{Re } z, \text{Im } w)$ plane with $\text{Im } z = \text{Re } w = 0$. At $m = 0$ the fixed points of the flow form a hyperbola $(\text{Re } z)^2 - (\text{Im } w)^2 = G$, which is the non-compact orbit of C_1 in Sec. 3.3.2.

At $m > 0$, a slow but non-vanishing flow appears along the hyperbola (see Fig. 3.13 (b), which corresponds to the right panel of Fig. 3.9). According to Fig. 3.13 (b), we can find that the Lefschetz thimble \mathcal{J}_- is given by the wedge-shaped region

$$\mathfrak{J}_B := \{(z, w) \in \mathbb{C}^2 \mid \text{Im } z = 0, \text{Re } w = 0, \text{Re } z + m < \text{Im } w < -\text{Re } z - m\}. \quad (3.3.15)$$

In Fig. 3.14, we combine flow plots in Figs. 3.12 (b) and 3.13 (b) at $m = 0.4$ within a three-dimensional subspace of \mathbb{C}^2 specified by $\text{Im } z = 0$, as we did in Fig. 3.10. Since $G > 0$ is on the Stokes ray, two saddle points $(z_{\pm}, 0)$ are connected via a flow and Lefschetz thimbles are ill-defined as cycles. Although the singularity of Lefschetz thimbles can be smoothed out through complexification of G as $Ge^{i\theta}$, it makes the Lefschetz thimbles extend into the whole \mathbb{C}^2 space.

Since the complexification of G impedes our visualization of the Stokes jump, we shall deduce the behavior of Lefschetz thimbles as $\theta \rightarrow 0^{\pm}$ by exploiting an indirect argument. The sum of \mathcal{J}_+ and \mathcal{J}_- is identical to the original integration cycle, \mathbb{R}^2 , since both \mathcal{J}_+ and \mathcal{J}_- contribute to $Z_{U(1)}$ with unit coefficients. Since \mathcal{J}_- gives a subdominant contribution compared with \mathcal{J}_+ , \mathcal{J}_+ changes by an integer multiple of \mathcal{J}_- at $\theta = 0^{\pm}$. These considerations indicate that we have

$$\begin{cases} \mathcal{J}_+ = \mathfrak{J}_A + \mathfrak{J}_B \\ \mathcal{J}_- = \mathfrak{J}_B \end{cases} \quad \text{at } \theta = 0^- \quad \Rightarrow \quad \begin{cases} \mathcal{J}_+ = \mathfrak{J}_A - \mathfrak{J}_B \\ \mathcal{J}_- = \mathfrak{J}_B \end{cases} \quad \text{at } \theta = 0^+. \quad (3.3.16)$$

Here, we assume an appropriate orientation of \mathfrak{J}_B . We find that the Lefschetz-thimble decomposition is given by $\mathbb{R}^2 = \mathcal{J}_+ - \mathcal{J}_-$ at $\theta = 0^-$ and by $\mathbb{R}^2 = \mathcal{J}_+ + \mathcal{J}_-$ at $\theta = 0^+$. It is important to notice that the contribution of \mathfrak{J}_B is exactly canceled between \mathcal{J}_+ and \mathcal{J}_- . This cancellation keeps the partition function real-valued and continuous in G , because the integral over \mathfrak{J}_B is purely imaginary (see below). This is one example that highlights the reason why we need sum up multiple Lefschetz thimbles in order to obtain a physically correct result.

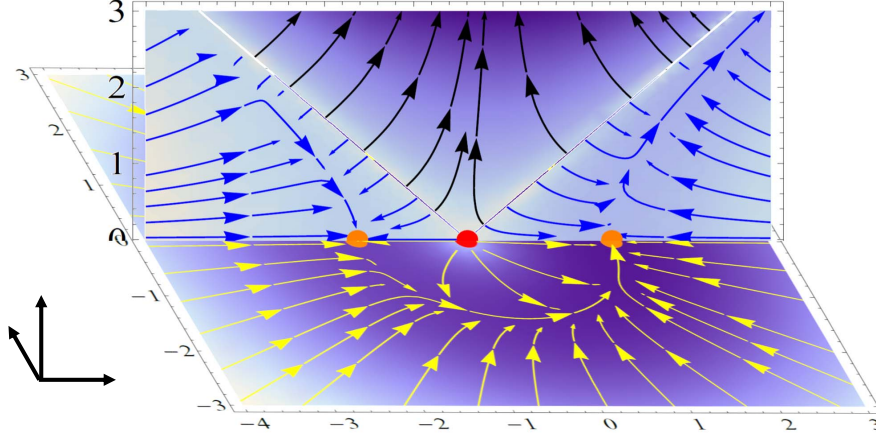


Figure 3.14: The downward flow (3.3.13) in a 3-dimensional space with $\text{Im } z \equiv 0$. The parameters are $m = 0.4$, $G = 2$ and $p = 0$ (same as for the right panels in Figs. 3.12 and 3.13). (Figures are taken from Ref. [91].)

It is intriguing to ask what happens near the chiral limit. As $m \rightarrow 0^+$, we can regard that \mathfrak{J}_A converges to $\mathcal{J}_1 = \{(z, w) \in \mathbb{R}^2 \mid (z, w) \neq (0, 0)\}$ up to a null set. However, according to (3.3.16), both \mathcal{J}_+ and \mathcal{J}_- contain an imaginary component \mathfrak{J}_B , and thus neither of them converges to \mathcal{J}_1 in the chiral limit. The same thing happens for the bosonic model discussed in Sec. 3.3.2. A unique feature of the fermionic model in comparison to bosonic models is that one of the thimbles (\mathcal{J}_-) is the wedge-shaped region because of the logarithmic singularity.

Near the chiral limit ($m \ll \sqrt{G}$), we have observed that a quasi-stationary flow along the orbit $z^2 + w^2 \simeq G$ emerges (see Figs. 3.12 and 3.13). This originates from the $O(2, \mathbb{C})$ symmetry of $S(z, w)$ at $m = 0$. Since $O(2, \mathbb{C})$ is non compact, the non-compact orbit on \mathfrak{J}_B (see Fig. 3.13) extends to infinity and it gives a divergent contribution in the limit $m \rightarrow 0$, as we discussed in Sec. 3.2.2. More explicitly, we find for the contribution from \mathfrak{J}_B

$$Z|_{\mathfrak{J}_B} = \frac{N}{\pi G} \int_{\mathfrak{J}_B} dz dw \left\{ (z + m)^2 + w^2 \right\}^N e^{-\frac{N}{G}(z^2 + w^2)} \quad (3.3.17)$$

$$= i \frac{N}{\pi G} \int_0^\infty dR R^{2N+1} \int_{-\infty}^\infty d\Phi e^{-\frac{N}{G}(m^2 + 2mR \cosh \Phi + R^2)} \quad (3.3.18)$$

$$= 2i \frac{N}{\pi G} e^{-\frac{N}{G}m^2} \int_0^\infty dR R^{2N+1} e^{-\frac{N}{G}R^2} K_0\left(\frac{2NR}{G}m\right). \quad (3.3.19)$$

In the second and third lines, we changed the integration variables as $z = -m - R \cosh \Phi$ and $w = -iR \sinh \Phi$. Roughly speaking, Φ parametrizes the hyperbola in Fig. 3.13. Using the asymptotic formula $K_0(x) = -\left(\log \frac{x}{2} + \gamma\right) I_0(x) + \mathcal{O}(x^2)$, we conclude that $Z|_{\mathfrak{J}_B}$ diverges as $\sim \log m$ in the chiral limit, $m \rightarrow 0$. Since both \mathcal{J}_+ and \mathcal{J}_- include \mathfrak{J}_B with the opposite sign (see (3.3.16)), this infrared divergence on each thimble exactly cancels out when we sum up both contributions. We suspect that this is a generic phenomenon that occurs when we handle the spontaneous breaking of continuous symmetries by the path integral on Lefschetz thimbles. It is an important check of future studies to compute the behavior of Lefschetz thimbles for field-theoretical models in higher dimensions.

3.4 Brief summary

In this chapter, we discussed the chiral symmetry breaking from the viewpoint of the Lefschetz-thimble approach. Since the spontaneous breaking of the chiral symmetry is an essential ingredient to understand low-energy dynamics of QCD, this study gives a part of the theoretical foundation to study low-temperature and finite-density QCD using Lefschetz thimbles.

In Sec. 3.1, we first study the case where the chiral symmetry is given by a discrete group \mathbb{Z}_2 using a 0-dimensional Gross–Neveu model. After introducing an auxiliary bosonic field for the chiral condensate, we apply the Lefschetz-thimble method for evaluating the bosonic integral. This is the first application of the Lefschetz-thimble method when the effective action has a contribution from the fermionic determinant. The Lefschetz-thimble decomposition of the integration cycle provides a nice setup to study the analytic structure of the partition function because we can complexify the four-fermion coupling before performing the path integral. Thanks to this property, we can discuss the phase transition of this model in the large- N limit from the viewpoint of anti-Stokes rays and Lee–Yang zeros.

In QCD, the chiral symmetry is a continuous and approximate symmetry. Indeed, pions are pseudo Nambu–Goldstone bosons of the symmetry breaking from $SU(2)_L \times SU(2)_R$ to $SU(2)_{L+R}$. In order to extend our analysis in Sec. 3.1 to spontaneous breaking of continuous symmetries, we developed a computational way of Lefschetz thimbles with approximate continuous symmetries in Sec. 3.2. If there exists an exact continuous symmetry, the set of saddle points form a critical orbit of the Lie group, and there exists a remnant of that structure even after adding a small explicit symmetry breaking. In this case, we can approximately decouple the quasi-zero mode of the gradient flow to compute Lefschetz thimbles.

By applying this technique, we study the spontaneous breaking of the axial $U(1)$ symmetry of the 0-dimensional Nambu–Jona-Lasinio model in Sec. 3.3. After overcoming technical difficulties of computing Lefschetz thimbles with continuous symmetries, we can analyze this model in the almost same way as what we have done for the Gross–Neveu model. The only difference is that picking up one Lefschetz thimble has a singularity in taking the chiral limit, and thus we must sum up Lefschetz thimbles related by the gradient flow along the quasi-zero mode.

It is an important future study to extend those analysis of 0-dimensional models to that of lattice field theories or other matrix models. When many degrees of freedom are correlated with one another in a complex manner, then the perturbative fluctuation around the saddle points becomes important. It is interesting to see whether our techniques and results in this chapter are useful under such circumstances.

Chapter 4

Lefschetz-thimble approach to the Silver Blaze problem

In this chapter, the Lefschetz-thimble path integral is applied to the sign problem of several models. In this circumstance, the mean-field approximation in a usual sense cannot be applied because the self-consistent equation has no real solution. When the classical action is complex, we need complexify integration variables in order to search relevant Lefschetz thimbles. Physical observables must have real expectation values; then how can this condition be satisfied? This question is answered in Sec. 4.1.

In Sec. 4.2, the one-site Hubbard model is studied in detail, which is a good playground to study the sign problem in the path-integral expression. This model is easily and exactly solvable, but it has the severe sign problem in the path integral, whose mathematical structure is quite similar to that of finite-density QCD at $\mu_q > m_\pi/2$. Using the Lefschetz-thimble method, we unveil the secret of the severe sign problem from various points of view.

4.1 Sign problem in the mean-field approximation

When the sign problem exists, there is no solution of the self-consistent equation of the mean-field approximation. When we try to solve it, the mean field usually takes complex values, which contradicts the real-valuedness of physical observables. This is the sign problem appearing in the mean-field approximation, and we consider its origin from the viewpoint of Lefschetz thimbles. We first show the general theorem to ensure the real-valuedness of physical observables in the Lefschetz-thimble decomposition, and applies that theorem to the complex saddle-point approximation. Using this method, the sign problem of the heavy-dense QCD is shown to be completely understood. The discussion in this section is adapted from Ref. [109].

4.1.1 Real-valuedness of the partition function and observables

Let us consider a multiple integration that gives the partition function,

$$Z = \int_{\mathbb{R}^n} d^n x \, e^{-S(x)}, \quad (4.1.1)$$

where $S(x)$ is the action functional of the real field $x = (x_1, \dots, x_n)$. Since the partition function (4.1.1) for physical systems is given by the trace of a positive operator,

$$Z = \text{tr} \left[\exp -\beta \hat{H} \right], \quad (4.1.2)$$

it must be a positive quantity; however the Boltzmann weight $\exp(-S(x))$ can be complex in general. In this section, we elucidate how the real-valuedness of the partition function holds manifestly in the Lefschetz-thimble decomposition

$$Z = \sum_{\sigma \in \Sigma} \langle \mathcal{K}_\sigma, \mathbb{R}^n \rangle \int_{\mathcal{J}_\sigma} d^n z \, e^{-S(z)}. \quad (4.1.3)$$

of (4.1.1).

One of the sufficient conditions for ensuring $Z \in \mathbb{R}$ is the existence of a reflection symmetry $L : (x_i) \mapsto (L_{ij}x_j)$, which satisfies $L_{ij} = L_{ji} \in \mathbb{R}$, $L^2 = 1$ and

$$\overline{S(x)} = S(L \cdot x). \quad (4.1.4)$$

In the case of finite-density QCD, we will see later that the charge conjugation gives this correspondence. The main purpose of this section is to derive the useful formula for the mean-field analysis and its systematic improvement while keeping Z real under Eq.(4.1.4).

Let us recall Morse's flow equation which defines Lefschetz thimbles,

$$\frac{dz_i}{dt} = \overline{\left(\frac{\partial S(z)}{\partial z_i} \right)}. \quad (4.1.5)$$

In order to show invariance of the Lefschetz-thimble decomposition under the complex conjugation, some invariance of the flow equation (4.1.5) associated with the reflection symmetry (4.1.4) is sufficient. We extend the linear map L on \mathbb{R}^n to an antilinear map on \mathbb{C}^n by [109]

$$K : (z_i) \mapsto (L_{ij} \bar{z}_j). \quad (4.1.6)$$

The flow equation (4.1.5) shows the covariance under this antilinear reflection: Using Eq.(4.1.4), we find

$$\frac{d\bar{z}_i}{dt} = \overline{\left(\frac{\partial S(L \cdot \bar{z})}{\partial \bar{z}_i} \right)}, \quad (4.1.7)$$

and thus the antilinearly transformed function $z'(t) := K(z(t))$ satisfies the same gradient flow equation (4.1.5):

$$\begin{aligned} \frac{dz'_i(t)}{dt} &= L_{ij} \cdot \overline{\left(\frac{\partial S(L \cdot \bar{z})}{\partial \bar{z}_j} \right)} = L_{ij} \cdot L_{kj} \cdot \overline{\left(\frac{\partial S(z')}{\partial z'_k} \right)} \\ &= \overline{\left(\frac{\partial S(z')}{\partial z'_i} \right)}. \end{aligned} \quad (4.1.8)$$

Many important properties can be deduced from this conclusion [109]:

1. When z^σ is a saddle point, so is $K(z^\sigma)$. Let \mathcal{J}_σ be the Lefschetz thimble around z^σ ; then $\mathcal{J}_\sigma^K := \{K(z) \mid z \in \mathcal{J}_\sigma\}$ coincides with the Lefschetz thimble around $K(z^\sigma)$ up to orientation.
2. Since the flow is covariant under the antilinear map, $\langle \mathcal{K}_\sigma, \mathbb{R}^n \rangle = \langle \mathcal{K}_\sigma^K, \mathbb{R}^n \rangle$ under an appropriate choice of the orientation. This means that the contributing thimbles always form an invariant pair $\mathcal{J}_\sigma \cup \mathcal{J}_\sigma^K$.

Let us decompose Σ into three disjoint parts. For simplicity, we assume that $S(z^\sigma) \in \mathbb{R}$ only if the saddle point satisfies $z^\sigma = K(z^\sigma)$ ¹; then, $\Sigma = \Sigma_0 \cup \Sigma_{>} \cup \Sigma_{<}$, where

$$\Sigma_0 = \{\sigma \mid z^\sigma = L \cdot \overline{z^\sigma}\}, \quad \Sigma_{\geq} = \{\sigma \mid \text{Im} S(z^\sigma) \geq 0\}. \quad (4.1.9)$$

The transformation K induces a one-to-one and onto correspondence between $\Sigma_{>}$ and $\Sigma_{<}$. Equation (4.1.3) becomes

$$Z = \sum_{\sigma \in \Sigma_0} n_\sigma \int_{\mathcal{J}_\sigma} d^n z e^{-S(z)} + \sum_{\tau \in \Sigma_{>}} n_\tau \int_{\mathcal{J}_\tau + \mathcal{J}_\tau^K} d^n z e^{-S(z)}. \quad (4.1.10)$$

Each integral on the r.h.s. of the formula (4.1.10) is real or purely imaginary depending on whether K changes orientation of $\mathcal{J}_\sigma \cup \mathcal{J}_\sigma^K$. Since the l.h.s. is real, n_τ must be zero unless the integral on $\mathcal{J}_\tau + \mathcal{J}_\tau^K$ is real². This conclusion can also be applied to expectation values of any physical observables that satisfy the symmetry (4.1.4). The decomposition formula (4.1.10) takes a suitable form for the saddle-point analysis.

Let us emphasize here that the real-valuedness of the partition function is ensured only by the invariance under the antilinear map K . The point of our discussion is that the Lefschetz-thimble decomposition of the integration cycle manifestly respects the antilinear reflection K , and so does the saddle-point analysis based on it.

4.1.2 Mean-field approximation and complex classical actions

Charge conjugation in finite-density QCD The QCD partition function at temperature $T = \beta^{-1}$ and quark chemical potential μ_q is given by

$$Z_{\text{QCD}} = \int \mathcal{D}A \det D(A, \mu_q) e^{-S_{\text{YM}}[A]}, \quad (4.1.11)$$

where $S_{\text{YM}} = \frac{1}{2} \text{tr} \int_0^\beta dx^4 \int d^3\mathbf{x} |F_{\mu\nu}|^2$ (> 0) is the Yang-Mills action, and

$$\det D(A, \mu_q) = \det [\gamma^\nu (\partial_\nu + ig A_\nu) + \gamma^4 \mu_q + m] \quad (4.1.12)$$

is the quark determinant. When $\mu_q \neq 0$, the quark determinant becomes an oscillatory functional of the gauge field A , and the sign problem emerges. Even when $\mu_q \neq 0$, the charge conjugation $A \mapsto -A^t$ with the γ_5 hermiticity implies that the fermion determinant still satisfies the identity [113, 114],

$$\begin{aligned} \overline{\det D(A, \mu_q)} &= \det D(A^\dagger, -\mu_q) \\ &= \det D(-\bar{A}, \mu_q). \end{aligned} \quad (4.1.13)$$

The charge C and complex K conjugation, or the CK transformation, serves as the antilinear map (4.1.6) for finite-density QCD [115, 116]. The Lefschetz-thimble decomposition (4.1.10)

¹This technical assumption can be removed by carefully defining Σ_{\geq} so that they are conjugate to each other under the antilinearly extended map $K(z)$ of L .

²We here assume that the coupling constant is generic so that Stokes phenomenon does not occur. If it does, several saddle points are connected via some downward flows, and subdominant saddle points may give a purely imaginary contribution so as to cancel ambiguities of the large-order perturbation series at the dominant saddle. This is discussed in the context of the resurgence trans-series of quantum field theories [35, 37, 40, 41, 75, 110–112].

manifestly respects the CK symmetry so that $Z_{\text{QCD}} \in \mathbb{R}$. Since the discussion is robust, this conclusion applies to any effective descriptions of QCD, including lattice QCD simulations [67–70, 117] and also matrix models.

We apply our insight on the Lefschetz-thimble method to the sign problem in Polyakov-loop effective models. The Polyakov loop $\ell_{\mathbf{3}}$ of the fundamental representation $\mathbf{3}$ is an order parameter for the confinement-deconfinement transition [24];

$$\ell_{\mathbf{3}} = \frac{1}{3} \text{tr} \left[\mathcal{P} \exp \left(ig \int_0^\beta A_4 dx^4 \right) \right], \quad (4.1.14)$$

where \mathcal{P} refers to the path ordering. To understand its properties, the constrained effective action $S_{\text{eff}}(a_4)$ of the Polyakov loop is useful [118, 119]. It describes the (complex) weight of the partition function under the background Polyakov-loop phase a_4 :

$$\exp(-S_{\text{eff}}(a_4)) = \int \mathcal{D}A \, e^{-S[A]} \delta(A_4 - a_4), \quad (4.1.15)$$

where A_4 is the temporal gauge field and $S[A] = S_{\text{YM}}[A] - \ln \det D(A, \mu_q)$. We implicitly take the Polyakov gauge fixing with

$$\exp\left(i \frac{ga_4}{T}\right) = \text{diag} \left[e^{i(\theta_1 + \theta_2)}, e^{i(-\theta_1 + \theta_2)}, e^{-2i\theta_2} \right]. \quad (4.1.16)$$

The Weyl group action $(\theta_1, \theta_2) \mapsto (-\theta_1, \theta_2)$, $(\theta_1, \theta_2) \mapsto ((\theta_1 + 3\theta_2)/2, (\theta_1 - \theta_2)/2)$ just permutes eigenvalues of the Polyakov loop (4.1.16), and thus the parameter region can be restricted to $\mathfrak{C} = \{\theta = (\theta_1, \theta_2) \mid 3|\theta_2| \leq \theta_1 \leq \pi\}$. This background field method, or the mean-field approximation (MFA), gives a single integration over $a_4(\theta_1, \theta_2)$ to compute the partition function:

$$Z_{\text{QCD}} = \int_{\mathfrak{C}} d\theta_1 d\theta_2 H(\theta_1, \theta_2) \exp[-S_{\text{eff}}(\theta_1, \theta_2)], \quad (4.1.17)$$

with $H(\theta) = \sin^2 \theta_1 \sin^2((\theta_1 + 3\theta_2)/2) \sin^2((\theta_1 - \theta_2)/2)$ coming from the $SU(3)$ Haar measure [120, 121]. When the quark chemical potential μ_{qk} is turned on under the nontrivial Polyakov-loop background, the effective action $S_{\text{eff}}(\theta)$ takes complex values in general due to the quark determinant. This makes the integration (4.1.17) oscillatory, and the sign problem remains in the mean-field approximation [113, 114].

Lefschetz-thimble analysis of heavy-dense Polyakov-loop models In order to evade the sign problem of the MFA, we should rewrite Eq.(4.1.17) based on the decomposition formula (4.1.10). Since $H(\theta)$ identically vanishes at the edge of \mathfrak{C} , the Lefschetz-thimble method can be applied by regarding $S(\theta) = S_{\text{eff}}(\theta) - \ln H(\theta)$. In terms of the Polyakov-loop (4.1.16), the CK transformation K becomes

$$K(z_1, z_2) = (\overline{z_1}, -\overline{z_2}), \quad (4.1.18)$$

where z_i is the complexified variable of θ_i , up to some Weyl transformations. The CK symmetry (4.1.13) leads

$$\overline{S_{\text{eff}}(z_1, z_2)} = S_{\text{eff}}(\overline{z_1}, -\overline{z_2}). \quad (4.1.19)$$

It is important to remark that the Polyakov loop,

$$\ell_{\mathbf{3}}(\theta) = \frac{1}{3} (2e^{i\theta_2} \cos \theta_1 + e^{-2i\theta_2}), \quad (4.1.20)$$

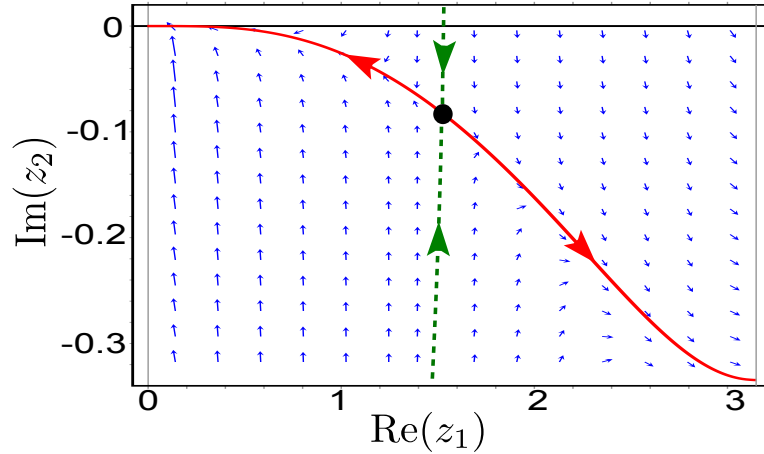


Figure 4.1: Flows at $h = 0.1$ and $\mu = 2$ around the \mathcal{CK} -symmetric saddle point (the black blob) z^* in the $\text{Re}(z_1)$ - $\text{Im}(z_2)$ plane. The red solid and green dashed lines are the Lefschetz thimble \mathcal{J}_* and its dual \mathcal{K}_* of z^* , respectively. Since \mathcal{K}_* intersects with $\text{Im}(z_2) = 0$, the integral over \mathcal{J}_* is equal to that over \mathfrak{C} . (The figure is taken from Ref. [109])

satisfies the \mathcal{CK} symmetry (4.1.19). For our demonstration, we take a simplified heavy-quark model [113, 122–127]:

$$\begin{aligned} S_{\text{eff}} &= -h \frac{(3^2 - 1)}{2} \left(e^\mu \ell_{\mathbf{3}}(\theta_1, \theta_2) + e^{-\mu} \ell_{\bar{\mathbf{3}}}(\theta_1, \theta_2) \right) \\ &= -\frac{8h}{3} \left(2 \cos \theta_1 \cos(\theta_2 - i\mu) + \cos(2\theta_2 + i\mu) \right). \end{aligned} \quad (4.1.21)$$

Since the Polyakov loop $\ell_{\mathbf{3}}$ can be regarded as a free energy for single quark excitation, this effective action represents the free energy for static quarks. Therefore, this approximation can be justified when quarks are sufficiently heavy. When $h \neq 0$ and $\mu = \beta\mu_{\text{qk}} \neq 0$, the integration (4.1.17) is oscillatory because S_{eff} takes complex values. The gluon dynamics is neglected just for simplicity.

If $h = 0$, the system has the \mathbb{Z}_3 symmetry generated by $(\theta_1, \theta_2) \mapsto (\theta_1, \theta_2 + 2\pi/3)$ up to Weyl group actions. The Haar measure factor $H(\theta_1, \theta_2)$ takes the unique maxima at $\theta^* = (2\pi/3, 0)$ in \mathfrak{C} , and this is \mathbb{Z}_3 invariant. For later purposes, it is important to notice that this saddle point is \mathcal{CK} symmetric in the sense that $\theta^* = K(\theta^*)$. The eigenvalues of the temporal Wilson line (4.1.16) become uniformly separated, and thus $\langle \ell_{\mathbf{3}} \rangle = 0$.

When $h \neq 0$, the \mathbb{Z}_3 symmetry is explicitly broken, and the saddle point z^* moves away from the \mathbb{Z}_3 -symmetric point $(2\pi/3, 0)$, but it still must be CK symmetric because there are no other saddles to form a pair. By continuity of intersection numbers, z^* will contribute to Z_{QCD} even for finite h and μ . In order to demonstrate it lucidly, we explicitly solve the flow equation (4.1.5) around the CK -symmetric saddle point (see Fig. 4.1). The dual thimble \mathcal{K}_* of z^* is shown with the green dashed curve, and it indeed intersects with the original integration cycle \mathfrak{C} . Therefore, the complex saddle point contributes, but physical quantities take real values since the CK symmetry is respected under the Lefschetz-thimble decomposition.

In the limit $\mu \rightarrow +\infty$, the saddle-point approximation becomes accurate. In this limit, the effect of the quark potential S_{eff} becomes quite large. By solving the saddle-point equation of

S in the limit $\mu \rightarrow \infty$, we find that

$$z_1^* \simeq \frac{3e^{-\mu/2}}{2\sqrt{h}}, \quad z_2^* \simeq -i\frac{e^{-\mu}}{8h}, \quad (4.1.22)$$

and it indeed approaches the perturbative vacuum $z_{\text{pert.}}^* = (0, 0)$ of S_{eff} . Thus, $\langle \ell_{\mathbf{3}} \rangle$ and $\langle \ell_{\bar{\mathbf{3}}} \rangle$ converge to 1 in this limit, as was numerically observed in Fig.2 of Ref. [113]. Using the saddle-point approximation, we can see that these Polyakov loops have different expectation values:

$$\langle \ell_{\bar{\mathbf{3}}} \rangle - \langle \ell_{\mathbf{3}} \rangle \simeq \frac{2}{3} (\sinh 2iz_2^* - 2 \cos z_1^* \sinh iz_2^*) > 0. \quad (4.1.23)$$

These results are consistent with those of exact computations of expectation values [113], and the CK -symmetric saddle point gives real expectation values [115, 116]. The formula (4.1.10) shows that this approximation can be systematically improved perturbatively to satisfy these physical requirements.

In this model, the flow equation tells us that only the single saddle point contributes to the path integral. In order to make our mean-field analysis valid, the one-thimble approximation must be sufficiently accurate and this condition can be checked by solving the flow equation in principle.

4.2 One-site Hubbard model

In this section, we apply the Lefschetz-thimble approach to the one-site model of electron systems. This toy model can be regarded as an extreme limit of strong couplings, because it can be obtained by neglecting hopping in the Hubbard model, and its Hamiltonian can be easily diagonalized. If we rewrite its partition function using the path integral with the Hubbard–Stratonovich transformation, the sign problem emerges and thus this toy model provides us a good playground to study theoretical structures of the Lefschetz-thimble approach when we apply it to the sign problem. In a previous study [117], the two-dimensional Hubbard model is studied using the Lefschetz-thimble Monte Carlo method, but one must use the so-called “one-thimble approximation” due to the current limitation of the numerical algorithm. Since our system is exactly solvable, we can understand the complete structure of Lefschetz thimbles, and suggest appropriate approximation schemes. The discussion in this section is adapted from Ref. [128].

4.2.1 Physical properties of the model

The Hubbard model [129–131] is a lattice model of many-body electron systems, and it can describe the transition between Mott insulators and metals. Its dynamics is governed by

$$\hat{H} = -t \sum_{\langle i,j \rangle, \sigma} \hat{c}_{\sigma,i}^\dagger \hat{c}_{\sigma,j} + U \sum_i \hat{n}_{\uparrow,i} \hat{n}_{\downarrow,i} - \mu \sum_i (\hat{n}_{\uparrow,i} + \hat{n}_{\downarrow,i}). \quad (4.2.1)$$

The summation is taken over all the lattice sites i , and the notation $\langle i, j \rangle$ denotes that only the nearest neighbor hopping is considered. $\hat{c}_{\sigma,i}^\dagger$ and $\hat{c}_{\sigma,i}$ are creation and annihilation operators of fermions of the spin $\sigma (= \uparrow, \downarrow)$ at the site i obeying $\{\hat{c}_{\sigma,i}, \hat{c}_{\tau,j}^\dagger\} = \delta_{\sigma\tau} \delta_{ij}$, and $\hat{n}_{\sigma,i} = \hat{c}_{\sigma,i}^\dagger \hat{c}_{\sigma,i}$ is the

number operator. The parameter t is called the hopping parameter, and we will consider the case $t = 0$ in this section. The parameter $U(> 0)$ describes the on-site repulsive interaction, and the energy increases if more than one particles get together at the same site. The Hamiltonian is invariant under the global $U(1)$ rotation $\hat{c}_{\sigma,i}^{(\dagger)} \mapsto \exp(\pm i\alpha)\hat{c}_{\sigma,i}^{(\dagger)}$, and the total number of fermions is conserved. In the Hamiltonian (4.2.1), the chemical potential μ is introduced for this conserved quantity.

At zero temperature, the Hubbard model shows a Mott insulating phase if $t \ll U$. Especially in the strong coupling limit $t = 0$, one can solve the model (4.2.1) analytically and let us see the result on the total number density $\langle \hat{n} \rangle$ as a function of the chemical potential μ . Since each site is totally independent from others, one can study the single-site Hamiltonian,

$$\hat{H} = U\hat{n}_{\uparrow}\hat{n}_{\downarrow} - \mu\hat{n}, \quad (4.2.2)$$

instead. Since the Hamiltonian (4.2.2) commutes with the number density operator $\hat{n} = \hat{n}_{\uparrow} + \hat{n}_{\downarrow}$, we can take the number basis to find the ground state. Let us define the partition function

$$Z = \text{tr} \left[\exp \left(-\beta \hat{H} \right) \right], \quad (4.2.3)$$

then the number basis gives an explicit result:

$$Z = 1 + 2e^{\beta\mu} + e^{-\beta(U-2\mu)} \quad (4.2.4)$$

The number density is given as

$$\langle \hat{n} \rangle = \frac{1}{\beta} \frac{\partial}{\partial \mu} \ln Z = \frac{2(e^{\beta\mu} + e^{-\beta(U-2\mu)})}{1 + 2e^{\beta\mu} + e^{-\beta(U-2\mu)}}, \quad (4.2.5)$$

and, in the zero-temperature limit $\beta \rightarrow \infty$, it shows a non-analytic behavior:

$$n(\beta = \infty) = \begin{cases} 0 & \text{for } \mu/U < 0, \\ 1 & \text{for } 0 < \mu/U < 1, \\ 2 & \text{for } \mu/U > 1. \end{cases} \quad (4.2.6)$$

At the half-filling $\mu = U/2$, Eq. (4.2.5) shows that $\langle \hat{n} \rangle = 1$ for any β , which comes from the particle-hole symmetry $\hat{n} \mapsto 2 - \hat{n}$ (or, $\hat{n}_{\sigma} \mapsto 1 - \hat{n}_{\sigma}$) in (4.2.2).

4.2.2 Path integral formulation and the sign problem

We have explicitly seen that the Hubbard model can be solved analytically using the number eigenstates in the strong coupling limit, or the static limit $t = 0$. However, if one changes the basis of the Hilbert space in taking trace, the sign problem emerges and the Hubbard model in the strong coupling provides us a good lesson.

Let us first derive the path integral expression of the partition function. Using two-component complex Grassmannian variables $\psi = (\psi_{\uparrow}, \psi_{\downarrow})$, the fermion coherent state is defined by

$$|\psi\rangle = \exp(-\psi\hat{c}^{\dagger})|0\rangle, \quad (4.2.7)$$

which satisfies $\hat{c}|\psi\rangle = \psi|\psi\rangle$. In the following, the summation over spin is taken without showing it explicitly. We take the convention in which all the Grassmannian variables anticommute with each other and with fermionic creation/annihilation operators. It is easy to check that

$$\langle \psi_1 | \psi_2 \rangle = e^{\psi_1^* \psi_2}, \quad \int d\psi^* d\psi |\psi\rangle e^{-\psi^* \psi} \langle \psi| = 1, \quad (4.2.8)$$

and

$$\text{tr}(O) = \int d\psi^* d\psi e^{-\psi^* \psi} \langle -\psi | O | \psi \rangle. \quad (4.2.9)$$

Let $|n_\uparrow, n_\downarrow\rangle$ be a fermionic Fock state, and the inner product with coherent states is

$$\langle 0, 0 | \psi \rangle = 1, \quad \langle 1, 0 | \psi \rangle = \psi_\uparrow, \quad \langle 0, 1 | \psi \rangle = \psi_\downarrow, \quad \langle 1, 1 | \psi \rangle = -\psi_\uparrow \psi_\downarrow. \quad (4.2.10)$$

Using these relation, one can compute the matrix element of the time-development operator in the following way:

$$\begin{aligned} e^{-\psi^* \psi} \langle \psi | e^{-\Delta\tau \hat{H}} | \psi' \rangle &= \exp - \left[\psi^* (\psi - e^{\Delta\tau \mu} \psi') + (1 - e^{-\Delta\tau U}) (\psi_\uparrow^* e^{\Delta\tau \mu} \psi'_\uparrow) (\psi_\downarrow^* e^{\Delta\tau \mu} \psi'_\downarrow) \right] \\ &\simeq \exp - \left[\psi^* (\psi - e^{\Delta\tau \mu} \psi') + \Delta\tau U (\psi_\uparrow^* e^{\Delta\tau \mu} \psi'_\uparrow) (\psi_\downarrow^* e^{\Delta\tau \mu} \psi'_\downarrow) \right]. \end{aligned} \quad (4.2.11)$$

The first equality is exact thanks to the knowledge on the number eigenstates, and we take an approximation for small $\Delta\tau$ in the last equality. In order to circumvent the quartic interaction, let us introduce an auxiliary field φ via the Hubbard–Stratonovich transformation, so that

$$1 = \sqrt{\frac{\Delta\tau}{2\pi U}} \int d\varphi \exp - \frac{\Delta\tau}{2U} (\varphi - iU(\psi_\uparrow^* e^{\Delta\tau \mu} \psi_\uparrow + \psi_\downarrow^* e^{\Delta\tau \mu} \psi_\downarrow))^2. \quad (4.2.12)$$

Inserting (4.2.12) into (4.2.11), we obtain that

$$e^{-\psi^* \psi} \langle \psi | e^{-\Delta\tau \hat{H}} | \psi' \rangle = \sqrt{\frac{\Delta\tau}{2\pi U}} \int d\varphi \exp - \left[\frac{\Delta\tau}{2U} \varphi^2 + \sum_\sigma \psi^* (\psi - e^{\Delta\tau \mu} (1 + i\Delta\tau \varphi) \psi') \right]. \quad (4.2.13)$$

In order to take the naive continuum limit of the path integral expression, we must exponentiate the auxiliary field in the fermionic bilinear term:

$$\begin{aligned} e^{\Delta\tau \mu} (1 + i\Delta\tau \varphi) &= \exp \left(\Delta\tau (\mu + i\varphi) + \frac{\Delta\tau^2}{2} \varphi^2 + O(\Delta\tau^{3/2}) \right) \\ &= \exp \left(\Delta\tau (\mu + i\varphi) + \frac{\Delta\tau^2}{2} \langle \varphi^2 \rangle_0 + O(\Delta\tau^{3/2}) \right) \\ &= \exp \left(\Delta\tau \left(\mu + \frac{U}{2} + i\varphi \right) + O(\Delta\tau^{3/2}) \right). \end{aligned} \quad (4.2.14)$$

Here, $\langle \varphi^2 \rangle_0$ means the expectation value of φ^2 with the Gaussian weight in (4.2.13), which gives $U/\Delta\tau$. We find the path integral expression of the partition function as

$$\begin{aligned} Z &= \lim_{N \rightarrow \infty} \sqrt{\frac{\beta/N}{2\pi U}} \int \prod_{k=1}^N d\varphi_k \exp \left(-\frac{\beta}{N} \sum_{k=1}^N \frac{\varphi_k^2}{2U} \right) \\ &\quad \times \int \prod_{k=1}^N d\psi_k^* d\psi_k \exp \left(-\sum_{k=1}^N \psi_{k+1}^* \left(\psi_{k+1} - e^{\frac{\beta}{N} (i\varphi_k + \mu + U/2)} \psi_k \right) \right), \end{aligned} \quad (4.2.15)$$

with the antiperiodic boundary condition $\psi_{N+1} = -\psi_1$. Equation of motion in terms of φ shows

$$\langle \hat{n} \rangle = \langle \psi_{k+1}^* e^{\frac{\beta}{N} (i\varphi_k + \mu + U/2)} \psi_k \rangle = -\frac{i}{U} \langle \varphi_k \rangle. \quad (4.2.16)$$

The expectation value of φ is nothing but that of the total number density. This formula will be used later in order to compute the number density. Since Eq. (4.2.15) is quadratic in the fermionic field ψ and ψ^* , we can perform the Grassmannian integration explicitly. The spectrum of the fermion bilinear operator is given by

$$\lambda_\ell(\varphi, \mu) = 1 - e^{(2\ell-1)\pi i/N} \exp \frac{\beta}{N^2} \sum_{k=1}^N (i\varphi_k + \mu + U/2). \quad (4.2.17)$$

and then in the continuum limit

$$\lim_{N \rightarrow \infty} \left(\prod_{\ell=1}^N \lambda_\ell \right)^2 = \left(1 + \exp \int_0^\beta d\tau (i\varphi(\tau) + \mu + U/2) \right)^2. \quad (4.2.18)$$

Since fermions have two flavors, the overall square is taken. Since the fermionic determinant contains only the Matsubara zero mode of φ , the path integral of non-zero Matsubara modes of φ gives a trivial Gaussian integration without coupling to μ . Therefore, the path integral is now reduced to an integral of zero Matsubara mode φ_{bg} , and we obtain that

$$Z = \sqrt{\frac{\beta}{2\pi U}} \int d\varphi_{\text{bg}} \left(1 + \exp \beta \left(i\varphi_{\text{bg}} + \mu + \frac{U}{2} \right) \right)^2 \exp -\frac{\beta}{2U} \varphi_{\text{bg}}^2. \quad (4.2.19)$$

This integration can be performed analytically to find (4.2.4). Instead, we apply the Lefschetz-thimble method because (4.2.19) has the sign problem, and this simple model may lead us to the deeper understanding of the problem.

Sign problem

In order to explicitly show that the path integral (4.2.19) contains the sign problem, let us compare it with the sign-quenched partition function. In order to make the sign problem less severe, we first shift the integration variable φ_{bg} to

$$\phi := \begin{cases} \varphi_{\text{bg}} - 2iU & \text{for } \mu/U > \frac{3}{2}, \\ \varphi_{\text{bg}} - i\left(\mu + \frac{U}{2}\right) & \text{for } -\frac{1}{2} < \mu/U < \frac{3}{2}, \\ \varphi_{\text{bg}} & \text{for } \mu/U < -\frac{1}{2}. \end{cases} \quad (4.2.20)$$

After shifting the integration variable, we take absolute values of the integrand, and the result is called the phase quenched partition function. For $\mu/U < -1/2$,

$$Z_{\text{pq}} = \int \frac{d\phi}{\sqrt{2\pi U/\beta}} |1 + e^{\beta(i\phi + \mu + U/2)}|^2 e^{-\beta\phi^2/2U}. \quad (4.2.21)$$

For $-1/2 < \mu/U < 3/2$,

$$Z_{\text{pq}} = \int \frac{d\phi}{\sqrt{2\pi U/\beta}} |1 + e^{i\beta\phi}|^2 e^{-\beta\phi^2/2U + \beta(\mu + U/2)^2/2U}. \quad (4.2.22)$$

The ratio Z/Z_{pq} is shown in Fig. 4.2 as a function of the chemical potential at $\beta U = 30$. For small (large) chemical potentials, $\mu/U \lesssim -1/2$ ($\mu/U \gtrsim 3/2$), the ratio Z/Z_{pq} is almost one because the dominant contribution comes from the unoccupied (occupied) state, and the sign

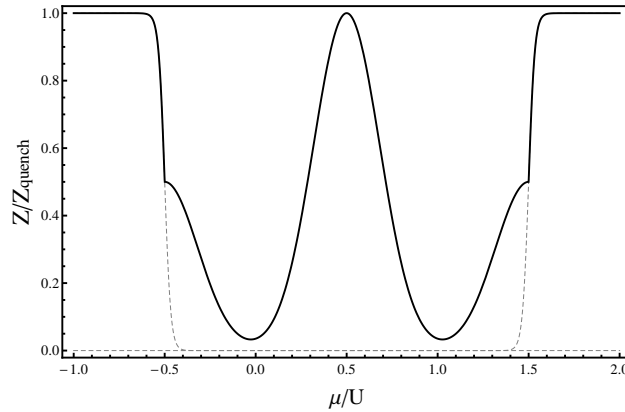


Figure 4.2: Z/Z_{pq} as a function of μ at $\beta U = 30$.

problem is sufficiently weak. In the later section, we can interpret this semiclassically because the important configurations accumulate around the origin $\varphi_{\text{bg}} \simeq 0$ ($\varphi_{\text{bg}} \simeq 2iU$). According to Fig. 4.2, there is another remarkable condition in which the sign problem disappears again by a simple shift of the integration variable: At the half-filling $\mu = U/2$, the shift of the integration variable solves the sign problem. By introducing a new integration variable by $\varphi_{\text{bg}} = \varphi'_{\text{bg}} + iU$, we find that

$$Z_{\text{half-filling}} = \sqrt{\frac{\beta}{2\pi U}} \int d\varphi'_{\text{bg}} \left(2 \cos \frac{\beta \varphi'_{\text{bg}}}{2} \right)^2 \exp \left[-\frac{\beta}{2U} (\varphi'_{\text{bg}}{}^2 - U^2) \right], \quad (4.2.23)$$

and the integrand is positive definite. The sign problem can be evaded in these three special case even using the path integral formalism, but this does not happen in general. Indeed, when $\mu/U = 0$ or 1 at which number densities (4.2.6) jumps, the sign problem is severe because

$$Z/Z_{\text{pq}} \simeq \frac{3}{2} e^{-\beta U/8} \ll 1. \quad (4.2.24)$$

We explore the origin of this sign problem in the path integral formalism by applying the Picard–Lefschetz theory to the integration (4.2.19). If we naively use (4.2.21) instead of (4.2.22) for the whole region, the sign problem becomes more severe so that $Z/Z_{\text{pq}} \propto e^{-\beta U}$ for $\mu = 0$.

When the sign problem becomes severe $\mu/U = -0.5$, the second-order phase transition happens in the phase quenched theory at $T = 0$. This situation is quite similar to what happens in the finite-density QCD at $\mu_q = m_\pi/2$.

4.2.3 Lefschetz-thimble analysis at strong couplings

Let us apply the Picard–Lefschetz theory to (4.2.19). The effective action of this system is obtained as

$$S(z) = \frac{\beta}{2U} z^2 - 2 \ln \left(1 + \exp \beta \left(iz + \mu + \frac{U}{2} \right) \right), \quad (4.2.25)$$

which satisfies the real-valued condition of the partition function (4.1.4); $\overline{S(z)} = S(-\bar{z})$. As we have shown in Sec. 4.1, this gives a strong constraint on the configuration of Lefschetz thimbles to ensure the real-valuedness of physical observables in the decomposition (4.1.10). The logarithmic function has branch singularities at fermionic Matsubara modes $z = i(\mu +$

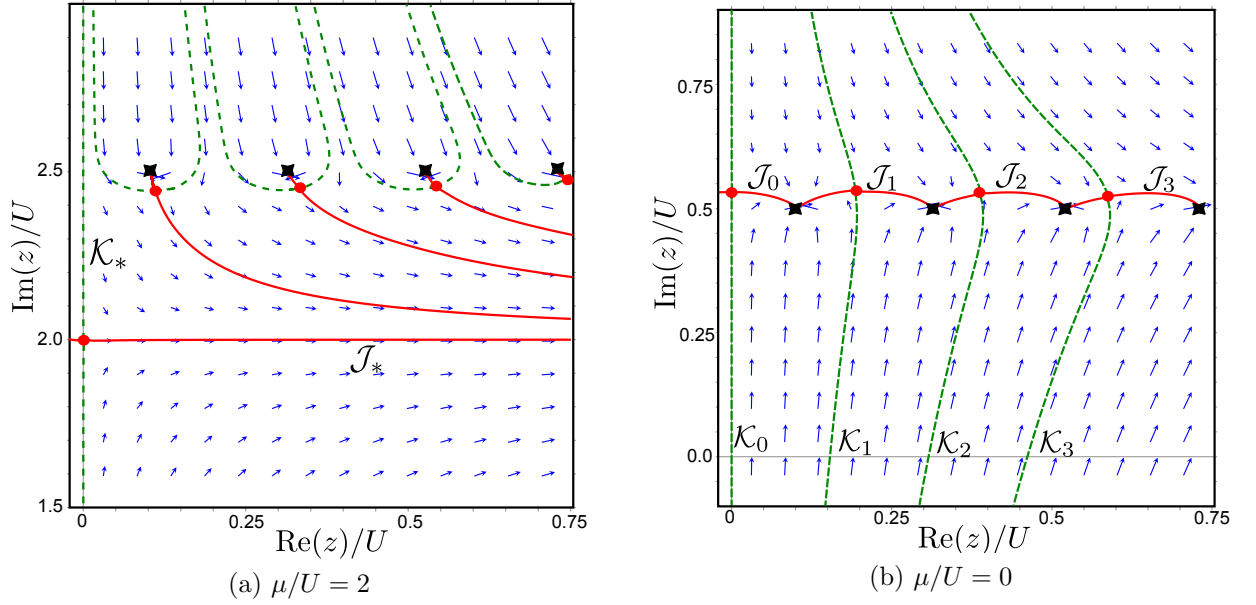


Figure 4.3: Behaviors of Morse's downward flow equation at $\beta U = 30$, for $\mu/U = 2$ (a) or $\mu/U = 0$ (b). Star-shape black points show singular points of logarithm, and red blobs show complex saddle points z_σ . We only show the region $\text{Re}(z) \geq 0$ because of the symmetry of the flow equation under $z \mapsto -\bar{z}$. (Figures are taken from Ref. [128].)

$U/2) + (2\ell + 1)\pi/\beta$ for $\ell \in \mathbb{Z}$. The integrand converges to 0, i.e., $S \rightarrow +\infty$, at these points. The flow equation of Eq. (4.2.25) reads

$$\frac{dz}{dt} = \frac{\bar{z}}{U} + \frac{2i \exp \beta (-i\bar{z} + \mu + \frac{U}{2})}{1 + \exp \beta (-i\bar{z} + \mu + \frac{U}{2})}. \quad (4.2.26)$$

Semiclassical analysis and gradient flows Let us find the set of saddle points, which is an important step not only for the saddle-point approximation but also for the Lefschetz-thimble method. The saddle-point condition of the effective action (4.2.25) is

$$iz_\sigma = -\frac{2U}{1 + \exp -\beta (iz_\sigma + \mu + \frac{U}{2})}. \quad (4.2.27)$$

In order to simplify our analysis, we consider a limiting case where $T \ll U, |\mu|$. We can approximately obtain the saddle points as

$$z_m = i \left(\mu + \frac{U}{2} \right) + T \left(2\pi m + i \ln \frac{\frac{3}{2}U - \mu}{\frac{U}{2} + \mu} \right) + O(T^2) \quad (4.2.28)$$

for $m \in \mathbb{Z}$ by assuming that the second term is much smaller than the first one. The real-valued condition says that z_{-m} and z_m form a pair. If $\mu > 3U/2$ or $\mu < -U/2$, there is another solution

$$z_* = \begin{cases} 2iU + o(T) & \text{for } \mu > \frac{3}{2}U, \\ 0 + o(T) & \text{for } \mu < -\frac{1}{2}U. \end{cases} \quad (4.2.29)$$

Behaviors of the downward flow equation (4.2.26) are shown in Fig. 4.3 with $U = 1$ and $\beta U = 30$. Let us discuss the case when the chemical potential is sufficiently large ($\mu = 2U$).

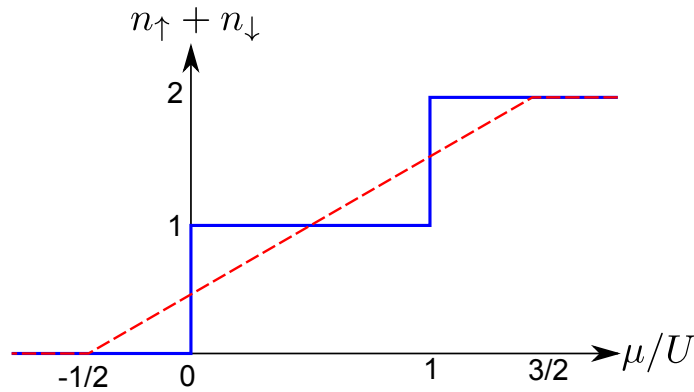


Figure 4.4: Schematic behavior of the number density. The exact result at $\beta = \infty$ is shown with the solid blue curve. The dashed red line shows the naive expectation from the positions of the complex saddle points, $\text{Im}(z_m) \simeq \mu + U/2$, for $-1/2 < \mu/U < 3/2$.

In this case, Morse's flow is shown in Fig. 4.3 (a). Only one Lefschetz thimble \mathcal{J}_* associated with z_* contributes in the Lefschetz-thimble decomposition. Other dual thimbles shown with green dashed lines do not intersect with the original integration cycle \mathbb{R} as in Fig. 4.3 (a). Thus intersection numbers in Eq. (4.1.3) vanish and we have

$$Z = \int_{\mathcal{J}_*} dz \exp -S(z). \quad (4.2.30)$$

Within the saddle-point approximation using the complex saddle point z_* , the number density is given as

$$n \simeq \frac{-iz_*}{U} = 2, \quad (4.2.31)$$

and thus the saturation of fermions is well described. The exactly similar thing happens also for $\mu/U \lesssim -1$, and then the saddle-point approximation gives $n \simeq -iz_*/U = 0$. This analysis explicitly shows why the sign problem is significantly weakened with an appropriate shift of integration variables for $\mu/U \lesssim -1$ and $\mu/U \gtrsim 2$, as we have show in Fig. 4.2.

In the following, let us concentrate on the case where the sign problem is severe, $-1/2 \lesssim \mu/U \lesssim 3/2$, at low temperatures $\beta U \gtrsim 10$. In this parameter region, the typical behavior of the flow is shown in Fig. 4.3 (b). All dual thimbles \mathcal{K}_m intersect with the original integration cycle \mathbb{R} . This shows that all the saddle points z_m contribute to the partition function³, so that the interference among them may not be negligible. This interference requires a careful treatment of the semiclassical analysis in order to solve the sign problem. Behaviors of the flow equation in Figs. 4.3 (a) and (b) are very different. This big difference can be explained by the Stokes phenomena [64], which occur around $\mu/U \simeq 3/2$ and also around $\mu/U \simeq -1/2$. However, this is irrelevant to the non-analytic behaviors of the number density, and then we stick to the analysis for $-1/2 \lesssim \mu/U \lesssim 3/2$.

There is a big question on the behavior of the number density for $-1/2 \lesssim \mu/U \lesssim 3/2$. Since the number density is given by $n = \text{Im}\langle z \rangle/U$, we may naively expect that the number density

³This statement can be shown at half-filling due to the particle-hole symmetry, but in general cases we have checked it numerically only for $|m| \lesssim \beta U/2\pi$. For sufficiently large $|m| (\gg \beta U/2\pi)$, the Stokes phenomena may happen and it may cause a peculiar behavior. However, the effect of that subtlety is quite small, and it does not change the result of the following argument.

is

$$\frac{1}{U} \text{Im}(z_m) \simeq \frac{\mu}{U} + \frac{1}{2}, \quad (4.2.32)$$

by using (4.2.28). This is shown with the dashed red line in Fig. 4.4, which is totally different from the exact result (the solid blue curve). This behavior is, however, also expected from the phase quenched theory Z_{pq} in (4.2.22). The similar problem happens in the finite-density QCD at $\mu_q = m_\pi/2$ (see Sec. 1.2), and thus this model is a prototype of the sign problem appearing in the finite-density QCD. This is the Silver Blaze problem in the one-site Hubbard model⁴. This aspect will be discussed in detail in Sec. 4.3.

Semiclassical partition function Let us denote the classical action at the saddle point z_σ as $S_\sigma(=S(z_\sigma))$. Substituting the approximate expression (4.2.28) into Eq. (4.2.25), we have

$$\text{Re}(S_m - S_0) \simeq \frac{2\pi^2}{\beta U} m^2, \quad (4.2.33)$$

$$\text{Im} S_m \simeq 2\pi m \left(\frac{\mu}{U} + \frac{1}{2} \right), \quad (4.2.34)$$

and

$$S_0 \simeq -\frac{\beta}{2U} \left(\mu + \frac{U}{2} \right)^2. \quad (4.2.35)$$

Equation (4.2.33) shows that subdominant thimbles \mathcal{J}_m can be comparable with the dominant one \mathcal{J}_0 for $\beta U \gg 1$ so long as $|m|(\neq 0)$ is not so large. According to Eq. (4.2.34), these different thimbles have different complex phases, and thus a contribution from one Lefschetz thimble is in general canceled by other ones. Exactly at the half-filling, $\mu/U = 1/2$, the complex phase is always an integer multiple of $2\pi i$, and such a cancellation is absent. This gives an interpretation on the reason why the sign problem disappears at the half-filling from the viewpoint of Lefschetz-thimble approach.

Let us compute the partition function Z_{cl} only using these semiclassical information. Neglecting the higher order correction in the Gaussian fluctuation, let us simply compute

$$Z_{\text{cl}} := \sum_{n=-\infty}^{\infty} \exp -S_n. \quad (4.2.36)$$

This can be computed analytically in the following way using the elliptic theta function:

$$\begin{aligned} Z_{\text{cl}} &\simeq e^{-S_0} \left(1 + 2 \sum_{n=1}^{\infty} \cos 2n\pi \left(\frac{\mu}{U} + \frac{1}{2} \right) e^{-2\pi^2 n^2 / \beta U} \right) \\ &= e^{-S_0} \theta_3 \left(\pi \left(\frac{\mu}{U} + \frac{1}{2} \right), e^{-2\pi^2 / \beta U} \right) \end{aligned} \quad (4.2.37)$$

⁴Recently, the one-site massive Thirring model is studied in Refs. [132–134] using the Monte Carlo simulation with one-thimble approximation. The one-thimble approximation reproduces the naive expectation, which does not explain the Silver Blaze problem correctly.

Here we used an approximate expression of the saddle points (4.2.33-4.2.35) to obtain (4.2.37)⁵. Using this result, in the limit $\beta \rightarrow \infty$, one can analytically show that

$$n_{\text{cl}} := \frac{1}{\beta} \frac{\partial}{\partial \mu} \ln Z_{\text{cl}} \rightarrow \begin{cases} 2 & (1 < \mu/U < 1.5), \\ 1 & (0 < \mu/U < 1), \\ 0 & (-0.5 < \mu/U < 0). \end{cases} \quad (4.2.38)$$

Of course, this good agreement is accidental to some extent, since we have neglected higher order contributions in the semiclassical analysis. This result, however, still indicates the usefulness of the semiclassical approximation even when the sign problem is quite severe.

Lee–Yang zeros and fermion spectrum Let us discuss this non-analytic behavior from the viewpoint of Lee–Yang zeros [97, 98, 100–107] in this semiclassical expression (4.2.37) (For Lee–Yang zeros see Sec. 3.1.3). Using the infinite-product expression of the elliptic theta function,

$$\theta_3(z, q) = \prod_{\ell=1}^{\infty} \left\{ (1 - q^{2\ell}) (1 + 2q^{2\ell-1} \cos(2z) + q^{4\ell-2}) \right\}, \quad (4.2.39)$$

the zeros of the partition function in the complex μ plane satisfy

$$\cos \left(2\pi \frac{\mu}{U} \right) = \cosh \left(\frac{2\pi^2}{\beta U} (2\ell - 1) \right) \quad (4.2.40)$$

for some positive integer ℓ . Since (4.2.37) is originally derived as an approximate expression for $-1/2 < \mu/U < 3/2$, we restrict the real part of the complex chemical potential to $-U/2 < \text{Re}\mu < 3U/2$. Then, the zeros of the partition function are

$$\mu = i\pi T(2k - 1), \quad \mu = U + i\pi T(2k - 1), \quad (4.2.41)$$

for $k \in \mathbb{Z}$. In the limit $T \rightarrow 0$, these zeros form straight lines crossing to the real axis at $\mu = 0, U$, which causes the first-order phase transition as shown in (4.2.38).

Let us apply the same analysis to the quenched partition function. Let us again define the phase quenched semiclassical partition function by

$$Z_{\text{pq,cl}} := \sum_{n=-\infty}^{\infty} \left| \exp -S_n \right|. \quad (4.2.42)$$

In the phase quenched approximation, interference of complex phases $\exp i\text{Im}S_m$ disappears, and the chemical potential dependence on μ is given by $\exp -S_0$. This is consistent with (4.2.22). Lee–Yang zeros does not exists if $-U/2 \ll \text{Re}\mu \ll 3U/2$. Therefore, the only possibility of the phase transition in this phase quenched approximation originates from the Stokes phenomena around $\mu/U \simeq -1/2, 3/2$, which usually gives the second-order transition [91].

In order to investigate this failure of the phase quench approximation more deeply, we analyze the fermion spectrum (4.2.17) at complex saddle points. For simplicity, let us take the continuum limit at first with an appropriate renormalization,

$$\lambda_{\ell}^{\text{ren}}(\varphi, \mu) := \lim_{N \rightarrow \infty} TN \lambda_{\ell}(\varphi, \mu) = - \left\{ (2\ell - 1)\pi iT + i\varphi + \mu + \frac{U}{2} \right\}. \quad (4.2.43)$$

⁵The Gaussian integral gives an m -independent prefactor $(1 + \beta U (\mu/U - 3/2) (\mu/U + 1/2))^{-1/2}$ at the leading order. It does not change a qualitative behavior and thus it is neglected in the following.

The spectral representation of the number density is given by

$$n(\varphi, \mu) = -2T \sum_{\ell=-\infty}^{\infty} \frac{e^{i0^+\ell}}{\lambda_{\ell}^{\text{ren}}(\varphi, \mu)} = \frac{2}{e^{-\beta(i\varphi + \mu + U/2)} + 1}. \quad (4.2.44)$$

If the sign problem is mild enough, $\mu < -U/2$, then the eigenvalue at the saddle point $z_* = 0$ is

$$\lambda_{\ell}^{\text{ren}}(z_*, \mu) \simeq - \left((2\ell - 1)\pi iT + \mu + \frac{U}{2} \right). \quad (4.2.45)$$

Since $\text{Re}\lambda_{\ell}^{\text{ren}}(z_*, \mu)$ cannot be zero, the chemical potential dependence of the number density is exponentially suppressed as $T \rightarrow 0$,

$$n(z_*, \mu) \simeq \frac{2}{e^{-\beta(\mu + U/2)} + 1} \simeq 0. \quad (4.2.46)$$

However, for $\mu > -U/2$, $\text{Re}\lambda_{\ell}$ can be zero in the vicinity of saddle points, and indeed one finds

$$\lambda_{\ell}^{\text{ren}}(z_m, \mu) = - \left((2(\ell + m) - 1)\pi iT - T \ln \frac{\frac{3}{2}U - \mu}{\frac{U}{2} + \mu} \right). \quad (4.2.47)$$

Within this approximation, the number density becomes

$$n(z_m, \mu) \simeq \frac{2}{e^{-\beta(i z_m + \mu + U/2)} + 1} \simeq \frac{\mu}{U} + \frac{1}{2}. \quad (4.2.48)$$

The near-zero fermionic mode provokes the fake second-order transition at $\mu = -U/2$ again, as shown with the dashed red line in Fig. 4.4. From the viewpoint of fermion spectrum at complex saddle points, nothing special happens in the vicinity of the correct transition points $\mu = 0, U$. In the language of Lefschetz thimbles, this implies that their topological structure does not change at all around $\mu = 0, U$, as we can see in Fig. 4.3 (b).

4.2.4 Importance of interference

Numerical results Let us consider one-, three-, and five-thimble approximations in order to analyze the importance of the interference among multiple Lefschetz thimbles. We consider the case where the sign problem is severe, i.e., $-1/2 \lesssim \mu/U \lesssim 3/2$ and $\beta U \gtrsim 10$. The $(2m+1)$ -thimble approximation takes into account only $\mathcal{J}_0, \mathcal{J}_{\pm 1}, \dots, \mathcal{J}_{\pm m}$ in Fig. 4.3 (b). The partition function (4.2.19) in this approximation reads

$$Z \simeq Z^{(m)} := \int_{\mathcal{J}_0} dz e^{-S(z)} + \sum_{k=1}^m 2\text{Re} \int_{\mathcal{J}_k} dz e^{-S(z)}. \quad (4.2.49)$$

Each contribution of the summation in the second term comes from a pair \mathcal{J}_k and \mathcal{J}_{-k} , and becomes manifestly real because of the reflection symmetry $z \mapsto -\bar{z}$ (see Sec. 4.1 and Ref. [109]). Since the Lefschetz thimble \mathcal{J}_k is homologically equivalent to the interval in the complex plane $i(\mu + U/2) + [(2k-1)\pi T, (2k+1)\pi T]$, the above integration (4.2.49) is reduced to

$$Z^{(m)} = \int_{-(2m+1)\pi T}^{+(2m+1)\pi T} dx \exp -S\left(x + i(\mu + U/2)\right), \quad (4.2.50)$$

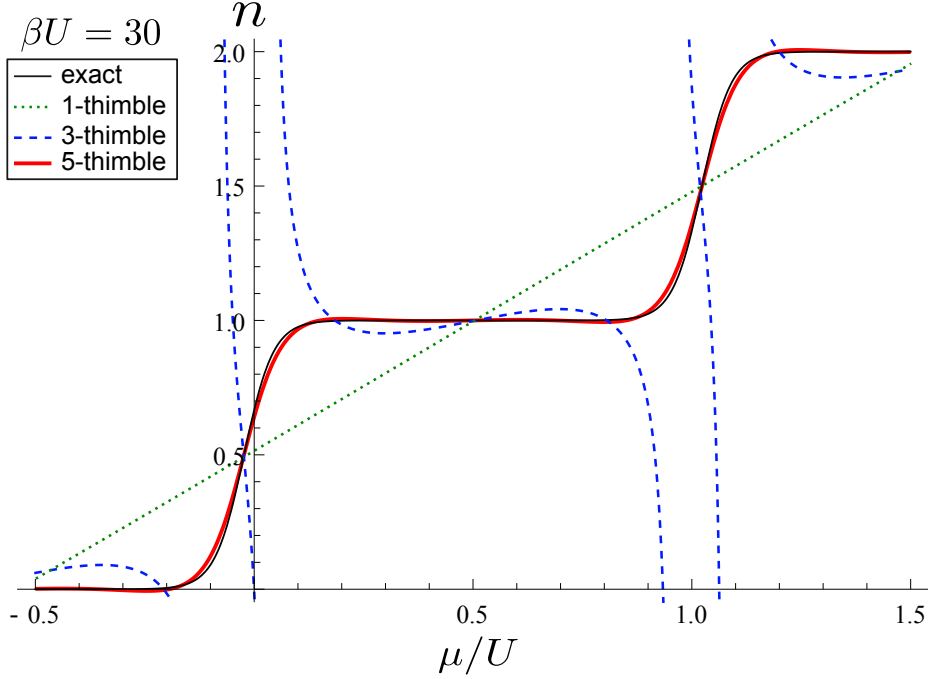


Figure 4.5: Behaviors of the number density $n = -i\langle\varphi\rangle/U$ as a function of μ at $\beta U = 30$. The thin solid black line shows the exact solution. Other lines, dotted green one, dashed blue one, and thick solid red one, show the result of one-, three-, and five-thimble approximations, which integrate over \mathcal{J}_0 , $\mathcal{J}_0 \cup \mathcal{J}_{\pm 1}$, and $\mathcal{J}_0 \cup \mathcal{J}_{\pm 1} \cup \mathcal{J}_{\pm 2}$, respectively. The five-thimble approximation gives an almost exact result, and most parts of the solid red line overlaps with the solid black one. (This figure is adapted from Ref. [128].)

with $x = z - i(\mu + U/2)$. The result on the number density at $\beta U = 30$ is shown in Fig. 4.5, in which one-, three-, and five-thimble approximations are compared with the exact computation.

The one-thimble approximation, which is shown with the dashed green line, is an approximation to integrate only over the Lefschetz thimble \mathcal{J}_0 , and it almost gives the mean-field result,

$$n_{\text{MF}} = \frac{\mu}{U} + \frac{1}{2}, \quad (4.2.51)$$

for $-1/2 < \mu/U < 3/2$. Figure 4.5 shows that the one-thimble approximation is not sufficient to describe the plateaus of the number density in the region $-1/2 < \mu/U < 3/2$. One can easily check that this is also obtained from the sign-quench approximation (4.2.22).

The result of the three-thimble approximation provides us a useful lesson for an application of the Lefschetz-thimble approach to the sign problem. The number density diverges at several chemical potentials around a rapid crossover, although the result is improved around each plateau. Let us analyze this divergence by using the semiclassical analysis. For that purpose, we introduce the semiclassical partition function with the $(2m+1)$ -thimble approximation by

$$Z_{\text{cl}}^{(m)} := \sum_{k=-m}^m \exp -S_k. \quad (4.2.52)$$

In the three-thimble approximation, the semiclassical partition function approximately behaves as

$$Z_{\text{cl}}^{(1)} \simeq e^{-S_0} \left[1 + 2e^{-\frac{2\pi^2}{\beta U}} \cos \pi \left(1 + \frac{2\mu}{U} \right) \right]. \quad (4.2.53)$$

Since $\beta U \gg 1$ and thus $e^{-2\pi^2/\beta U} \sim 1$, the second term is not suppressed, compared with the first term. This approximate partition function vanishes at some chemical potentials around $\mu/U = 0$ and 1 ($Z_{\text{cl}}^{(3)}$ vanishes at $\mu/U \simeq \pm 0.04$, which is roughly consistent with Fig. 4.5). This example clearly demonstrates that picking up a part of the Lefschetz-thimble decomposition can violate the physical requirement, such as the positivity condition on the thermodynamic quantities. In this instance, the incompressibility $(\partial n/\partial \mu)/n^2$ should not be negative.

According to Fig. 4.5, we can conclude that five Lefschetz thimbles $\mathcal{J}_0 \cup \mathcal{J}_{\pm 1} \cup \mathcal{J}_{\pm 2}$ are necessary in order to explain rapid jumps of the number density in terms of the chemical potential at a low temperature $\beta U = 30$. Indeed, the five-thimble approximation (solid red line) and the exact computation (solid black line) almost overlap with one another in Fig. 4.5.

Necessary numbers of Lefschetz thimbles How many Lefschetz thimbles are necessary in general at a given lower temperature β ? Let us propose the criterion to neglect the Lefschetz thimbles \mathcal{J}_m for large $|m|$:

$$\left| \frac{Z_{\text{cl}}^{(m)} - Z_{\text{cl}}^{(m-1)}}{Z_{\text{cl}}^{(m)}} \right| \ll 1. \quad (4.2.54)$$

Assuming that the number of Lefschetz thimbles, $(2m+1)$, is sufficiently large, one can replace $Z_{\text{cl}}^{(m)}$ in the denominator by the semiclassical partition function Z_{cl} . Since $|Z_{\text{cl}}^{(m)} - Z_{\text{cl}}^{(m-1)}| \leq 2|\exp -S_m|$, the contribution from \mathcal{J}_m can be negligible if

$$\frac{2|\exp -S_m|}{Z_{\text{cl}}} \lesssim \varepsilon. \quad (4.2.55)$$

Here ε is a controlling parameter of an error, and $\varepsilon \ll 1$. Using the approximate results (4.2.33) and (4.2.37), we can solve this inequality with respect to m :

$$|m| \gtrsim \sqrt{-\frac{\beta U}{2\pi^2} \ln \frac{\varepsilon}{2} \theta_3(\pi(\mu/U + 1/2), e^{-2\pi^2/\beta U})}. \quad (4.2.56)$$

This criterion gives different results depending on μ , and thus let us first derive the strongest restriction. If the sign problem is severe, i.e. $\mu = 0$, the elliptic theta function is exponentially small with respect to βU :

$$\theta_3\left(\frac{\pi}{2}, e^{-2\pi^2/\beta U}\right) \simeq \sqrt{\frac{2\beta U}{\pi}} e^{-\beta U/8}. \quad (4.2.57)$$

Therefore, for reasonable ε such as $\varepsilon \simeq 0.1$, the effect of ε is negligible because of its mild logarithmic dependence. The criterion gives

$$|m| \gtrsim \frac{\beta U}{4\pi} \quad (4.2.58)$$

in the limit of $\beta U \gg 1$. It means that we need $(2\lceil \beta U/4\pi \rceil + 1)$ thimbles in order to describe the rapid crossover of the number density for the one-site Hubbard model.

Let us discuss this behavior from alternative point of view. Since βU becomes large, the relevant integration region becomes smaller as $|\text{Re } z| \lesssim \sqrt{U/\beta}$. However, Fig. 4.3 shows that the length of each Lefschetz thimble \mathcal{J}_k is proportional to $1/\beta$, and thus we need more Lefschetz thimbles in order to cover the relevant integration region. That number is clearly proportional

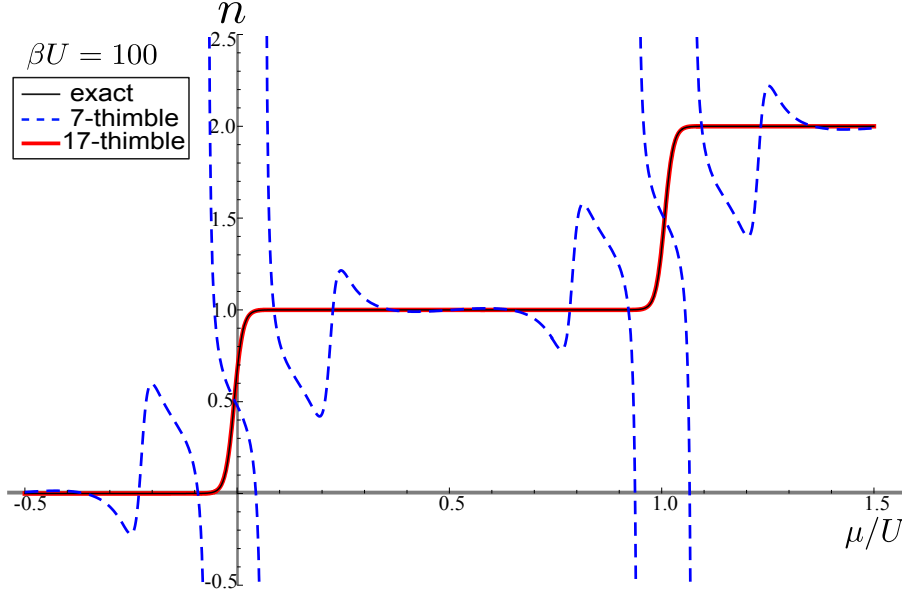


Figure 4.6: Behaviors of the number density $n = -i\langle\varphi\rangle/U$ as a function of μ at $\beta U = 100$. In order to explain the Silver Blaze phenomenon, the 7-thimble approximation is already reasonable. In order to describe the correct transition behavior, 17 Lefschetz thimbles become necessary. (This figure is adapted from Ref. [128].)

to $\sqrt{\beta U}$, and is much smaller than Eq. (4.2.58). This is because interference of complex phases among different saddle points makes the semiclassical partition function much smaller than that of the naive expectation if $\mu/U \sim 0$ and 1. This indicates that the explanation of the plateau in the vicinity of the half-filling is much easier than that of the rapid crossover. The necessary number of Lefschetz thimbles for each phenomenon is also largely different. Indeed, for $\mu/U = 1/2$, one can show that

$$\frac{Z_{\text{cl}}}{e^{-S_0}} \simeq \theta_3\left(\pi, e^{-2\pi^2/\beta U}\right) \simeq \sqrt{\frac{\beta U}{2\pi}}, \quad (4.2.59)$$

and, roughly speaking, we need

$$|m| \gtrsim \sqrt{\frac{\beta U}{2\pi^2} \ln \frac{\sqrt{8\pi}}{\varepsilon \sqrt{\beta U}}} \quad (4.2.60)$$

for \mathcal{J}_m being negligible in order to achieve a good accuracy only around the half filling. This is consistent with the result of the above heuristic argument. Now, we can understand that the large gap of these two estimates (4.2.58) and (4.2.60) comes from the sign problem in summing up Lefschetz thimbles, and the semiclassical analysis provides a reasonable rough indication. In Fig. 4.6, we plot the number density at $\beta U = 100$, and the exact result is compared with those of 7- and 17-thimble approximations. The result of the 17-thimble approximation (thick solid red line) completely overlaps with the exact one (thin solid black line). The 7-thimble approximation (dashed blue line) is insufficient to describe the phase transition at $\mu/U \sim 0$ and 1, but it nicely describes the silence of the number density in the vicinity of $\mu/U \sim -1/2$, $1/2$, and $3/2$.

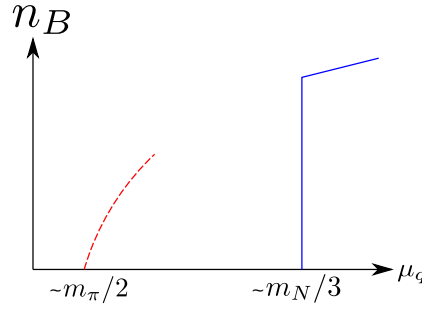


Figure 4.7: Schematic illustration of the Silver Blaze phenomenon in finite-density QCD. This plots the baryon number density n_B as a function of the quark chemical potential μ_q . In the phase quenched QCD, the second-order phase transition happens at $\mu_q \simeq m_\pi/2$ (the dashed red line), but the full QCD must experience nothing until the nuclear liquid-vapor phase transition at $\mu_q \simeq m_N/3$ (the solid blue line). It is similar to Fig. 4.4 for the one-site Hubbard model.

4.3 Speculation on the Silver Blaze problem at finite-density QCD

We have studied the one-site Hubbard model in Sec. 4.2 as a toy model of the sign problem. We elucidate that the interference of complex phases among multiple saddle points is important to explain $n = 0$ for $-U/2 < \mu < 0$ and the rapid jump of n at $\mu = 0$. In this section, we first discuss the similarity of the mathematical structure of the one-site Hubbard model to that of finite-density QCD, and mention the speculation on the baryon Silver Blaze problem. The discussion in this section is adapted from Ref. [128].

Let us recall the baryon Silver Blaze problem. We consider properties of finite-density QCD at $T = 0$. In general, the quark determinant, $\text{Det} [\gamma_4(\not{D}_A + m) - \mu_q]$, will have the (nontrivial) μ_q -dependence. Naively thinking, this means that the baryon number density n_B arises for any chemical potentials. However, since we know that the lightest baryon in the QCD spectrum is nucleon, the baryon number density n_B must be zero for any $3\mu_q < m_N - B \simeq 923 \text{ MeV}$ at $T = 0$. It is difficult to explain this empirically trivial fact by using the path-integral expression of finite-density QCD. It contains the essence of the sign problem, and this is called the baryon Silver Blaze problem [58]. Indeed, the unphysical early onset of n_B has been observed in the reweighting method of lattice QCD [135, 136] (Fig. 4.7 schematically illustrates this situation).

So far, we have understood the baryon Silver Blaze problem only for small quark chemical potentials $\mu_q < m_\pi/2$ [58, 106, 137]. In general, the eigenvalues of $\gamma_4(\not{D}_A + m)$ can be expressed as

$$\lambda_{(j,n)}(A, \mu_q) = \varepsilon_j(A) - \mu_q - i\phi_j(A) + i(2n+1)\pi T \quad (4.3.1)$$

with $-\pi T < \phi_j \leq \pi T$, and they do not depend on μ_q . Using this expression, the quark determinant becomes

$$\begin{aligned} & \text{Det} [\gamma_4(\not{D}_A + m) - \mu_q] \\ &= \mathcal{N} e^{-\beta\mu_q \text{Tr}(1)/2} \prod_j (1 + e^{-\beta(\varepsilon_j - \mu_q)} e^{i\beta\phi_j}), \end{aligned} \quad (4.3.2)$$

$$= \mathcal{N} \prod_{\varepsilon_j > 0} e^{\beta(\varepsilon_j + i\phi_j)} (1 + e^{-\beta(\varepsilon_j - \mu_q - i\phi_j)}) (1 + e^{-\beta(\varepsilon_j + \mu_q + i\phi_j)}). \quad (4.3.3)$$

where \mathcal{N} is the normalization factor. Here, we implicitly use the zeta-function regularization,

and see Ref. [137] for its derivation. Its μ_q -dependence at sufficiently low temperatures and at $\mu_q > 0$ becomes crystal clear according to the following expression [58, 137]:

$$\frac{\text{Det} [\gamma_4(\not{D}_A + m) - \mu_q]}{\text{Det} [\gamma_4(\not{D}_A + m)]} \simeq \prod_{0 < \varepsilon_j(A) \leq \mu_q} (1 + e^{-\beta(\varepsilon_j(A) - \mu_q)} e^{i\beta\phi_j(A)}). \quad (4.3.4)$$

The quark determinant becomes independent of μ_q at $T = 0$ if μ_q is smaller than the minimum of $\varepsilon_j(A) (> 0)$. For statistically significant gauge fields, it is confirmed that $\min(\varepsilon_j(A)) = m_\pi/2$ at $\mu_q = 0$ [58, 106, 137], and thus $n_B = 0$ for $\mu_q < m_\pi/2$. This also means that the Lefschetz-thimble decomposition of lattice QCD at $\mu_q < m_\pi/2$ and at sufficiently low temperatures is identical to the original integration cycle up to an exponentially small correction because the quark determinant at $\mu_q = 0$ is positive-definite.

In contrast, as computed in Eq. (4.2.18), the fermion determinant in the one-site fermion model is

$$\text{Det} \left[\partial_\tau - \left(i\varphi(\tau) + \mu + \frac{U}{2} \right) \right] = (1 + e^{-\beta(-U/2 - \mu)} e^{i\beta\varphi_{\text{bg}}})^2. \quad (4.3.5)$$

We can ask the same question: How can we show $n = 0$ for $\mu < 0$ using the path-integral expression when the fermion determinant depends on μ ? This Silver Blaze problem for $\mu < -U/2$ can be solved in the same manner for the baryon Silver Blaze problem at $\mu_{\text{qk}} < m_\pi/2$. At $\mu < -U/2$, the fermion determinant becomes independent of μ as $T \rightarrow 0$. This also explains why the Lefschetz thimble \mathcal{J}_* at $\mu < -U/2$ is almost identical to the original integration cycle \mathbb{R} (The similar discussion shows the Lefschetz thimble \mathcal{J}_* at $\mu > 3U/2$ is almost identical to the line with $\text{Im}(z) = 2$).

For $-U/2 < \mu < 0$, the μ -dependence of the fermion determinant (4.3.5) becomes exponentially large, and thus the property $n = 0$ at $T = 0$ is still veiled. At $\mu \simeq -U/2$, zeros of the fermion determinant (star-shape black points in Fig. 4.3) move close to the real axis, and let us recall that $\mathcal{J}_* = \mathbb{R}$ for $\mu < -U/2$ up to an exponentially small correction. In the case of one-site fermion model, this triggers Stokes jumps and the original integration cycle is decomposed into multiple Lefschetz thimbles for $\mu > -U/2$. One can no longer replace the expectation value of the number density by the number density at a complex saddle point. The significance of interference among multiple Lefschetz thimbles is identified in order to explain not only the rapid jumps of n but also the property $n = 0$ for $-U/2 < \mu < 0$ at the zero temperature. Furthermore, if the number of Lefschetz thimbles is insufficient, the thermodynamic stability is violated in the one-site fermion model.

We speculate that this interference of complex phases also play an important role in finite-density QCD to analyze the Silver Blaze problem and also the sign problem beyond half of the pion mass. For $\mu_{\text{qk}} > m_\pi/2$, the quark determinant becomes dependent on μ_{qk} and highly oscillatory on the statistically significant domain of real gauge fields. This means that zeros of the quark determinant around $\mu_{\text{qk}} \simeq m_\pi/2$ move closer to that domain. It would be natural to conclude that the statistically dominant region of the original integration cycle is decomposed into multiple Lefschetz thimbles around $\mu_{\text{qk}} \simeq m_\pi/2$. The complex phase of the fermion determinant becomes ill-defined at its zeros. Thus, the constant-phase condition of the integrand on a Lefschetz thimble would be hard to be satisfied without such decomposition, when zeros of the fermion determinant are located in the vicinity of the Lefschetz thimble.

Because of the complexity of QCD, we cannot show these statements so far. Future study of QCD-like models based on Lefschetz thimbles will be crucial to develop our understanding on the baryon Silver Blaze problem and on the finite-density QCD. Since the statistically significant

domain of real gauge fields can be partially mimicked by chiral random matrix models and by instanton liquid models, it would be desired to study those models from this viewpoint of Lefschetz thimbles.

4.4 Brief summary

In this chapter, we discussed the sign problem appearing in the path-integral expression of the partition function from the viewpoint of the Lefschetz-thimble approach.

In Sec. 4.1, we first establish a theorem which ensures the real-valuedness of physical observables. Since we have to complexify the integration variables to deform the integration contour, it is not obvious whether physical observables take real values in a manifest manner. Our analysis shows that the antilinear symmetry of the gradient flow is its key. If the system accepts the charge conjugation, we can construct the antilinear charge conjugation operation, and it ensures that physical observables take real values.

This theorem is helpful to understand the sign problem appearing in the mean-field approximation and in the perturbation theory. Since the fermion chemical potential makes the effective action complex, the gap equation in the mean-field approximation has no solution when the sign problem exists. This problem can be solved by applying the background field method and the Lefschetz-thimble analysis, which gives the mathematical foundation for the results of previous studies [113, 114]. This knowledge is used to analyze the heavy-dense QCD for a lucid demonstration of this method.

In Sec. 4.2, we apply the Lefschetz-thimble method to the one-site Fermi Hubbard model in order to understand the essence of difficulty hidden in the sign problem of finite-density QCD. The one-site Hubbard model is quite simple but its path-integral expression has the severe sign problem. If the phase-quenched approximation is applied, the fictitious phase transition appears at $\mu = -U/2$ although the number density must stay zero until $\mu = 0$. This reminds us what happens for QCD, because phase-quenched QCD experiences the second-order phase transition at $\mu_q = m_\pi/2$ although there is nothing until the liquid-vapor phase transition $\mu_q = (m_N - B)/3$. Therefore, the one-site Hubbard model has a severe Silver Blaze problem.

Using the Lefschetz-thimble approach to the path integral, we succeeded to unveil the secret of this Silver Blaze problem for the one-site Hubbard model. For $\mu < -U/2$, we can apply the complex mean-field approximation described in Sec. 4.1. Around $\mu = -U/2$, the Stokes jumping happens because of fermionic zero modes, and the topological structure of Lefschetz thimbles drastically changes, and the situation totally changes. In order to explain the Silver Blaze phenomenon, the interference of complex phases among complex saddle points play a pivotal role. We discuss Lee–Yang zeros within the semiclassical analysis, and the correct phase transition can be explained in a clear way.

Based on the semiclassical analysis, the necessary number of Lefschetz thimbles is estimated. It is proportional to the inverse temperature, $\beta U/2\pi$, and we confirmed its correctness by using the numerical computation. We hope this analysis suggests the general strategy to evaluate the difficulty of tackling the sign problem using the Lefschetz-thimble approach.

In Sec. 4.3, we discuss the implication on the Silver Blaze problem of finite-density QCD based on our analysis of the one-site Hubbard model. These theories share the difficulty of the sign problem from various points of view. Outside of the pion condensation of the phase-quenched QCD, the contributing Lefschetz thimbles would not have different complex phases. This means that we can apply the complex mean-field approximation or also other conventional

approaches to the sign problem. If $\mu_q > m_\pi/2$, then the fermion determinant would divide the integration cycle into multiple Lefschetz thimbles with different complex phases. In summing up those phases, the baryon number density stays zero, which breaks our naive expectation obtained from the pion condensation in the phase-quenched theory. This speculation must be justified/denied in the future to deepen our understanding on the baryon Silver Blaze problem.

Chapter 5

Complex Langevin method revisited via Lefschetz-thimble integrals

The complex Langevin method has been considered as a sign problem solver for a long time. Even how severe the sign problem is, this method solve it for some cases. However, it is also known that the complex Langevin method shows wrong convergence in other cases, and this situation is annoying when we apply it to the strongly-correlated systems.

In Sec. 5.1, we show a simple criterion for incorrectness of the complex Langevin method by relating it with the Lefschetz-thimble path integral through the Dyson–Schwinger equation. This clearly shows that the naive complex Langevin method cannot solve the Silver Blaze phenomenon at finite-density QCD for $\mu > m_\pi/2$. In Sec. 5.2, we propose to revise the complex Langevin method to evade the proof of its incorrectness. We check our criterion for the incorrectness numerically for two zero-dimensional examples, and test the modified complex Langevin method.

The discussion in this chapter is adapted from Ref. [138].

5.1 Complex Langevin method and its failure

After a brief review of the complex Langevin method, we show that it gives wrong convergence in generic cases by relating it with the Lefschetz-thimble path integral.

5.1.1 Brief review on basics of complex Langevin method

For simplicity, we discuss an oscillatory integral of one variable x , which can be extended to multiple integrals in a straightforward way,

$$\langle O(x) \rangle = \frac{1}{Z} \int_{\mathbb{R}} dx e^{-S(x)/\hbar} O(x). \quad (5.1.1)$$

The classical action $S(x)$ is complex valued in general, which makes the Monte Carlo simulation of (5.1.1) difficult because of the sign problem. One proposal for solving the sign problem is to take the noise average of the solution of the classical equation of motion with random noises [139–142]. For this purpose, we need to solve the Langevin equations for complex values z along the fictitious time direction

$$\partial_\theta z_\eta(\theta) = -S'(z_\eta(\theta)) + \sqrt{\hbar} \eta(\theta), \quad (5.1.2)$$

with θ being the continuous fictitious time. $\eta(\theta)$ is real Gaussian noises satisfying $\langle \eta(\theta) \rangle_\eta = 0$ and $\langle \eta(\theta)\eta(\theta') \rangle_\eta = 2\delta(\theta - \theta')$. The function z_η shows the classical trajectory of the system when the random force η is fixed. Since the action $S(x)$ is complex, the right-hand side of Eq. (5.1.2) is complex. Thus, complexification of the variable z is unavoidable, and this method is named the complex Langevin method.

For that purpose, let us review the result of Itô calculus. We can restrict our consideration on the set of holomorphic operators $O(z)$ for later purpose. The stochastic calculus shows that

$$\frac{d}{d\theta} \langle O(z_\eta(\theta)) \rangle_\eta = \hbar \langle O''(z_\eta(\theta)) \rangle_\eta - \langle O'(z_\eta(\theta)) S'(z_\eta(\theta)) \rangle_\eta. \quad (5.1.3)$$

If we assume that the expectation values reach equilibrium, then the set of expectation values satisfy the Dyson–Schwinger equation:

$$\lim_{\theta \rightarrow \infty} \langle O'(z_\eta(\theta)) S'(z_\eta(\theta)) \rangle_\eta = \lim_{\theta \rightarrow \infty} \hbar \langle O''(z_\eta(\theta)) \rangle_\eta. \quad (5.1.4)$$

The real Langevin method is equivalent to the path-integral quantization; if $S(x)$ were real, the ensemble average $\langle O(x_\eta(\theta)) \rangle_\eta$ can be shown to converge into (5.1.1) as $\theta \rightarrow \infty$ by rewriting this Dyson–Schwinger equation into the Fokker–Planck equation [143]. There is a folklore theorem stating that the complex Langevin method also gives correct expectation values, but let us first show that it is true only for very restricted cases in the next subsection. After that, we propose a new prescription to evade this breakdown.

5.1.2 Semiclassical inconsistency

In the following, we assume that expectation values of holomorphic operators $O(z)$ converge as $\theta \rightarrow \infty$. As we have already seen, Itô calculus shows that they must satisfy the Dyson–Schwinger equation

$$\langle O(z_\eta) S'(z_\eta) \rangle_\eta = \hbar \langle O'(z_\eta) \rangle_\eta. \quad (5.1.5)$$

Here the argument $\theta = \infty$ of z is omitted. The Lefschetz-thimble method shows that the expectation value of the holomorphic operator $O(z)$ at $\theta \rightarrow \infty$ can be represented, by using a sum of complex contour integrals on steepest descent paths \mathcal{J}_σ of $\text{Re } S(z)$ ($\sigma \in \Sigma$ labels the critical points z_σ of S) [64, 65, 76], as

$$\langle O(z_\eta) \rangle_\eta = \frac{1}{Z} \sum_{\sigma \in \Sigma} d_\sigma \int_{\mathcal{J}_\sigma} dz e^{-S(z)/\hbar} O(z). \quad (5.1.6)$$

Here, d_σ is a complex number in general. If and only if d_σ is an intersection number $\langle \mathcal{K}_\sigma, \mathbb{R} \rangle$ between the steepest ascent path \mathcal{K}_σ and the original integration path \mathbb{R} , the original integration (5.1.1) is obtained:

$$\langle O(z_\eta) \rangle_\eta = \frac{1}{Z} \int_{\mathbb{R}} dx e^{-S(x)/\hbar} O(x) \Leftrightarrow d_\sigma = \langle \mathcal{K}_\sigma, \mathbb{R} \rangle. \quad (5.1.7)$$

We already proved in Sec. 2.2 that each integration on Lefschetz thimble respect the Dyson–Schwinger equation. Another linearly independent solution does not exist since the Dyson–Schwinger equation requires that $S'(z) = 0$ in the limit $\hbar \rightarrow 0$, which is nothing but the saddle-point condition. Thus, all the possible integration cycles must be associated with complex saddle points.

Let us take the semiclassical limit $\hbar \rightarrow +0$ of (5.1.6). For semiclassical analysis, we expand $S(z)$ around each complex saddle point z_σ as

$$S(z_\sigma + \delta z) = S_\sigma + \frac{\omega_\sigma}{2} \delta z^2 + O(\delta z^3). \quad (5.1.8)$$

Let us first analyze the left hand side of (5.1.6). If $\text{Re } \omega_\sigma > 0$, the solution of the equation of motion (5.1.2) can converge into z_σ as $\theta \rightarrow \infty$ in the limit of $\hbar \rightarrow 0$. On the other hand, it is impossible for $\text{Re } \omega_\sigma \leq 0$. In the semiclassical approximation, we have

$$\langle O(z) \rangle_\eta \simeq \sum_\sigma c_\sigma O(z_\sigma), \quad (5.1.9)$$

where $c_\sigma \geq 0$, and $c_\sigma = 0$ if $\text{Re } \omega_\sigma \leq 0$. Next let us analyze the right hand side of (5.1.6). In the semiclassical approximation, the integration along the thimble becomes

$$\int_{\mathcal{J}_\sigma} dz e^{-S(z)} \mathcal{O}(z) \simeq \sqrt{\frac{2\pi\hbar}{\omega_\sigma}} e^{-S_\sigma/\hbar} \mathcal{O}(z_\sigma). \quad (5.1.10)$$

Now, we reach

$$c_\sigma = \frac{1}{Z} \sqrt{\frac{2\pi\hbar}{\omega_\sigma}} e^{-S_\sigma/\hbar} d_\sigma. \quad (5.1.11)$$

Notice that $c_\sigma \geq 0$, however, d_σ must be an integer $\langle \mathcal{K}_\sigma, \mathbb{R} \rangle$ in order to give the original integration (5.1.1). These two statements clearly contradict with one another for generic cases, especially when there are several dominant saddle points with different complex phases. Therefore, complex Langevin methods cannot reproduce original integrals at least in the semiclassical limit.

Let us give a notice about subdominant saddle points. Since the Borel resummation of higher-order perturbations may cancel the subdominant contributions of complex saddle points, we need a careful case-by-case study in order to conclude inconsistency from the above arguments. Nevertheless, we strongly believe that the above argument is still robust and applicable to judge the breakdown of complex Langevin method for wide class of classical actions $S(x)$. We give a clear and simple criterion for the incorrectness of the complex Langevin method.

Let us give a few comment on previous studies. There is a formal proof [144, 145] on the correctness of complex Langevin method, but it relies on several nontrivial assumptions. Recent study [146] elucidates that this assumption is questionable especially if some singularities exist in complex classical action $S(x)$, such as poles or branch points. Our semiclassical analysis show that this breakdown happens in more generic cases. Furthermore, our criterion for incorrectness of the complex Langevin method can be applied before performing the complex Langevin simulations.

5.2 Modification of complex Langevin method

In the previous section, we showed that the complex Langevin method gives an unphysical solution of the Dyson–Schwinger equation in generic cases. We give a trial to modify the complex Langevin method in order to evade the semiclassical inconsistency. Although this trial is still incomplete, it may open a way to perform numerical multi-thimble lattice simulation, which has not yet been achieved in the current technology.

5.2.1 Proposal to modify complex Langevin method

Let us assume that if $\text{Re } \omega_\sigma \leq 0$ then $\langle \mathcal{K}_\sigma, \mathbb{R} \rangle = 0$ for a complex classical action $S(z)$. Otherwise, the number of contributing saddle points in the semiclassical limit is different between the complex Langevin method and the original integral. In such cases, I have no idea how to modify the complex Langevin method to evade this inconsistency. Therefore, we require that $S(x)$ satisfy this restriction.

Let us propose a way to circumvent the inconsistency of semiclassical analysis by adopting this conjecture as a working principle. We denote the equilibrium distribution of the complex Langevin method by P i.e., $\langle O(z) \rangle_\eta = \int dx dy P(x, y) O(x + iy)$. In the semiclassical limit, P will be approximated as a sum of localized distributions P_σ around complex saddle points z_σ , as $P = \sum_\sigma c_\sigma P_\sigma$, which gives the expectation value (5.1.9). Here, each P_σ is a normalized probability density that localizes around z_σ . In order to evade the inconsistency, we need to introduce another distribution function,

$$\tilde{P}(x, y) = \frac{1}{Z} \sum_\sigma \langle \mathcal{K}_\sigma, \mathbb{R} \rangle \sqrt{\frac{2\pi\hbar}{\omega_\sigma}} e^{-S_\sigma/\hbar} P_\sigma(x, y). \quad (5.2.1)$$

Here, Z is a normalization factor, as usual. As a result, the new average $\int dx dy \tilde{P}(x, y) O(x + iy)$ follows the correct semiclassical limit, and thus the Dyson–Schwinger equation is not violated at the semiclassical level. In order to represent this new average as an ensemble average, introduce the following phase function,

$$\Phi(x, y) = \sum_\sigma \frac{\langle \mathcal{K}_\sigma, \mathbb{R} \rangle \sqrt{\frac{2\pi\hbar}{\omega_\sigma}} e^{-S_\sigma/\hbar}}{c_\sigma} \chi_\sigma(x, y), \quad (5.2.2)$$

where χ_σ is almost the characteristic function of $\text{supp}(P_\sigma)$ so that $\chi_\sigma P_\tau \simeq \delta_{\sigma\tau} P_\tau$ because of locality of P_σ . When $c_\sigma = 0$, we must put $\chi_\sigma = 0$. Using this phase function, we can easily find that

$$\int dx dy \tilde{P}(x, y) O(x + iy) = \frac{\langle \Phi(x_\eta, y_\eta) O(x_\eta + iy_\eta) \rangle_\eta}{\langle \Phi(x_\eta, y_\eta) \rangle_\eta}. \quad (5.2.3)$$

This seems to be the only way to circumvent the inconsistency in the semiclassical limit for the complex Langevin method. However, we must give a notice that this prescription contains several unsolved problems to be tackled: (i) Phase factors are calculated in the semiclassical limit, and they can suffer from higher order corrections of \hbar . (ii) In order to apply this prescription, we must compute c_σ in (5.1.9) and its higher order corrections in \hbar . (iii) When \hbar is not so small, P does not necessarily localize around saddle points and thus we may not be able to find good characteristic functions χ_σ . We must evaluate an error affected by this failure of the prescription in order to give a reliable prediction.

The first problem (i) is not a big deal, because we can compute higher order corrections by usual perturbation theory. The third problem (iii) can be a fatal disease for strongly coupled systems if quantum fluctuations give huge corrections. This must be an important future task when the complex Langevin method is applied. The second one (ii) may look similar to the first one, but there is no standard way to compute c_σ to my best knowledge. Since the Fokker–Planck operator of the complex Langevin method is non-Hermitian, the developed techniques in quantum mechanics are not necessarily useful.

In order to demonstrate that this prescription may work well, we put a working hypothesis on c_σ . Let us assume that

$$c_\sigma = \langle \mathcal{K}_\sigma, \mathbb{R} \rangle \left| \int_{\mathcal{J}_\sigma} dz e^{-S(z)} \right| \simeq \sqrt{\frac{2\pi\hbar}{|\omega_\sigma|}} e^{-\text{Re } S_\sigma/\hbar} \langle \mathcal{K}_\sigma, \mathbb{R} \rangle. \quad (5.2.4)$$

This solution means that the complex Langevin method gives an extension of the so-called phase quenched approximation so as to include complex saddle points:

$$\langle O(z_\eta) \rangle_\eta \simeq \frac{1}{Z'} \sum_\sigma \langle \mathcal{K}_\sigma, \mathbb{R} \rangle \sqrt{\frac{2\pi\hbar}{|\omega_\sigma|}} e^{-\text{Re } S_\sigma/\hbar} O(z_\sigma). \quad (5.2.5)$$

Note that there are many other possibility to satisfy semiclassical consistency. This is just a one of possibilities and it has not been proven that this is indeed the solution of the complex Langevin method. Computation of c_σ directly from the complex Langevin method is of great importance if one would like to solve the sign problem using it.

Once we adopt this working hypothesis on c_σ , we can write down the phase function Φ in an explicit manner as

$$\Phi = \sum_\sigma \langle \mathcal{K}_\sigma, \mathbb{R} \rangle \sqrt{\frac{|\omega_\sigma|}{\omega_\sigma}} e^{-i \text{Im}(S_\sigma)/\hbar} \chi_\sigma. \quad (5.2.6)$$

The expectation values of holomorphic operators are computed by (5.2.3).

5.2.2 Numerical test of the proposal

In this section, we check that our criterion for incorrectness of the complex Langevin method, and test our proposal of modification by applying it to two examples with and without a singular drift term. As a nonsingular potential, we consider the double-well potential with a complex linear term, which is called the complex double-well potential here. As a singular one, we consider the one-site Fermi Hubbard model which is studied in Sec. 4.2 using Lefschetz thimbles.

Complex double-well potential The first example is a nonsingular action

$$S(x) = \frac{x^4}{4} - \frac{x^2}{2} - i\alpha x, \quad (5.2.7)$$

with $\alpha > 0$. This action has three saddle points on the complex plane, and let us see their properties in the limit $\alpha \rightarrow +\infty$. In the case $\alpha \gg 1$, the x^2 term in (5.2.7) becomes negligible and we can give simple expressions for three saddle points as

$$z_1 \simeq \alpha^{1/3} e^{\pi i/6}, \quad z_2 \simeq \alpha^{1/3} e^{5\pi i/6}, \quad z_0 \simeq \alpha^{1/3} e^{-\pi i/2}. \quad (5.2.8)$$

Around these points, we evaluate the classical action as

$$S(z_1 + \delta z) \simeq -\frac{3}{4} \alpha^{4/3} e^{2\pi i/3} + 3\alpha^{2/3} e^{\pi i/3} \delta z^2, \quad (5.2.9)$$

$$S(z_2 + \delta z) \simeq -\frac{3}{4} \alpha^{4/3} e^{-2\pi i/3} + 3\alpha^{2/3} e^{-\pi i/3} \delta z^2, \quad (5.2.10)$$

$$S(z_0 + \delta z) \simeq -\frac{3}{4} \alpha^{4/3} - 3\alpha^{2/3} \delta z^2. \quad (5.2.11)$$

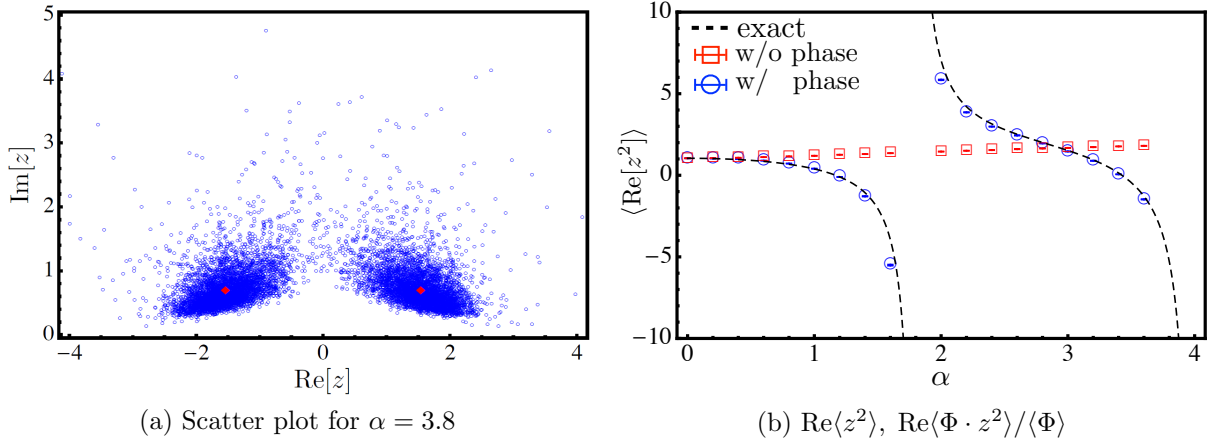


Figure 5.1: Test of the complex Langevin method for the complex double-well potential $S(x) = x^4/4 - x^2/2 + i\alpha x$ with $\alpha > 0$. (a) Scatter plot obtained by the complex Langevin for $\alpha = 3.8$. For large α , two local distributions around saddle points are well separated. (b) Expectation values of z^2 . The red boxes are obtained by the original complex Langevin method, and the blue circles by our new formula (5.2.3). (Figure (b) is taken from Ref. [138].)

Only two of them, z_1 and z_2 , have positive $\text{Re}[\omega_\sigma]$ as we can easily see, and contribute to the Langevin simulation in the semiclassical limit $\alpha \rightarrow \infty$. In the present model, the same is true for the Lefschetz-thimble method, and only these two saddle points give contributions in the Lefschetz-thimble decomposition:

$$\begin{aligned} Z(\alpha) &= \int_{\mathcal{J}_1} dz e^{-S(z)} + \int_{\mathcal{J}_2} dz e^{-S(z)} \\ &\simeq \sqrt{\frac{\pi}{3\alpha^{2/3}}} e^{-3\alpha^{4/3}/8} \cos\left(\frac{3\sqrt{3}}{8}\alpha^{4/3} + \frac{\pi}{6}\right). \end{aligned} \quad (5.2.12)$$

The last expression is the asymptotic expression which is valid only for $\alpha \gg 1$, but it clearly tells us the oscillatory behavior of the partition function. This oscillatory behavior comes from interference of complex phases between dominant saddle points $z_{1,2}$, and thus the naive complex Langevin method is expected to give wrong results for this model.

We numerically solved the complex Langevin equations with the fictitious time step $\varepsilon = 5.0 \times 10^{-7}$. We adopted a higher order algorithm [147], and errors were estimated by using the jackknife method. The result for $\langle z^2 \rangle$ is shown in Fig. 5.1 (b). The red squares show the result for the naive complex Langevin method, and they are clearly incorrect as we expected.

Let us try our proposal on modification of the complex Langevin method. Since there are two contributing saddle points with $\text{Re}[z_1] > 0$ and $\text{Re}[z_2] < 0$, we divide the complex plane \mathbb{C} into two regions for positive and negative real parts (See Fig. 5.1 (a)). We introduce the phase function by

$$\Phi(x, y) = \sum_{\sigma=1,2} \sqrt{\frac{|S''(z_\sigma)|}{S''(z_\sigma)}} e^{-i\text{Im}S(z_\sigma)} \theta((-1)^{\sigma+1}x), \quad (5.2.13)$$

where $\theta(x)$ is the Heaviside step function. Here, saddle points $z_{1,2}$ are computed exactly, although we only showed their approximate expressions for $\alpha \gg 1$ in (5.2.8). The result for $\langle \Phi(x, y) z^2 \rangle / \langle \Phi \rangle$ is shown with blue circles in Fig. 5.1 (b), and those points are roughly

consistent with the exact result (black dashed line). Especially for large α 's, our prescription on the modification works nicely for this model.

We numerically checked whether the Dyson–Schwinger equation is satisfied for this model, but it turns out not to be satisfied for z^n with $n > 3$. The equilibrium probability distribution seems to show a power-law decay in the $\text{Im}(z)$ direction for this model, and this might be a reason for this illness. Our criterion for incorrectness still gives the sufficient condition for the complex Langevin method to break down, and we can clearly see it in this example. What is surprising is that our prescription of the modified complex Langevin works nicely for z^n with $n \leq 4$ in this case, and it is an open problem to understand its reason.

One-site Fermi Hubbard model Next, we analyze the action with a logarithmic singularity. We analyze the one-site Fermi Hubbard model studied in Sec. 4.2, which is the simplest model and shows the severe sign problem like finite-density QCD (see also Refs. [128, 132–134]). For reader's convenience, let us briefly describe properties of this model again.

The Hamiltonian of this model (4.2.2) is given by

$$\hat{H} = U\hat{n}_\uparrow\hat{n}_\downarrow - \mu(\hat{n}_\uparrow + \hat{n}_\downarrow), \quad (5.2.14)$$

with $\hat{n}_s = \hat{c}_s^\dagger \hat{c}_s$. At the zero temperature, this system shows the first-order phase transitions at $\mu/U = 0, 1$. A path-integral expression of the partition function $Z = \text{tr} \left[\exp \left(-\beta \hat{H} \right) \right]$ is given by the following one-variable integral (4.2.19),

$$Z = \sqrt{\frac{\beta}{2\pi U}} \int d\varphi_{\text{bg}} \left(1 + \exp \beta \left(i\varphi_{\text{bg}} + \mu + \frac{U}{2} \right) \right)^2 \exp -\frac{\beta}{2U} \varphi_{\text{bg}}^2. \quad (5.2.15)$$

The expectation value of the number density can be computed as $n = \text{Im}\langle\varphi\rangle/U$. For $\mu/U < -0.5$ or $\mu/U > 1.5$, behaviors of the number density can be easily described just by solving the classical equation of motion, which comes from the fact that the μ -dependence of the fermion determinant becomes trivial. What was difficult to understand in this path-integral expression is the step-function behaviors of n for $-0.5 < \mu/U < 1.5$, and the sign problem in this region is expected to have strong connection with that of finite-density QCD at $m_\pi/2 < \mu < m_N/3$.

Let us again stick to the case $-0.5 < \mu/U < 1.5$, since this is the best testing ground for the complex Langevin method. In this region, the contributing complex classical solutions (4.2.28) are labeled by integers $m \in \mathbb{Z}$ as ($\beta U \gg 1$)

$$z_m \simeq i \left(\mu + \frac{U}{2} \right) + T \left(2\pi m + i \ln \frac{\frac{3}{2}U - \mu}{\frac{U}{2} + \mu} \right). \quad (5.2.16)$$

At these saddle points, the classical action is evaluated as

$$\text{Re}(S_m - S_0) \simeq \frac{2\pi^2}{\beta U} m^2, \quad (5.2.17)$$

$$\text{Im} S_m \simeq 2\pi m \left(\frac{\mu}{U} + \frac{1}{2} \right). \quad (5.2.18)$$

In this model, the most dominant contributions comes only from a saddle point z_0 , and then, strictly speaking, one cannot apply our proof of incorrectness of the complex Langevin method.

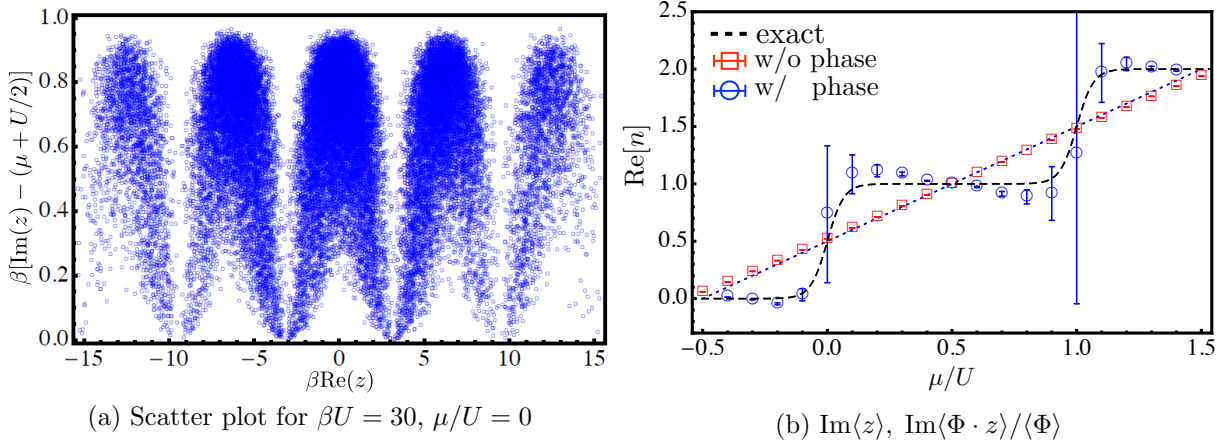


Figure 5.2: Test of the complex Langevin method for the one-site Fermi Hubbard model. (a) Scatter plot obtained by the complex Langevin method for $\beta U = 30$ and $\mu/U = 0$. This has a remarkable similarity with Fig. 4.3 (b). (b) The red boxes are obtained by the original complex Langevin method, and the blue circles by our new formula (5.2.3). (Figure (b) is taken from Ref. [138].)

However, other saddle points z_m ($m \neq 0$) also give almost dominant contributions at $\beta U \rightarrow \infty$ as long as $|m|$ is not too large. This suggests that our criterion can still conclude that the complex Langevin method shows wrong convergence in this model. That is, because of the difference of complex phases among S_m , the complex Langevin method is expected to give a wrong answer for this model.

Figure 5.2 (a) shows the scatter plot obtained by the complex Langevin method obtained by the complex Langevin method. Here, $\text{Im}(z)$ is subtracted by the offset $\mu + U/2$ in order to look at details of the distribution. They do not show step-function behaviors and instead show the linear dependence on μ . It is quite similar to the structure of Lefschetz thimbles in Fig. 4.3 (b), and the distribution is nicely separated by fermionic zero modes. The result for the number density of the naive complex Langevin method is shown with red squares in Fig. 5.2 (b). This is expected because the position of the complex saddle points is $\text{Im}(z_m)/U \simeq \mu/U + 1/2$, and this indicates that the complex Langevin method at least loses the complex phases among saddle points.

We introduce the phase function Φ by

$$\Phi(x, y) = \sum_{m=-\infty}^{\infty} e^{-i \text{Im} S_m} \theta\left((2m-1)\pi < \beta x < (2m+1)\pi\right). \quad (5.2.19)$$

The result of the modification, $\text{Im}\langle\Phi \cdot z\rangle/\langle\Phi\rangle$, is shown with blue circles in Fig. 5.2 (b). Although we cannot observe the perfect agreement between our modified computation of the complex Langevin method and the exact result, step-function behaviors can be observed after modification. It is an important future study to refine the modification procedure and explore the Silver Blaze phenomenon using the modified complex Langevin method.

5.3 Brief summary

In this chapter, we discussed the relation between the Lefschetz-thimble path integral and the complex Langevin method through the Dyson–Schwinger equation. Establishment of this

relation enables us to give feedbacks from our new findings on the Lefschetz-thimble approach for other approaches to the sign problem, and vice versa.

In Sec. 5.1, we formally relate the complex Langevin method and the Lefschetz-thimble path integral by using Itô calculus. Since Itô calculus gives the Dyson–Schwinger equation if the Langevin dynamics equilibrates, the ensemble averages of the complex Langevin method must be given by a complex linear combination of Lefschetz-thimble integrals. Only when it is given by the linear combination with appropriate integers, does the complex Langevin method simulate the original quantum system.

Using the semiclassical analysis, we derived the sufficient condition for the complex Langevin method to show the wrong convergence. This condition is quite simple: The complex Langevin method is always wrong if the classical action has several dominantly contributing saddle points with different complex phases.

Since we have identified a missing part in the complex Langevin simulation, we can propose a way to change the complex Langevin method in Sec. 5.2. Since the phase factors appearing in summing up multiple Lefschetz thimbles are missed, we introduce them and perform the reweighting. This is the minimal modification in order to circumvent the semiclassical inconsistency in Sec. 5.1.

Our proposal is checked numerically. If we apply the complex Langevin method to the one-site Hubbard model, it shows the fictitious phase transition which we observed with the phase-quenched approximation in Sec. 4.2. After performing the reweighting, the result on the number density is improved and shows a rapid transition at correct values of the chemical potential.

Chapter 6

Summary and Outlook

In Chapter 2, I first give a brief review on a foundation of the Picard–Lefschetz theory. This gives an extension of steepest descent methods by applying it to the multiple oscillatory integral, and the steepest descent integration cycles are called Lefschetz thimbles. In order to understand how it works, I compute the real-time Feynman kernels of free particles and the harmonic oscillator.

In Chapter 3, spontaneous breaking of chiral symmetry is discussed from the viewpoint of the Lefschetz-thimble approach. This study tackles one of the important aspects of nonperturbative QCD using simple 0-dimensional fermionic models, Gross–Neveu and Nambu–Jona-Lasinio models. In both cases, an auxiliary bosonic field for the chiral condensate is introduced, and its integration cycle is decomposed into Lefschetz thimbles. This allows ones to study the analytic property of the partition function for complex four-fermion interactions before performing the path integral. Thanks to this property, one can easily compute Lee–Yang zeros of these models in the large- N limit.

In this chapter, I also develop the computational tool of Lefschetz thimbles with the continuous chiral symmetry. The Lefschetz thimble method can be naively applicable only when all the saddle points are non-degenerate, which is not the case if there exists an exact continuous symmetry. Even when the continuous symmetry is explicitly broken, the remnant of the symmetry introduces a practical difficulty in its application because of the appearance of quasi-zero modes. I find that the quasi-zero mode of the gradient flow can be decoupled approximately, and Lefschetz thimbles become computable in an efficient way. This technique turns out to be quite useful, and it is applied for the 0-dimensional Nambu–Jona-Lasinio model.

In Chapter 4, I consider two examples with the sign problem in order to understand the origin and structures of the sign problem. The first one is the Polyakov-loop effective model of the heavy-dense quantum chromodynamics (QCD). In order to study it, I developed the mean-field approximation based on the Lefschetz-thimble approach so that it is applicable even if the sign problem exists. One can judge whether this works nicely by computing topologies of Lefschetz thimbles. This gives the mathematical foundation to study the Polyakov-loop effective models at finite quark densities.

The second one is the one-site Fermi Hubbard model, which is easily and exactly solvable but has the severe sign problem in the path-integral expression. In this case, the above mean-field approximation is not applicable, and I elucidate its reason by studying topological structures of Lefschetz thimbles. I show that interference of complex phases among complex classical solutions play a pivotal role to understand the sign problem and the correct phase structures using path integrals. This interference is shown to become also important in the finite-density QCD with light flavors if the baryon chemical potential exceeds the pion mass.

In Chapter 5, I relate this newly developing technique, the Lefschetz-thimble path integral, with a conventional approach to the sign problem, the complex Langevin method. I show that the original complex Langevin method cannot give correct results if interference of complex phases among classical solutions is important. This gives the simple criterion for incorrectness of the complex Langevin method without doing its numerical simulation, and suggests that the complex Langevin method is not applicable to the finite-density QCD. To resolve this failure, I propose to modify the complex Langevin method and it is numerically tested. Our proposal on modification improves the result for the one-site Hubbard model but it is not perfect yet. This study strongly suggests that the Lefschetz-thimble approach is quite powerful to invent or justify other sign problem solvers.

In this thesis, I elucidate what is an essential difficulty of the sign problem when the path-integral formulation is applied. This requires some changes or modifications of conventional approaches to the sign problem, and this study may be able to infer how to do them. For that purpose, I must study further details and evaluate the amount of computational costs. Especially, it is important to understand the structures of Lefschetz thimbles when the system has infinitely many degrees of freedom.

In order to explore the phase diagram of QCD using the path-integral approach, I believe that we must further develop the theoretical and technical foundations of Lefschetz-thimble methods. It is quite important to fully understand how the sign problem in finite-density QCD is correlated to the low-energy dynamics of QCD characterized by confinement and spontaneous chiral symmetry breaking. Each aspect of the problem is partly explored in this thesis, and I would like to know how these results play into the realistic problems. As a next step, it is interesting to revisit the structure of the sign problem in the chiral random matrix model and the instanton liquid model. These models simplify the dynamics of gauge fields in QCD, and thus one would be able to learn how the chiral symmetry breaking affects the difficulty of the sign problem in an explicit way. It is fascinating if these studies shed a new light on the cold and dense nuclear matters and a longstanding and new problems of neutron stars.

So far, the path integral on Lefschetz thimbles relies on sophisticated mathematics. Its applications can be discussed based on solid mathematical foundations thanks to this aspect. However, if one could relate this analysis with our conventional physical intuition on quantum field theories, then this method must have wider applications and become practical tools. I believe that this is possible, because this method is suitable for the semiclassical study of quantum physics. Dynamical aspects of field theories, such as real-time phenomena, have vast unexplored areas compared with static ones, and I would like to tackle those problems in future by extending the applicability of this technique.

Appendix A

Homology

A.1 General property

Homology can be defined in a quite abstract way, and it is sometimes useful to compute the homology since we can deal them without considering details of its construction. Therefore, let us just remark the Eilenberg–Steenrod axioms [148] of the homology at first.

Eilenberg–Steenrod axiom

For every pair (X, A) of topological spaces, i.e. $A \subset X$, Abelian groups $H_i(X, A)$ ($i \geq 0$) and boundary maps $\partial : H_i(X, A) \rightarrow H_{i-1}(A, \emptyset)(=: H_{i-1}(A))$ are assigned, and a map of pairs $f : (X, A) \rightarrow (Y, B)$ induces a group homomorphism $f_* : H_n(X, A) \rightarrow H_n(Y, B)$. They further satisfy the following five axioms:

1. **[Naturalness]** The boundary map ∂ is natural, i.e. for a map $f : (X, A) \rightarrow (Y, B)$ the induced maps must commute with ∂ ; $f_* \circ \partial = \partial \circ (f|_A)_*$.
2. **[Homotopy]** If two maps $f, g : (X, A) \rightarrow (Y, B)$ is homotopic, the induced maps f_*, g_* to the homology are the same.
3. **[Excision]** Let (X, A) be a pair and $U \subset A$. If the closure of U is inside the interior of A , then the inclusion $(X \setminus U, A \setminus U) \hookrightarrow (X, A)$ induces $H_i(X \setminus U, A \setminus U) = H_i(X, A)$.
4. **[Dimension]** For the one-point set $*$, $H_i(*) = 0$ for $i > 0$. In the singular homology, $H_0(*) = \mathbb{Z}$.
5. **[Additivity]** Let X is given by a disjoint union of X_α 's, then $H_i(X) = \bigoplus_\alpha H_i(X_\alpha)$.
6. **[Exactness]** For each pair (X, A) , two inclusions $i : A \hookrightarrow X$ and $j : (X, \emptyset) \hookrightarrow (X, A)$ induces the long exact sequence

$$\cdots \xrightarrow{\partial} H_n(A) \xrightarrow{i_*} H_n(X) \xrightarrow{j_*} H_n(X, A) \xrightarrow{\partial} H_{n-1}(A) \xrightarrow{i_*} \cdots \quad (\text{A.1.1})$$

With these axioms, the homology can be uniquely determined. For some topological spaces like spheres, one can compute their homologies directly from these axioms.

If one were familiar with the homology group $H_n(X)$ but not with the relative homology group $H_n(X, A)$, one can think of $H_n(X, A)$ as $H_n(X/A)$ for $n > 0$ (for singular homologies). For $n = 0$, $H_0(X, A) = H_0(X/A, *)$ and it is the free module of one rank less than $H_0(X/A)$. These properties follow from the excision axiom.

Mayer–Vietoris exact sequence

The Mayer–Vietoris sequence provides a helpful way to compute the homologies, and this theorem follows from the above Eilenberg–Steenrod axioms. Let $A, B \subset X$ be topological subspaces of X , and X be covered by interiors of A and B . We can consider natural inclusions $i : A \cap B \hookrightarrow A$, $j : A \cap B \hookrightarrow B$, $k : A \hookrightarrow X$, and $l : B \hookrightarrow X$, then the Mayer–Vietoris sequence states that the following is the long exact sequence:

$$\cdots \rightarrow H_n(A \cap B) \xrightarrow{(i_*, j_*)} H_n(A) \oplus H_n(B) \xrightarrow{k_* - l_*} H_n(X) \xrightarrow{\partial_*} H_{n-1}(A \cap B) \rightarrow \cdots \quad (\text{A.1.2})$$

The map ∂_* needs a little explanation. Let us set $U = B \setminus A$, then the closure of U is contained in B because X is covered by interiors of A and B by the assumption. Using the excision property, one finds

$$H_n(X, B) \simeq H_n(X \setminus U, B \setminus U) = H_n(A, A \cap B). \quad (\text{A.1.3})$$

Then, ∂_* is given by the composition,

$$\partial_* : H_n(X) \rightarrow H_n(X, B) \simeq H_n(A, A \cap B) \xrightarrow{\partial} H_{n-1}(A \cap B). \quad (\text{A.1.4})$$

For spheres S^k , this states that $H_n(S^k) = H_{n-1}(S^{k-1})$ by dividing it into two hemispheres. In the case of singular homologies, one can iteratively show that $H_0(S^k) = H_k(S^k) = \mathbb{Z}$ and $H_n(S^k) = 0$ for $n \neq 0, k$.

A.2 Smale–Witten theory

Morse homology provides a useful way to understand homologies of compact smooth manifolds. Semiclassical analysis of a supersymmetric quantum mechanics gives a physical idea of homologies [149, 150]. For its relevant extension in our context, see Refs. [151–154].

Morse inequalities Let (M, g) be a smooth Riemannian manifold with finite dimension, and consider $h : M \rightarrow \mathbb{R}$. For a moment, let us assume that M is compact. The function h is called a **Morse function** on M if all the critical points $p \in \Sigma = \{x \in M \mid dh(x) = 0\}$ is non-degenerate, i.e.

$$\det \left(\frac{\partial^2 h}{\partial x^i \partial x^j} \right) \Big|_p \neq 0. \quad (\text{A.2.1})$$

For each critical point p , the Morse index $\lambda(p)$ is defined by the number of negative eigenvalues of the Hessian.

The strong Morse inequality gives

$$\sum_{p \in \Sigma} t^{\lambda(p)} - \sum_{n \geq 0} (\dim H_n(M)) t^n = (1 + t) \sum_{n \geq 0} Q_n t^n \quad (\text{A.2.2})$$

for some nonnegative integers Q_n . This gives $\#\{\lambda(p) = n\} \geq \dim H_n(M)$. This inequality can be shown for any homologies satisfying the Eilenberg–Steenrod axioms. Especially if all $Q_n = 0$, h is called a perfect Morse function.

Gradient flow and stable/unstable manifolds Let us still stick to the smooth compact Riemannian manifold M . Taking a local coordinate x^i , Morse’s downward flow equation is defined as

$$\frac{dx^i}{dt} = -g^{ij} \frac{\partial h}{\partial x^j}. \quad (\text{A.2.3})$$

There are two types of solutions in general; one is the constant solution at a critical point, $x(t) \equiv p$, and another one is a one-dimensional curve connecting two critical points. Let’s call this one-dimensional manifold as an “instanton”, because this is indeed an instanton of a supersymmetric quantum mechanics [149]. For each critical point p , we define the descending and ascending manifolds by

$$\mathcal{J}_p := \left\{ x(0) \in M \mid \lim_{t \rightarrow -\infty} x(t) = p \right\}, \quad \mathcal{K}_p := \left\{ x(0) \in M \mid \lim_{t \rightarrow +\infty} x(t) = p \right\}, \quad (\text{A.2.4})$$

respectively. The stable/unstable manifold theorem states that \mathcal{J}_p and \mathcal{K}_p are smooth manifolds, which are homeomorphic to open disks, and $\dim \mathcal{J}_p = \lambda(p)$ and $\dim \mathcal{K}_p = \dim(M) - \lambda(p)$.

The pair (h, g) of the Morse function and the metric is called **Morse–Smale** if \mathcal{J}_p and \mathcal{K}_q are transverse to each other for any $p, q \in \Sigma$: For any $r \in \mathcal{J}_p \cap \mathcal{K}_q$, $T_r \mathcal{J}_p \oplus T_r \mathcal{K}_q = T_r M$. This condition gives an exact sequence,

$$0 \rightarrow T_r(\mathcal{J}_p \cap \mathcal{K}_q) \rightarrow T_r(\mathcal{J}_p) \oplus T_r(\mathcal{K}_q) \rightarrow T_r M \rightarrow 0, \quad (\text{A.2.5})$$

for $r \in \mathcal{J}_p \cap \mathcal{K}_q$. This is a generic condition, in other words, small perturbations can always satisfy this even when a Morse function h is not Morse–Smale. We assume that (h, g) is Morse–Smale in the following.

Since $\dim(\mathcal{J}_p \cap \mathcal{K}_q) = \lambda(p) - \lambda(q)$ and

$$\mathcal{J}_p \cap \mathcal{K}_q = \{x(0) \mid x(-\infty) = p, x(+\infty) = q\}, \quad (\text{A.2.6})$$

the dimension of the moduli space of instantons is given by $\lambda(p) - \lambda(q)$. Therefore, if $\lambda(q) = \lambda(p) - 1$, the number of instantons connecting two critical points p and q is finite. The number of such instantons is precisely necessary information for computing homologies of M [149]. Consider the free \mathbb{Z} -module generated by descending manifolds \mathcal{J}_p graded by Morse indices,

$$C(M, h) = \bigoplus_n C_n(M, h), \quad C_n(M, h) = \sum_{p \in \Sigma, \lambda(p)=n} \mathbb{Z} \mathcal{J}_p. \quad (\text{A.2.7})$$

The boundary operator $\partial : C_n \rightarrow C_{n-1}$ is given by

$$\partial \mathcal{J}_p = \sum_{q \in \Sigma, \lambda(q)=\lambda(p)-1} n(p, q) \mathcal{J}_q, \quad (\text{A.2.8})$$

where $n(p, q)$ is a number of instantons connecting p and q . Here, an instanton is counted as ± 1 whether it preserves the orientation of the exact sequence (A.2.5) or not. One can check that $\partial^2 = 0$, and the homology of the complex $C(M, h)$ is nothing but $H_*(M)$. This also shows the strong Morse inequality.

Sketch of Witten's proof Let us recall the de Rham complex at first. Denoting the set of n -forms on M by $\Omega^n(M)$, the de Rham complex is

$$\Omega^* : \Omega^0(M) \xrightarrow{d} \Omega^1(M) \xrightarrow{d} \dots \xrightarrow{d} \Omega^{\dim(M)}(M). \quad (\text{A.2.9})$$

Cohomology of this complex is called the de Rham cohomology $H_{\text{dR}}^*(M)$, and the Poincaré duality states that $H_k(M) \simeq H_{\text{dR}}^{\dim(M)-k}(M)$ as \mathbb{R} -vector spaces. One can introduce an L^2 inner product on Ω^n by

$$\langle \alpha | \beta \rangle = \int_M \star \bar{\alpha} \wedge \beta, \quad (\text{A.2.10})$$

where \star is the Hodge star operator and $\bar{\alpha}$ is the complex conjugation of α . If degrees of α and β are different, we set $\langle \alpha | \beta \rangle = 0$. Let us regard Ω^* as a “Hilbert space” of quantum mechanics. As a “Hamiltonian”, we use the positive-definite operator

$$H_0 = dd^\dagger + d^\dagger d \left(= - \sum_n \frac{\partial^2}{(\partial x^n)^2} \right), \quad (\text{A.2.11})$$

where $\langle d^\dagger \alpha, \beta \rangle = \langle \alpha, d\beta \rangle$ (The last equality is true only on a flat local coordinate). This is nothing but the Laplace operator. The Hodge theory tells us that $H_{\text{dR}}^n(M)$ is nothing but the space of vacua of degree n , i.e., $H_{\text{dR}}^n(M) = \{\alpha \in \Omega^n \mid H_0 \alpha = 0\}$.

Instead of the exterior derivative d , one can consider another operator $d_t = e^{-th} d e^{th}$ for $t \geq 0$. Here h is a Morse function, and assume that (h, g) is Morse–Smale. Since this is just a conjugation, the de Rham cohomology is invariant for any t . Let us consider a Hamiltonian

$$H_t = d_t d_t^\dagger + d_t^\dagger d_t, \quad (\text{A.2.12})$$

then we would like to compute the space of vacua in order to obtain (co)homologies. In Ref. [149], the spectrum of H_t is computed in the limit $t \rightarrow \infty$ semiclassically.

Because of the anticommuting property of differential forms $dx^i \wedge dx^j = -dx^j \wedge dx^i$, the space of n -forms Ω^n can be regarded as the Hilbert space including n fermions, and $\alpha \mapsto dx^i \wedge \alpha$ gives the creation of i th fermion $\hat{c}^{i\dagger}$. The Hamiltonian H_t is expressed as

$$H_t = \sum_n (-\partial_n^2 + t^2 (\partial_n h)^2) + t \sum_{i,j} \frac{\partial^2 h}{\partial x^i \partial x^j} [\hat{c}^{i\dagger}, \hat{c}^j]. \quad (\text{A.2.13})$$

In the limit $t \rightarrow \infty$, low-energy wave functions must localize around critical points $p \in \Sigma$ because of the potential term $(\partial_n h)^2$. However, the bosonic part of Hamiltonians still have large energy due to zero-point oscillation. In order to cancel it, we need to make the fermionic energy maximally negative, and thus fermions must be occupied for negative eigenvalues of the Hessian of h and other fermions unoccupied. Let us denote this wave function by $|p\rangle$.

So far, by approximating the system as harmonic oscillators around critical points, we obtained the space of classical vacua $X^n(M, h)$ with n fermions, and $\dim X^n$ is the number of critical points p with Morse index $\lambda(p) = n$. Because of instantons (A.2.3), some elements of X^n may not be quantum vacua, which must be eliminated. The derivative $\delta : X^n \rightarrow X^{n+1}$,

$$\delta|p\rangle = \sum_{r \in \Sigma, \lambda(r)=\lambda(p)+1} n(r, p) |r\rangle, \quad (\text{A.2.14})$$

satisfies $\delta^2 = 0$. The cohomology of the complex (X^*, δ) gives the de Rham cohomology [149].

Appendix B

Path integral on Lefschetz thimbles and supersymmetry

Lefschetz thimbles can be interpreted as ground states of $\mathcal{N} = 2$ supersymmetric quantum systems [152–154] (see also Ref. [65]). It is possible to use this reformulation of the Lefschetz thimble in order to compute expectation values of observables. This work is taken from Ref. [155].

B.1 Lefschetz thimble and SUSY quantum mechanics.

Let us consider an N -dimensional real integral as a “quantum field theory” defined by a (complex) classical action $S(x)$. In this theory our goal is to compute an expectation value of an “observable” $\mathcal{O}(x)$ defined by

$$\langle \mathcal{O} \rangle = \mathcal{N} \int_{-\infty}^{\infty} d^N x e^{S(x)} \mathcal{O}(x), \quad (\text{B.1.1})$$

where $x = (x^{(1)}, x^{(2)}, \dots, x^{(N)}) \in \mathbb{R}^N$ and the normalization \mathcal{N} is chosen such that $\langle 1 \rangle = 1$. The starting point in our discussion is to reformulate this theory in an equivalent and more treatable way using a complexified representation:

$$\langle \mathcal{O} \rangle = \int d^N z d^N \bar{z} P(z, \bar{z}) \mathcal{O}(z). \quad (\text{B.1.2})$$

Here $z^{(i)} = x_1^{(i)} + ix_2^{(i)}$ and $\bar{z}^{(i)} = x_1^{(i)} - ix_2^{(i)}$ with $x_1^{(i)}, x_2^{(i)} \in \mathbb{R}$ and $\int dz d\bar{z}$ represents the integration over the whole complex plane; i.e. $\int_{-\infty}^{\infty} dx_1 \int_{-\infty}^{\infty} dx_2$. The choice of the generalized weight function $P(z, \bar{z})$ may not be unique. Indeed, a trivial example is $P(z, \bar{z}) = \mathcal{N} e^{S(z)} \prod_i \delta(z^{(i)} - \bar{z}^{(i)})$. At the cost of complexifying the variables, nevertheless, it is often the case that $P(z, \bar{z})$ could be endowed with more desirable properties for analytical and numerical computation than the original $e^{S(x)}$.

A clear criterion to simplify the integral is to find $P(z, \bar{z})$ such that the phase oscillation can be as much suppressed along integration paths as possible, while in the complex Langevin method $P(z, \bar{z})$ is optimized to become a real probability. To suppress the phase oscillation, let us pick up a saddle point z_σ satisfying $S'(z_\sigma) = 0$. The steepest descent cycle or the Lefschetz thimble \mathcal{J}_σ of the saddle point z_σ is defined with a fictitious time t as

$$\mathcal{J}_\sigma = \left\{ z(0) = x_1(0) + ix_2(0) \left| \frac{dx_j^{(i)}(t)}{dt} = -\frac{\partial \text{Re} S}{\partial x_j^{(i)}}, \lim_{t \rightarrow -\infty} (x_1(t) + ix_2(t)) = z_\sigma \right. \right\}. \quad (\text{B.1.3})$$

This is a multi-dimensional generalization of the steepest descent path in complex analysis, which we will refer to as the *downward* path. The original integration path on the real axis in Eq. (B.1.1) can be deformed as a sum of contributions on \mathcal{J}_σ weighted with an integer m_σ ; i.e., $\int_{\mathbb{R}^N} d^N x = \sum_\sigma m_\sigma \int_{\mathcal{J}_\sigma} d^N z$. In mathematics it is established how to determine m_σ from the intersection pattern between the steepest ascent (*upward*) path from z_σ and the original integration path [62, 64, 65]. It is important to note that $\text{Im}S$ is a constant on each Lefschetz thimble for the application to the sign problem [67, 70].

In the following, let us restrict ourselves to $N = 1$ for simplicity, because the generalization is straightforward. So far, the Lefschetz thimble is constructed as a line, and let us find a two-dimensional smooth distribution $P(z, \bar{z})$ according to Ref. [65]. For that purpose, we define the “delta-functional one-form” $\delta(\mathcal{J}_\sigma)$ supported on the Lefschetz thimble so that

$$\int_{\mathcal{J}_\sigma} \mathcal{O}(z) e^{S(z)} dz = \int_{\mathbb{C}} \delta(\mathcal{J}_\sigma) \wedge \mathcal{O}(z) e^{S(z)} dz. \quad (\text{B.1.4})$$

For instance, $\delta(\mathbb{R}) = \delta(y)dy$. Such delta-functional forms $\delta(\mathcal{J}_\sigma)$ (on a Kähler manifold) have a path-integral expression from the supersymmetric quantum mechanics [152–154] (see also Secs. 2.8 and 4 of Ref. [65] for more details in this context). Integration (B.1.4) can be represented as

$$\begin{aligned} \langle \mathcal{O} \rangle &= \mathcal{N} \int \mathcal{D}[x, p, \pi, \psi] \exp \left[i \int_{-\infty}^0 dt p_i \left(\frac{dx_i}{dt} + \frac{\partial \text{Re}S}{\partial x_i} \right) \right] \\ &\times \exp \left[- \int_{-\infty}^0 dt \pi_i \left(\frac{d}{dt} \delta_{ij} + \frac{\partial^2 \text{Re}S}{\partial x_i \partial x_j} \right) \psi_j \right] \mathcal{O}(z(0)) e^{S(z(0))} (\psi_1 + i\psi_2)(0). \end{aligned} \quad (\text{B.1.5})$$

Here x, p are bosonic fields and π, ψ are fermionic ghost fields, and $z(t) \rightarrow z_\sigma$ as $t \rightarrow -\infty$. We should note that an integration in terms of z is promoted to the path integral on $z(t)$ for $t \leq 0$, while the observable and the weight $\mathcal{O}(z(0)) \exp S(z(0))$ are functions of $z(0)$ only. Let us outline how these two expressions (B.1.4) and (B.1.5) are equivalent [65, 152–154]. We first integrate out $p(t)$ to get the Dirac delta function,

$$\int \mathcal{D}p \exp \left[i \int_{-\infty}^0 dt p_i \left(\frac{dx_i}{dt} + \frac{\partial \text{Re}S}{\partial x_i} \right) \right] = \delta \left(\frac{dx_i}{dt} + \frac{\partial \text{Re}S}{\partial x_i} \right). \quad (\text{B.1.6})$$

This delta function constrains the path integral on $x(t)$ to a gradient-flow line defining Lefschetz thimbles. Since $z(-\infty) \rightarrow z_\sigma$, this path integral for $t < 0$ gives a delta-functional support on \mathcal{J}_σ . However, the delta function produces an unwanted determinant factor. As is well-known, the path integral on ghost fields $\pi(t), \psi(t)$ for $t < 0$ can eliminate that factor as

$$\int \mathcal{D}\pi \mathcal{D}\psi \exp \left[- \int_{-\infty}^0 dt \pi_i \left(\frac{d}{dt} \delta_{ij} + \frac{\partial^2 \text{Re}S}{\partial x_i \partial x_j} \right) \psi_j \right] = \text{Det} \left(\frac{d}{dt} \delta_{ij} + \frac{\partial^2 \text{Re}S}{\partial x_i \partial x_j} \right). \quad (\text{B.1.7})$$

Now, we obtain an integration over surface variables $x(0), \psi(0)$, and denote them by x, ψ . Locally, the Lefschetz thimble \mathcal{J}_σ can be expressed as zeros of a certain function f , then we can find that the path integral (B.1.5) eventually gives

$$\int d^2x d^2\psi \delta(f) \frac{\partial f}{\partial x_i} \psi_i \wedge \mathcal{O}(z) e^{S(z)} (\psi_1 + i\psi_2) = \int \delta(f(x)) df(x) \wedge \mathcal{O}(z) e^{S(z)} dz, \quad (\text{B.1.8})$$

which is nothing but the local expression of the original integration (B.1.4). Going back to (B.1.5), this shows that the so-called residual sign problem comes from the fermionic surface term $\psi_1(0) + i\psi_2(0)$ because one can identify $\psi_i(0) = dx_i$ as above.

B.2 Hamilton dynamics

Importantly, with these added fields, p_i, π_i, ψ_i , the action is BRST exact under a transformation; $\hat{\delta}x_i = \psi_i, \hat{\delta}\psi_i = 0, \hat{\delta}\pi_i = -ip_i, \hat{\delta}p_i = 0$ [65]. By definition the nilpotency $\hat{\delta}^2 = 0$ is obvious. Thanks to the boundary fermionic operator in (B.1.5), the surface term is BRST-closed so long as the observables are holomorphic. This makes a sharp contrast to the complex Langevin method that could also acquire the BRST symmetry but it is violated by the surface term. Because of the BRST symmetry we can add any BRST exact terms without changing the original integral, and it is useful to insert $\frac{\varepsilon_i}{2} \int dt p_i^2$. In summary, the effective Lagrangian that describes the fictitious time evolution is given by the following topological theory:

$$\begin{aligned} L_{\text{eff}} &= -\frac{\varepsilon_i}{2} p_i^2 + ip_i \left(\frac{dx_i}{dt} + \frac{\partial \text{Re}S}{\partial x_i} \right) + \pi_i \left(\frac{d}{dt} \delta_{ij} + \frac{\partial^2 \text{Re}S}{\partial x_i \partial x_j} \right) \psi_j \\ &= -\hat{\delta} \left\{ \pi_i \left(i \frac{\varepsilon_i}{2} p_i + \frac{dx_i}{dt} + \frac{\partial \text{Re}S}{\partial x_i} \right) \right\}, \end{aligned} \quad (\text{B.2.1})$$

which is nothing but a Legendre transform of an effective Hamiltonian:

$$H_{\text{eff}} = \sum_i \left[\frac{\varepsilon_i}{2} \hat{p}_i^2 - \frac{i}{2} \left(\frac{\partial \text{Re}S}{\partial x_i} \hat{p}_i + \hat{p}_i \frac{\partial \text{Re}S}{\partial x_i} \right) \right] - \sum_{i,j} \frac{1}{2} \frac{\partial^2 \text{Re}S}{\partial x_i \partial x_j} [\hat{\pi}_i, \hat{\psi}_j] \quad (\text{B.2.2})$$

with $[x_i, \hat{p}_j] = i\delta_{ij}$ and $\{\hat{\pi}_i, \hat{\psi}_j\} = \delta_{ij}$. The fermion number $F = \hat{\pi}_1 \hat{\psi}_1 + \hat{\pi}_2 \hat{\psi}_2$ is a conserved quantity of this Hamiltonian. After the time evolution from $t = -\infty$ only the ground state with the lowest energy eigenvalue remains, so that the generalized weight is given by $P(z, \bar{z}) dz d\bar{z} = \Psi(z, \bar{z}) \wedge e^{S(z)} dz$, where $\Psi(z, \bar{z})$ is the ground state wave-function and converges to $\delta(\mathcal{J}_\sigma)$ in the limit $\varepsilon_i \rightarrow +0$. Note that the weight factor $\exp S(z)$ is necessary in this formula, since the wave function designates only the integration cycle \mathcal{J}_σ . We can further simplify this Hamilton problem by choosing $\varepsilon = \varepsilon_1 = \varepsilon_2$. Performing the conjugate transformation $\Psi = e^{-\text{Re}S/\varepsilon} \Psi'$, the first derivative terms are eliminated as

$$H'_{\text{eff}} = \sum_i \left[\frac{\varepsilon}{2} \hat{p}_i^2 + \frac{1}{2\varepsilon} \left(\frac{\partial \text{Re}S}{\partial x_i} \right)^2 \right] - \sum_{i,j} \frac{1}{2} \frac{\partial^2 \text{Re}S}{\partial x_i \partial x_j} [\hat{\pi}_i, \hat{\psi}_j]. \quad (\text{B.2.3})$$

This describes supersymmetric quantum mechanics with the superpotential $\text{Re}S$ [65].

By restricting ourselves to the $F = 1$ sector, we can define the effective potential in a form of 2×2 matrix-valued function that amounts to

$$V_{\text{eff}} = \frac{1}{2\varepsilon} \left[\left(\frac{\partial \text{Re}S}{\partial x_1} \right)^2 + \left(\frac{\partial \text{Re}S}{\partial x_2} \right)^2 \right] - \begin{pmatrix} \partial^2 \text{Re}S / \partial x_1^2 & \partial^2 \text{Re}S / \partial x_1 \partial x_2 \\ \partial^2 \text{Re}S / \partial x_1 \partial x_2 & -\partial^2 \text{Re}S / \partial x_1^2 \end{pmatrix}, \quad (\text{B.2.4})$$

and then the Hamiltonian is

$$H'_{\text{eff}} = -\frac{\varepsilon}{2} \left(\frac{\partial^2}{\partial x_1^2} + \frac{\partial^2}{\partial x_2^2} \right) + V_{\text{eff}}. \quad (\text{B.2.5})$$

This reformulation provides one way to compute Lefschetz thimbles for numerical purpose by solving the ground state of the above H'_{eff} at some ε [155].

References

- [1] R. P. Feynman, “Space-time approach to nonrelativistic quantum mechanics,” *Rev.Mod.Phys.* **20** (1948) 367–387.
- [2] R. P. Feynman and A. R. Hibbs, *Quantum Mechanics and Path Integrals*. McGraw-Hill Companies, first ed., 1965.
- [3] T. Matsubara, “A New approach to quantum statistical mechanics,” *Prog. Theor. Phys.* **14** (1955) 351–378.
- [4] F. Karsch, “Lattice QCD at high temperature and density,” *Lect. Notes Phys.* **583** (2002) 209–249, [arXiv:hep-lat/0106019 \[hep-lat\]](#).
- [5] D. M. Ceperley, “Path integrals in the theory of condensed helium,” *Rev. Mod. Phys.* **67** (1995) 279–355.
- [6] L. Pollet, “Recent developments in quantum Monte Carlo simulations with applications for cold gases,” *Rep. Prog. Phys.* **75** (2012) 094501, [arXiv:1206.0781 \[cond-mat.quant-gas\]](#).
- [7] A. Yamamoto and T. Hatsuda, “Quantum Monte Carlo simulation of three-dimensional Bose-Fermi mixtures,” *Phys. Rev. A* **86** (2012) 043627, [arXiv:1209.1954 \[cond-mat.quant-gas\]](#).
- [8] S. Weinberg, *The Quantum Theory of Fields, Volume 2: Modern Applications*. Cambridge University Press, 5, 2005.
- [9] T. Muta, *Foundations of Quantum Chromodynamics: An Introduction to Perturbative Methods in Gauge Theories (World Scientific Lecture Notes in Physics)*. Wsps, 6, 1984.
- [10] J. I. Kapusta and C. Gale, *Finite-Temperature Field Theory: Principles and Applications (Cambridge Monographs on Mathematical Physics)*. Cambridge University Press, 2 ed., 2, 2011.
- [11] K. Yagi, T. Hatsuda, and P. Y. Miake, *Quark-Gluon Plasma: From Big Bang to Little Bang (Cambridge Monographs on Particle Physics, Nuclear Physics and Cosmology)*. Cambridge University Press, 1 ed., 10, 2008.
- [12] D. J. Gross and F. Wilczek, “Asymptotically Free Gauge Theories. 1,” *Phys. Rev.* **D8** (1973) 3633–3652.
- [13] D. J. Gross and F. Wilczek, “Asymptotically Free Gauge Theories. 2,” *Phys. Rev.* **D9** (1974) 980–993.

- [14] H. D. Politzer, “Reliable Perturbative Results for Strong Interactions?,” *Phys. Rev. Lett.* **30** (1973) 1346–1349.
- [15] S. Bethke, “World Summary of α_s (2012),” [arXiv:1210.0325 \[hep-ex\]](#). [Nucl. Phys. Proc. Suppl.234,229(2013)].
- [16] **Particle Data Group** Collaboration, K. A. Olive *et al.*, “Review of Particle Physics,” *Chin. Phys.* **C38** (2014) 090001.
- [17] E. D. Bloom, D. H. Coward, H. DeStaebler, J. Drees, G. Miller, L. W. Mo, R. E. Taylor, M. Breidenbach, J. I. Friedman, G. C. Hartmann, and H. W. Kendall, “High-Energy Inelastic e-p Scattering at 6° and 10°,” *Phys. Rev. Lett.* **23** (1969) 930–934.
- [18] M. Breidenbach, J. I. Friedman, H. W. Kendall, E. D. Bloom, D. H. Coward, H. DeStaebler, J. Drees, L. W. Mo, and R. E. Taylor, “Observed Behavior of Highly Inelastic Electron-Proton Scattering,” *Phys. Rev. Lett.* **23** (1969) 935–939.
- [19] K. G. Wilson, “Confinement of Quarks,” *Phys. Rev.* **D10** (1974) 2445–2459.
- [20] M. Creutz, “Confinement and the Critical Dimensionality of Space-Time,” *Phys. Rev. Lett.* **43** (1979) 553–556. [Erratum: *Phys. Rev. Lett.*43,890(1979)].
- [21] M. Creutz, L. Jacobs, and C. Rebbi, “Experiments with a Gauge Invariant Ising System,” *Phys. Rev. Lett.* **42** (1979) 1390.
- [22] M. Creutz, “Monte Carlo Study of Quantized SU(2) Gauge Theory,” *Phys. Rev.* **D21** (1980) 2308–2315.
- [23] A. M. Polyakov, “Compact Gauge Fields and the Infrared Catastrophe,” *Phys. Lett.* **B59** (1975) 82–84.
- [24] A. M. Polyakov, “Thermal Properties of Gauge Fields and Quark Liberation,” *Phys.Lett.* **B72** (1978) 477–480.
- [25] G. ’t Hooft, “On the Phase Transition Towards Permanent Quark Confinement,” *Nucl. Phys.* **B138** (1978) 1.
- [26] G. ’t Hooft, “A Property of Electric and Magnetic Flux in Nonabelian Gauge Theories,” *Nucl. Phys.* **B153** (1979) 141.
- [27] G. ’t Hooft, “Topology of the Gauge Condition and New Confinement Phases in Nonabelian Gauge Theories,” *Nucl. Phys.* **B190** (1981) 455.
- [28] A. M. Polyakov, *Gauge Fields and Strings*, vol. 3. 1987.
- [29] N. Seiberg and E. Witten, “Electric - magnetic duality, monopole condensation, and confinement in N=2 supersymmetric Yang-Mills theory,” *Nucl.Phys.* **B426** (1994) 19–52, [arXiv:hep-th/9407087 \[hep-th\]](#).
- [30] N. Seiberg and E. Witten, “Monopoles, duality and chiral symmetry breaking in N=2 supersymmetric QCD,” *Nucl.Phys.* **B431** (1994) 484–550, [arXiv:hep-th/9408099 \[hep-th\]](#).

- [31] T. Schäfer and E. V. Shuryak, “Instantons in QCD,” *Rev. Mod. Phys.* **70** (1998) 323–426, [arXiv:hep-ph/9610451 \[hep-ph\]](#).
- [32] M. Unsal, “Magnetic bion condensation: A New mechanism of confinement and mass gap in four dimensions,” *Phys. Rev. D* **80** (2009) 065001, [arXiv:0709.3269 \[hep-th\]](#).
- [33] M. Unsal, “Abelian duality, confinement, and chiral symmetry breaking in QCD(adj),” *Phys. Rev. Lett.* **100** (2008) 032005, [arXiv:0708.1772 \[hep-th\]](#).
- [34] G. V. Dunne and M. Ünsal, “Continuity and Resurgence: towards a continuum definition of the $\mathbb{CP}(N-1)$ model,” *Phys. Rev. D* **87** (2013) 025015, [arXiv:1210.3646 \[hep-th\]](#).
- [35] G. V. Dunne and M. Ünsal, “Resurgence and Trans-series in Quantum Field Theory: The $\mathbb{CP}(N-1)$ Model,” *JHEP* **1211** (2012) 170, [arXiv:1210.2423 \[hep-th\]](#).
- [36] G. V. Dunne and M. Ünsal, “Uniform WKB, Multi-instantons, and Resurgent Trans-Series,” *Phys. Rev. D* **89** (2014) 105009, [arXiv:1401.5202 \[hep-th\]](#).
- [37] G. V. Dunne and M. Ünsal, “Generating nonperturbative physics from perturbation theory,” *Phys. Rev. D* **89** no. 4, (2014) 041701, [arXiv:1306.4405 \[hep-th\]](#).
- [38] P. C. Argyres and M. Ünsal, “The semi-classical expansion and resurgence in gauge theories: new perturbative, instanton, bion, and renormalon effects,” *JHEP* **08** (2012) 063, [arXiv:1206.1890 \[hep-th\]](#).
- [39] P. Argyres and M. Ünsal, “A semiclassical realization of infrared renormalons,” *Phys. Rev. Lett.* **109** (2012) 121601, [arXiv:1204.1661 \[hep-th\]](#).
- [40] A. Cherman, D. Dorigoni, and M. Unsal, “Decoding perturbation theory using resurgence: Stokes phenomena, new saddle points and Lefschetz thimbles,” [arXiv:1403.1277 \[hep-th\]](#).
- [41] A. Cherman, D. Dorigoni, G. V. Dunne, and M. Unsal, “Resurgence in Quantum Field Theory: Nonperturbative Effects in the Principal Chiral Model,” *Phys. Rev. Lett.* **112** no. 2, (2014) 021601, [arXiv:1308.0127 \[hep-th\]](#).
- [42] E. Shuryak and T. Sulejmanpasic, “Holonomy potential and confinement from a simple model of the gauge topology,” *Phys. Lett. B* **726** (2013) 257–261, [arXiv:1305.0796 \[hep-ph\]](#).
- [43] E. Poppitz and T. Sulejmanpasic, “(S)QCD on $\mathbb{R}^3 \times \mathbb{S}^1$: Screening of Polyakov loop by fundamental quarks and the demise of semi-classics,” *JHEP* **09** (2013) 128, [arXiv:1307.1317 \[hep-th\]](#).
- [44] R. Larsen and E. Shuryak, “Interacting ensemble of the instanton-dyons and the deconfinement phase transition in the $SU(2)$ gauge theory,” *Phys. Rev. D* **92** no. 9, (2015) 094022, [arXiv:1504.03341 \[hep-ph\]](#).
- [45] Y. Nambu and G. Jona-Lasinio, “Dynamical Model of Elementary Particles Based on an Analogy with Superconductivity. I,” *Phys. Rev.* **122** (1961) 345–358.

- [46] Y. Nambu and G. Jona-Lasinio, “Dynamical Model of Elementary Particles Based on an Analogy with Superconductivity. II,” *Phys.Rev.* **124** (1961) 246–254.
- [47] J. C. Collins and M. J. Perry, “Superdense Matter: Neutrons Or Asymptotically Free Quarks?,” *Phys. Rev. Lett.* **34** (1975) 1353.
- [48] N. Cabibbo and G. Parisi, “Exponential Hadronic Spectrum and Quark Liberation,” *Phys. Lett.* **B59** (1975) 67–69.
- [49] R. Hagedorn, “Statistical thermodynamics of strong interactions at high-energies,” *Nuovo Cim. Suppl.* **3** (1965) 147–186.
- [50] K. Fukushima and T. Hatsuda, “The phase diagram of dense QCD,” *Rep. Prog. Phys.* **74** (2011) 014001, [arXiv:1005.4814 \[hep-ph\]](#).
- [51] Y. Aoki, G. Endrodi, Z. Fodor, S. D. Katz, and K. K. Szabo, “The Order of the quantum chromodynamics transition predicted by the standard model of particle physics,” *Nature* **443** (2006) 675–678, [arXiv:hep-lat/0611014 \[hep-lat\]](#).
- [52] C. DeTar and U. M. Heller, “QCD Thermodynamics from the Lattice,” *Eur. Phys. J.* **A41** (2009) 405–437, [arXiv:0905.2949 \[hep-lat\]](#).
- [53] M. I. Buchoff, M. Cheng, N. H. Christ, H. T. Ding, C. Jung, F. Karsch, Z. Lin, R. Mawhinney, M. Swagato, P. Petreczky, D. Renfrew, C. Schroeder, P. Vranas, and H. Yin, “QCD chiral transition, U(1)A symmetry and the dirac spectrum using domain wall fermions,” *Phys. Rev.* **D89** no. 5, (2014) 054514, [arXiv:1309.4149 \[hep-lat\]](#).
- [54] P. Braun-Munzinger, B. Friman, and J. Stachel, eds., *QUARK MATTER 2014, XXIV INTERNATIONAL CONFERENCE ON ULTRARELATIVISTIC NUCLEUS-NUCLEUS COLLISIONS*, vol. 931 of *Nuclear Physics A*. 2014.
- [55] K. Hebeler, J. M. Lattimer, C. J. Pethick, and A. Schwenk, “Equation of state and neutron star properties constrained by nuclear physics and observation,” *Astrophys. J.* **773** (2013) 11, [arXiv:1303.4662 \[astro-ph.SR\]](#).
- [56] S. Muroya, A. Nakamura, C. Nonaka, and T. Takaishi, “Lattice QCD at finite density: An Introductory review,” *Prog. Theor. Phys.* **110** (2003) 615–668, [arXiv:hep-lat/0306031 \[hep-lat\]](#).
- [57] E. Loh, J. Gubernatis, R. Scalettar, S. White, D. Scalapino, and R. Sugar, “Sign problem in the numerical simulation of many-electron systems,” *Phys. Rev. B* **41** (1990) 9301–9307.
- [58] T. D. Cohen, “Functional integrals for QCD at nonzero chemical potential and zero density,” *Phys. Rev. Lett.* **91** (2003) 222001, [arXiv:hep-ph/0307089 \[hep-ph\]](#).
- [59] A. C. Doyle, *Silver Blaze*. 1892.
- [60] Y. Hidaka and N. Yamamoto, “No-Go Theorem for Critical Phenomena in Large-Nc QCD,” *Phys. Rev. Lett.* **108** (2012) 121601, [arXiv:1110.3044 \[hep-ph\]](#).

- [61] M. Hanada, Y. Matsuo, and N. Yamamoto, “Sign problem and phase quenching in finite-density QCD: models, holography, and lattice,” *Phys. Rev. D* **86** (2012) 074510, [arXiv:1205.1030 \[hep-lat\]](#).
- [62] F. Pham, “Vanishing homologies and the n variable saddlepoint method,” in *Proc. Symp. Pure Math*, vol. 40.2, pp. 319–333. AMS, 1983.
- [63] V. Arnold, A. Varchenko, and S. Gusein-Zade, *Singularities of Differentiable Maps: Volume II Monodromy and Asymptotic Integrals (Monographs in Mathematics)*. Springer, 1988.
- [64] E. Witten, “Analytic Continuation Of Chern-Simons Theory,” in *Chern-Simons Gauge Theory: 20 Years After*, vol. 50, pp. 347–446. AMS/IP Stud. Adv. Math., 2010. [arXiv:1001.2933 \[hep-th\]](#).
- [65] E. Witten, “A New Look At The Path Integral Of Quantum Mechanics,” [arXiv:1009.6032 \[hep-th\]](#).
- [66] D. Harlow, J. Maltz, and E. Witten, “Analytic Continuation of Liouville Theory,” *JHEP* **1112** (2011) 071, [arXiv:1108.4417 \[hep-th\]](#).
- [67] **AuroraScience** Collaboration, M. Cristoforetti, F. Di Renzo, and L. Scorzato, “New approach to the sign problem in quantum field theories: High density QCD on a Lefschetz thimble,” *Phys. Rev. D* **86** (2012) 074506, [arXiv:1205.3996 \[hep-lat\]](#).
- [68] M. Cristoforetti, F. Di Renzo, A. Mukherjee, and L. Scorzato, “Monte Carlo simulations on the Lefschetz thimble: taming the sign problem,” *Phys. Rev. D* **88** (2013) 051501, [arXiv:1303.7204 \[hep-lat\]](#).
- [69] M. Cristoforetti, F. Di Renzo, G. Eruzzi, A. Mukherjee, C. Schmidt, L. Scorzato, and C. Torrero, “An efficient method to compute the residual phase on a Lefschetz thimble,” *Phys. Rev. D* **89** (2014) 114505, [arXiv:1403.5637 \[hep-lat\]](#).
- [70] H. Fujii, D. Honda, M. Kato, Y. Kikukawa, S. Komatsu, and T. Sano, “Hybrid Monte Carlo on Lefschetz thimbles - A study of the residual sign problem,” *JHEP* **1310** (2013) 147, [arXiv:1309.4371 \[hep-lat\]](#).
- [71] G. Aarts, “Lefschetz thimbles and stochastic quantisation: Complex actions in the complex plane,” *Phys. Rev. D* **88** (2013) 094501, [arXiv:1308.4811 \[hep-lat\]](#).
- [72] G. Aarts, L. Bongiovanni, E. Seiler, and D. Sexty, “Some remarks on Lefschetz thimbles and complex Langevin dynamics,” *JHEP* **1410** (2014) 159, [arXiv:1407.2090 \[hep-lat\]](#).
- [73] F. Di Renzo and G. Eruzzi, “Thimble regularization at work: from toy models to chiral random matrix theories,” *Phys. Rev. D* **92** (2015) 085030, [arXiv:1507.03858 \[hep-lat\]](#).
- [74] J. Écalle, “Les fonctions résurgentes. Tome I.”
- [75] D. Dorigoni, “An Introduction to Resurgence, Trans-Series and Alien Calculus,” [arXiv:1411.3585 \[hep-th\]](#).

- [76] Y. Tanizaki and T. Koike, “Real-time Feynman path integral with Picard–Lefschetz theory and its applications to quantum tunneling,” *Ann. Phys.* **351** (2014) 250, [arXiv:1406.2386 \[math-ph\]](#).
- [77] M. Kac, “On Some Connections between Probability Theory and Differential and Integral Equations,” in *Proceedings of the Second Berkeley Symposium on Mathematical Statistics and Probability*, pp. 189–215. University of California Press, Berkeley, Calif., 1951. <http://projecteuclid.org/euclid.bsmsp/1200500229>.
- [78] E. Nelson, “Feynman Integrals and the Schrödinger Equation,” *Journal of Mathematical Physics* **5** no. 3, (1964) 332–343.
- [79] B. Simon, *Functional Integration and Quantum Physics*, vol. 86. Academic press, 1979.
- [80] V. Arnold, *Mathematical Methods of Classical Mechanics*. Graduate Texts in Mathematics Vol.60. Springer, 2nd ed., 1989. translated by K. Vogtmann and A. Weinstein.
- [81] S. Coleman, “Fate of the false vacuum: Semiclassical theory,” *Phys. Rev. D* **15** (1977) 2929–2936.
- [82] I. Y. Kobzarev, L. B. Okun, and M. B. Voloshin, “Bubbles in metastable vacuum,” *Sov. J. Nucl. Phys* **20** (1975) 644.
- [83] F. W. Olver, D. M. Lozier, R. F. Boisvert, and C. W. Clark, eds., *Digital Library of Mathematical Functions: Online Companion to NIST Handbook of Mathematical Functions (CUP)*. National Institute of Standards and Technology, 2010. <http://dlmf.nist.gov>.
- [84] F. R. Klinkhamer and N. S. Manton, “A saddle-point solution in the weinberg-salam theory,” *Phys. Rev. D* **30** (1984) 2212–2220.
- [85] P. Arnold and L. McLerran, “Sphalerons, small fluctuations, and baryon-number violation in electroweak theory,” *Phys. Rev. D* **36** (1987) 581–595.
- [86] P. Arnold and L. McLerran, “The sphaleron strikes back: A response to objections to the sphaleron approximation,” *Phys. Rev. D* **37** (1988) 1020–1029.
- [87] A. Cherman and M. Unsal, “Real-Time Feynman Path Integral Realization of Instantons,” [arXiv:1408.0012 \[hep-th\]](#).
- [88] C. K. Dumlu and G. V. Dunne, “The Stokes Phenomenon and Schwinger Vacuum Pair Production in Time-Dependent Laser Pulses,” *Phys. Rev. Lett.* **104** (2010) 250402, [arXiv:1004.2509 \[hep-th\]](#).
- [89] C. K. Dumlu and G. V. Dunne, “Interference Effects in Schwinger Vacuum Pair Production for Time-Dependent Laser Pulses,” *Phys. Rev. D* **83** (2011) 065028, [arXiv:1102.2899 \[hep-th\]](#).
- [90] C. K. Dumlu and G. V. Dunne, “Complex Worldline Instantons and Quantum Interference in Vacuum Pair Production,” *Phys. Rev. D* **84** (2011) 125023, [arXiv:1110.1657 \[hep-th\]](#).

- [91] T. Kanazawa and Y. Tanizaki, “Structure of Lefschetz thimbles in simple fermionic systems,” *JHEP* **1503** (2015) 044, [arXiv:1412.2802 \[hep-th\]](#).
- [92] D. J. Gross and A. Neveu, “Dynamical Symmetry Breaking in Asymptotically Free Field Theories,” *Phys.Rev.* **D10** (1974) 3235.
- [93] M. V. Berry, “Stokes’ phenomenon; smoothing a victorian discontinuity,” *Publ.Math.of the Institut des Hautes Etudes scientifique* **68** (1989) 211.
- [94] D. Boer and J. K. Boomsma, “Spontaneous CP-violation in the strong interaction at $\theta = \pi$,” *Phys.Rev.* **D78** (2008) 054027, [arXiv:0806.1669 \[hep-ph\]](#).
- [95] J. K. Boomsma and D. Boer, “The High temperature CP-restoring phase transition at $\theta = \pi$,” *Phys.Rev.* **D80** (2009) 034019, [arXiv:0905.4660 \[hep-ph\]](#).
- [96] M. V. Berry, “Uniform asymptotic smoothing of stokes’s discontinuities,” *Proc. Roy. Soc. Lond. A* **422** (1989) 7–21.
- [97] C. N. Yang and T. D. Lee, “Statistical Theory of Equations of State and Phase Transitions. I. Theory of Condensation,” *Phys. Rev.* **87** (1952) 404–409.
- [98] T. D. Lee and C. N. Yang, “Statistical Theory of Equations of State and Phase Transitions. II. Lattice Gas and Ising Model,” *Phys. Rev.* **87** (1952) 410–419.
- [99] I. Bena, M. Droz, and A. Lipowski, “Statistical mechanics of equilibrium and nonequilibrium phase transitions: The yang-lee formalism,” *International Journal of Modern physics B* **19** (2005) 4269–4329, [cond-mat/0510278](#).
- [100] Z. Fodor and S. Katz, “Lattice determination of the critical point of QCD at finite T and μ ,” *JHEP* **0203** (2002) 014, [arXiv:hep-lat/0106002 \[hep-lat\]](#).
- [101] Z. Fodor and S. Katz, “Critical point of QCD at finite T and μ , lattice results for physical quark masses,” *JHEP* **0404** (2004) 050, [arXiv:hep-lat/0402006 \[hep-lat\]](#).
- [102] S. Ejiri, “Lee-Yang zero analysis for the study of QCD phase structure,” *Phys.Rev.* **D73** (2006) 054502, [arXiv:hep-lat/0506023 \[hep-lat\]](#).
- [103] M. Stephanov, “QCD critical point and complex chemical potential singularities,” *Phys.Rev.* **D73** (2006) 094508, [arXiv:hep-lat/0603014 \[hep-lat\]](#).
- [104] S. Kratochvila and P. de Forcrand, “QCD at zero baryon density and the Polyakov loop paradox,” *Phys. Rev. D* **73** (2006) 114512, [arXiv:hep-lat/0602005 \[hep-lat\]](#).
- [105] A. Denbleyker, D. Du, Y. Liu, Y. Meurice, and H. Zou, “Fisher’s zeros as boundary of renormalization group flows in complex coupling spaces,” *Phys.Rev.Lett.* **104** (2010) 251601, [arXiv:1005.1993 \[hep-lat\]](#).
- [106] **XQCD-J** Collaboration, K. Nagata, S. Motoki, Y. Nakagawa, A. Nakamura, and T. Saito, “Towards extremely dense matter on the lattice,” *Prog. Theor. Exp. Phys.* **2012** (2012) 01A103, [arXiv:1204.1412 \[hep-lat\]](#).

- [107] K. Nagata, K. Kashiwa, A. Nakamura, and S. M. Nishigaki, “Lee-Yang zero distribution of high temperature QCD and the Roberge-Weiss phase transition,” *Phys. Rev. D* **91** (2015) 094507, [arXiv:1410.0783 \[hep-lat\]](#).
- [108] Y. Tanizaki, “Lefschetz-thimble techniques for path integral of zero-dimensional $O(n)$ sigma models,” *Phys. Rev. D* **91** (2015) 036002, [arXiv:1412.1891 \[hep-th\]](#).
- [109] Y. Tanizaki, H. Nishimura, and K. Kashiwa, “Evading the sign problem in the mean-field approximation through Lefschetz-thimble path integral,” *Phys. Rev. D* **91** (2015) 101701, [arXiv:1504.02979 \[hep-th\]](#).
- [110] M. Unsal, “Theta dependence, sign problems and topological interference,” *Phys. Rev. D* **86** (2012) 105012, [arXiv:1201.6426 \[hep-th\]](#).
- [111] G. Basar, G. V. Dunne, and M. Unsal, “Resurgence theory, ghost-instantons, and analytic continuation of path integrals,” *JHEP* **1310** (2013) 041, [arXiv:1308.1108 \[hep-th\]](#).
- [112] R. Larsen and E. Shuryak, “Classical interactions of the instanton-dyons with antidyons,” [arXiv:1408.6563 \[hep-ph\]](#).
- [113] A. Dumitru, R. D. Pisarski, and D. Zschiesche, “Dense quarks, and the fermion sign problem, in a $SU(N)$ matrix model,” *Phys. Rev. D* **72** (2005) 065008, [arXiv:hep-ph/0505256 \[hep-ph\]](#).
- [114] K. Fukushima and Y. Hidaka, “A Model study of the sign problem in the mean-field approximation,” *Phys. Rev. D* **75** (2007) 036002, [arXiv:hep-ph/0610323 \[hep-ph\]](#).
- [115] H. Nishimura, M. C. Ogilvie, and K. Pangeni, “Complex saddle points in QCD at finite temperature and density,” *Phys. Rev. D* **90** (2014) 045039, [arXiv:1401.7982 \[hep-ph\]](#).
- [116] H. Nishimura, M. C. Ogilvie, and K. Pangeni, “Complex Saddle Points and Disorder Lines in QCD at finite temperature and density,” *Phys. Rev. D* **91** no. 5, (2015) 054004, [arXiv:1411.4959 \[hep-ph\]](#).
- [117] A. Mukherjee and M. Cristoforetti, “Lefschetz thimble Monte Carlo for many body theories: application to the repulsive Hubbard model away from half filling,” *Phys. Rev. B* **90** (2014) 035134, [arXiv:1403.5680 \[cond-mat.str-el\]](#).
- [118] C. Korthals Altes, “Constrained effective potential in hot QCD,” *Nucl. Phys.* **B420** (1994) 637–668, [arXiv:hep-th/9310195 \[hep-th\]](#).
- [119] R. Fukuda and E. Kyriakopoulos, “Derivation of the Effective Potential,” *Nucl. Phys.* **B85** (1975) 354.
- [120] F. Green and F. Karsch, “Mean Field Analysis of $SU(N)$ Deconfining Transitions in the Presence of Dynamical Quarks,” *Nucl.Phys.* **B238** (1984) 297.
- [121] P. N. Meisinger, T. R. Miller, and M. C. Ogilvie, “Phenomenological equations of state for the quark gluon plasma,” *Phys. Rev. D* **65** (2002) 034009, [arXiv:hep-ph/0108009 \[hep-ph\]](#).

- [122] C. Alexandrou, A. Borici, A. Feo, P. de Forcrand, A. Galli, F. Jegerlehner, and T. Takaishi, “The Deconfinement phase transition in one flavor QCD,” *Phys. Rev. D* **60** (1999) 034504, [arXiv:hep-lat/9811028 \[hep-lat\]](#).
- [123] J. Condella and C. E. Detar, “Potts flux tube model at nonzero chemical potential,” *Phys. Rev. D* **61** (2000) 074023, [arXiv:hep-lat/9910028 \[hep-lat\]](#).
- [124] M. G. Alford, S. Chandrasekharan, J. Cox, and U. Wiese, “Solution of the complex action problem in the Potts model for dense QCD,” *Nucl. Phys.* **B602** (2001) 61–86, [arXiv:hep-lat/0101012 \[hep-lat\]](#).
- [125] T. Banks and A. Ukawa, “Deconfining and Chiral Phase Transitions in Quantum Chromodynamics at Finite Temperature,” *Nucl. Phys.* **B225** (1983) 145.
- [126] R. D. Pisarski, “Quark gluon plasma as a condensate of SU(3) Wilson lines,” *Phys. Rev. D* **62** (2000) 111501, [arXiv:hep-ph/0006205 \[hep-ph\]](#).
- [127] A. Dumitru and R. D. Pisarski, “Event-by-event fluctuations from decay of a Polyakov loop condensate,” *Phys.Lett.* **B504** (2001) 282–290, [arXiv:hep-ph/0010083 \[hep-ph\]](#).
- [128] Y. Tanizaki, Y. Hidaka, and T. Hayata, “Lefschetz-thimble analysis of the sign problem in one-site fermion model,” [arXiv:1509.07146 \[hep-th\]](#).
- [129] J. Hubbard, “Electron Correlations in Narrow Energy Bands,” *Proc. R. Soc. Lond. A* **276** (1963) 238–257.
- [130] M. C. Gutzwiller, “Effect of Correlation on the Ferromagnetism of Transition Metals,” *Phys. Rev. Lett.* **10** (1963) 159–162.
- [131] J. Kanamori, “Electron Correlation and Ferromagnetism of Transition Metals,” *Prog. Theor. Phys.* **30** (1963) 275–289.
- [132] H. Fujii, S. Kamata, and Y. Kikukawa, “Lefschetz thimble structure in one-dimensional lattice Thirring model at finite density,” [arXiv:1509.08176 \[hep-lat\]](#).
- [133] H. Fujii, S. Kamata, and Y. Kikukawa, “Monte Carlo study of Lefschetz thimble structure in one-dimensional Thirring model at finite density,” [arXiv:1509.09141 \[hep-lat\]](#).
- [134] A. Alexandru, G. Basar, and P. Bedaque, “A Monte Carlo algorithm for simulating fermions on Lefschetz thimbles,” [arXiv:1510.03258 \[hep-lat\]](#).
- [135] I. M. Barbour, S. E. Morrison, E. G. Klepfish, J. B. Kogut, and M.-P. Lombardo, “The Critical points of strongly coupled lattice QCD at nonzero chemical potential,” *Phys. Rev. D* **56** (1997) 7063–7072, [arXiv:hep-lat/9705038 \[hep-lat\]](#).
- [136] I. M. Barbour, S. E. Morrison, E. G. Klepfish, J. B. Kogut, and M.-P. Lombardo, “Results on finite density QCD,” *Nucl. Phys. Proc. Suppl.* **60A** (1998) 220–234, [arXiv:hep-lat/9705042 \[hep-lat\]](#).

- [137] D. H. Adams, “A Dimensionally reduced expression for the QCD fermion determinant at finite temperature and chemical potential,” *Phys. Rev. D* **70** (2004) 045002, [arXiv:hep-th/0401132 \[hep-th\]](#).
- [138] T. Hayata, Y. Hidaka, and Y. Tanizaki, “Complex saddle points and the sign problem in complex Langevin simulation,” [arXiv:1511.02437 \[hep-lat\]](#).
- [139] J. R. Klauder, “A Langevin Approach to Fermion and Quantum Spin Correlation Functions,” *J. Phys.* **A16** (1983) L317.
- [140] J. R. Klauder, “Coherent-state Langevin equations for canonical quantum systems with applications to the quantized Hall effect,” *Phys. Rev. A* **29** (1984) 2036–2047.
- [141] G. Parisi, “On complex probabilities,” *Phys. Lett. B* **131** (1983) 393–395.
- [142] P. H. Damgaard and H. Hufel, “Stochastic Quantization,” *Phys. Rep.* **152** (1987) 227.
- [143] G. Parisi and Y.-s. Wu, “Perturbation Theory Without Gauge Fixing,” *Sci.Sin.* **24** (1981) 483.
- [144] G. Aarts, E. Seiler, and I.-O. Stamatescu, “The Complex Langevin method: When can it be trusted?,” *Phys. Rev. D* **81** (2010) 054508, [arXiv:0912.3360 \[hep-lat\]](#).
- [145] G. Aarts, F. A. James, E. Seiler, and I.-O. Stamatescu, “Complex Langevin: Etiology and Diagnostics of its Main Problem,” *Eur. Phys. J. C* **71** (2011) 1756, [arXiv:1101.3270 \[hep-lat\]](#).
- [146] J. Nishimura and S. Shimasaki, “New insights into the problem with a singular drift term in the complex Langevin method,” *Phys. Rev. D* **92** (2015) 011501, [arXiv:1504.08359 \[hep-lat\]](#).
- [147] G. Aarts and F. A. James, “Complex Langevin dynamics in the SU(3) spin model at nonzero chemical potential revisited,” *JHEP* **01** (2012) 118, [arXiv:1112.4655 \[hep-lat\]](#).
- [148] S. Eilenberg and N. E. Steenrod, “Axiomatic approach to homology theory,” *Proc Natl Acad Sci U S A* **31** no. 4, (1945) 117.
- [149] E. Witten, “Supersymmetry and Morse theory,” *J. Diff. Geom.* **17** (1982) 661–692.
- [150] R. Bott, “Morse theory indomitable,” *Publications Mathématiques de l’IHÉS* **68** (1988) 99–114.
- [151] A. Floer, “Morse theory for Lagrangian intersections,” *J. Differential Geom.* **28** no. 3, (1988) 513–547.
- [152] E. Frenkel, A. Losev, and N. Nekrasov, “Notes on instantons in topological field theory and beyond,” *Nucl.Phys.Proc.Suppl.* **171** (2007) 215–230, [arXiv:hep-th/0702137 \[hep-th\]](#).
- [153] E. Frenkel, A. Losev, and N. Nekrasov, “Instantons beyond topological theory. I,” [arXiv:hep-th/0610149 \[hep-th\]](#).

- [154] E. Frenkel, A. Losev, and N. Nekrasov, “Instantons beyond topological theory II,” [arXiv:0803.3302](#) [hep-th].
- [155] K. Fukushima and Y. Tanizaki, “Hamilton dynamics for the Lefschetz thimble integration akin to the complex Langevin method,” *Prog. Theor. Exp. Phys.* **2015** (2015) 111A01, [arXiv:1507.07351](#) [hep-th].